Carbon nanotube electromechanical systems: Non-linear dynamics and self-oscillation

by

Kyle Willick

A thesis
presented to the University of Waterloo
in fulfillment of the
thesis requirement for the degree of
Doctor of Philosophy
in
Physics (Nanotechnology)

Waterloo, Ontario, Canada, 2020

Examining Committee Membership

The following served on the Examining Committee for this thesis. The decision of the Examining Committee is by majority vote.

External Examiner:	Edward Laird Lecturer, Dept. of Physics, Lancaster University
Supervisor(s):	Jonathan Baugh Associate Professor, Dept. of Chemistry, University of Waterloo
Internal Member:	Raffi Budakian Professor, Dept. of Physics and Astronomy, University of Waterloo
Internal-External Member:	Na Young Kim Associate Professor, Dept. of Electrical and Computer Engineering, University of Waterloo
Other Member(s):	Robert Hill Associate Professor, Dept. of Physics and Astronomy, University of Waterloo

Author's Declaration

I hereby declare that I am the sole author of this thesis. This is a true copy of the thesis, including any required final revisions, as accepted by my examiners.

I understand that my thesis may be made electronically available to the public.

Statement of Contributions

The following thesis chapters were based on articles published or submitted for publication

- Chapter 4:
  - Willick, K., Tang, X., & Baugh, J. (2017). Probing the non-linear transient response of a carbon nanotube mechanical oscillator. *Applied Physics Letters*, 111(22), 223108.
- Chapter 5:
  - Willick, K., & Baugh, J. (2020). Self-driven oscillation in Coulomb blockaded suspended carbon nanotubes. preprint arXiv:2003.01229.
- Chapter 6:
  - Willick, K., Park, D. K., & Baugh, J. (2018). Efficient continuous-wave noise spectroscopy beyond weak coupling. *Physical Review A*, 98(1), 013414.

The device fabrication, measurement, and analysis presented in this thesis was performed by Kyle Willick with supervision and guidance from Jonathan Baugh, and the following contributions from additional parties:

- Daniel Park contributed to the theory/analysis presented in chapter 6, particularly that in section 6.2
- The dilution refrigerator wiring presented in appendix E was a collaborative project between all members of Jonathan Baugh's Coherent Spintronics research group, with primary contributions from Brandon Buonacorsi on the room temperature to mixing chamber cabling, Kyle Willick on mixing chamber components, and Eduardo Barrera who performed the electron thermometry experiments.

Abstract

This thesis is motivated by the many sensing applications of carbon nanotube (CNT) nano-electromechanical systems (NEMS), both previous state-of-the-art demonstrations and proposed new uses. This research is particularly focused on the long term goal of realizing the magnetic force sensing of molecular nanomagnets, proposed in reference [1].

The fabrication of micron long, small diameter, high quality suspended carbon nanotubes is a challenging task. Integrating ferromagnetic structures which are incompatible with the CNT growth procedures increases this challenge. In this thesis, devices suitable for magnetic force sensing experiments are realized by separating the chemical vapour deposition growth of CNTs from the device contacts and gates, while maintaining CNT quality.

Using conventional readout techniques, the low-temperature measurement of the CNT NEMS mechanical state is usually limited by the CNT contact resistance and capacitance of the measurement cabling/circuit. I describe the use of a heterojunction bipolar transistor (HBT) amplifying circuit operating at cryogenic temperatures near the device to measure the mechanical amplitude at microsecond timescales. A Coulomb rectification scheme, in which the probe signal is at much lower frequency than the mechanical drive signal, allows investigation of the transient response with strongly non-linear driving. The transient dynamics in both the linear and non-linear regimes are measured and modeled by including Duffing and non-linear damping terms in a harmonic oscillator equation. The non-linear regime can result in faster sensing response times, on the order of 10 μs for the device and circuit presented.

Self-driven oscillations in suspended carbon nanotubes can create apparent instabilities in the electrical conductance of the CNT. In literature, such instabilities have been observed in kondo regime or high bias transport. In this thesis, I observed self-driven oscillations which created significant conduction within the nominally Coulomb-blockaded low-bias transport. Using a master equation system model, these oscillations are shown to be the result of strongly energy dependent electron tunneling to the contacts of high quality CNT NEMS operated at sub-Kelvin temperatures.

Finally, in a separate research project, I consider the noise characterization of spin qubits interacting with the environment. In particular, I address the problem of probing the spectral density $S(\omega)$ of semi-classical phase noise using a spin interacting with a continuous-wave (CW) resonant excitation field. Previous CW noise spectroscopy protocols have been based on the generalized Bloch equations (GBE) or the filter function formalism, and assumed weak coupling to a Markovian bath. However, those protocols

can substantially underestimate $S(\omega)$ at low frequencies when the CW pulse amplitude becomes comparable to $S(\omega)$. I derive the coherence decay more generally by extending to higher orders in the noise strength and discarding the Markov approximation. Numerical simulations show that this provides a more accurate description of the spin dynamics compared to a simple exponential decay, especially on short timescales. Exploiting these results, a new protocol is developed that uses an experiment at a single CW pulse amplitude to extend the spectral range over which $S(\omega)$ can be reliably determined, down to $\omega = 0$.

Acknowledgements

I would like to first thank my graduate supervisor, Jonathan Baugh, for his continued support and guidance throughout this research project. Thank you also to my advisory committee members Raffi Budakian, Rob Hill, and Shirley Tang, for timely advice and direction to keep my research moving forward. Additionally, I am grateful to Na Young Kim and Edward Laird for taking part on my thesis defense committee.

Next I would like to thank the many CSG research group members who have helped me along the way. My start in both nanofabrication and experiments would not have gone as smoothly without the aide and input of Greg, Kaveh, Chris, Yipu, and Mustafa. I thank Sean, Brandon, Eduardo, Annelise, Daryoush, Milad, Ferhat, Arjun, and Francois for many helpful discussions and always lending a hand in the lab. I'm also thankful to Daniel Park, who introduced me to the realm of noise spectroscopy and whose ideas and analysis started the path that led to Chapter 6.

I am grateful to the Tang Nanotechnology Lab members who allowed me to continuously work in their lab growing CNTs. In particular, I thank Andrew who spent countless hours teaching me the CVD systems and processes; and Gaganprit, Zhi, and Irfani for putting up with my constant scheduling emails and changes to the CVD.

I'd like to thank Yutian Wen of the Quantum Electronics Devices group at Oxford University who provided his expertise to help me develop our version of the stamping fabrication processes.

The devices presented in this thesis would not be possible without the Quantum-Nano Fabrication & Characterization Facility. Thank you to all of the staff for keeping the QNFCF facility running smoothly and ever growing, and for providing invaluable troubleshooting of my fabrication processes.

My time in graduate school was made possible by financial support of the National Science and Engineering Research Council (NSERC), the Ontario government, the University of Waterloo, and the Institute for Quantum Computing. This research was also supported by generous funding of fabrication and lab facilities by NSERC, the Ontario Ministry for Research and Innovation, Canada First Research Excellence Fund, and the Canadian Foundation for Innovation.

A special thank you to my friends and family for keeping me going. I'm especially grateful to my parents for always supporting me. And a final giant thank you to Kirstin, for all that you do.

Table of Contents

List of Tables

List of Figures

Chapter 1

Introduction

Microelectromechanical systems(MEMS) are ubiquitous in modern technology. MEMS devices use coupling between mechanical motion at micron scales and electronic behavior to realize a wide variety of applications, such as aviation gyroscopes [2], chip-scale vacuum pumps [3], actuators [4], gas sensors [5], optical displays [6] and many more [7]. In the past few decades, advances in lithography and material growth have opened the field of nano-electromechanical systems (NEMS), the nanoscale evolution of MEMS. The reduced size of these systems can not only improve the performance in current MEMS applications, as demonstrated in single-charge electrometry [8] and magnetic resonance force microscopy [9], but can also be pushed into entirely new regimes such as quantized states of mechanical motion [10].

NEMS fabrication can be realized in either a top-down or bottom-up process. Top-down fabrication is a subtractive process in which a bulk material is patterned and selectively etched away to form the device of interest. With modern lithography, devices with dimensions $\sim 10\,\mathrm{nm}$ are readily achievable [11]. An issue with top-down fabrication is that the device surfaces are exposed to the potentially damaging fabrication processes, and as a result surface defects in the final device are common. As device size decreases, the ratio of surface to bulk increases, making these surface defects very detrimental to NEMS performance. In bottom-up fabrication, the NEMS device is assembled in place from molecular level building blocks. Prevalent examples of bottom-up devices include semiconducting nanowires and suspended nanotubes. The dimensions of such NEMS are limited only by the achievable material growth.

Among NEMS realizations, the suspended carbon nanotube (CNT) stands out for its exceptionally low mass, one-dimensional electrical conductance, mechanical strength, stiff-

ness, and tunability. The first suspended single-wall CNT NEMS resonator was realized in 2004 when the amplitude of room temperature oscillations of a single suspended CNT were measured [12]. In 2009, fabrication and measurement improvements realized the first high quality CNT resonators [13, 14]. Experiments on these high quality devices began to highlight the rich behavior of CNT NEMS, such as mode-coupling [15], parametric driving [16], and SET-mechanical feedback [14, 17, 18, 19]. Within a few years, these devices had achieved state-of-the-art mass sensing down to the level of a single proton [20] and zepto-Newton force sensitivity [21]. Suspended CNT devices have also demonstrated operation up to $\sim 100\,\mathrm{GHz}$, allowing for quantized mechanical states at cryogenic temperatures without active cooling. [22, 23]. More recent improvements to the operation and measurement of CNT resonators have realized mechanical quality factors up to 5 million [24], readout sensitivity down to intrinsic thermal fluctuations [25], and real time optical position measurement [26].

The record sensitivity of CNT NEMS opens up the possibility for new sensing applications. For example, coupling the spin state of an adhered molecule, such as a molecular nanomagnet, to the oscillations of the CNT would allow novel studies of the magnetic states of these molecules [27]. Such a coupling was proposed [28] and demonstrated [29] using the torque induced on an anisotropic nanomagnet attached to a CNT. In a previous work, I proposed a higher sensitivity coupling based on the force acting on a nanomagnet in a magnetic field gradient, created by a nearby micromagnetic structure [1]. The fabrication processes presented in this thesis are motivated by the realization of such a device, and the experimental work is aimed towards its the operation.

This thesis is organized as follows. **Chapter 2** discusses the electrical and mechanical properties of CNT NEMS, providing relevant background information for the work presented in later chapters. **Chapter 3** details the nanofabrication of the CNT NEMS devices studies in this thesis, including specifics on the CVD growth of small diameter, defect free CNTs. **Chapter 4** describes an experiment in which cryogenic amplification using a heterojunction bipolar transistor was used to measure the transient response of a suspended CNT resonator, and modeling of this response with a non-linear resonator description. **Chapter 5** reports the experimental observation of self-driven oscillations in Coulomb-blockaded suspended CNTs. Using a master equation derived model of the combined single electron transistor-resonator system, these features are simulated and understood as a result of energy-dependence in the adjacent tunneling processes. **Chapter 6** discusses a separate research project, in which noise spectroscopy of spin systems in the presence of dominant phase noise was addressed using a new continuous driving protocol. **Chapter 7** concludes the main results of this thesis and discusses future direction.

Chapter 2

Carbon nanotube nanoelectromechanical systems

In this chapter, I give an overview of the electronic and mechanical properties of carbon nanotubes that will be relevant in this thesis. After a quick review of the single wall CNT structure and electronic properties, I describe the electromechanical coupling and its use for driving and readout of CNT motion. Then I detail some of the applicable models for the mechanical motion of suspended CNTs, specifically a harmonic oscillator description and an Euler-Bernoulli beam model.

2.1 The carbon nanotube

Structurally, it is convenient to think of a CNT as rolled strip of graphene. Figure 2.1 shows graphene lattice with unit vectors, $\vec{a}_1$ and $\vec{a}_2$, and the chiral vector $\vec{C}$ that will define the CNT. The chiral vector represents the circumference of the CNT, such that the end points of $\vec{C}$ are the same point of the CNT. The chiral vector is specified by the integer multiples for each unit vector that make up $\vec{C}$

$$\vec{C} = n\vec{a}_1 + m\vec{a}_2 \equiv (n, m) \tag{2.1}$$

The CNT are categorized by their chiral vector. Armchair ($n = m$) and zigzag ($m = 0$) nanotubes represent special cases, while all other chiralities are generally referred to as chiral.

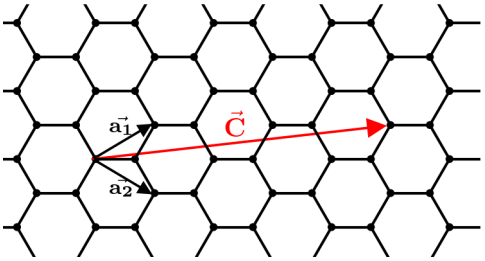

Figure 2.1: The direct lattice of graphene, including the primitive unit vectors $\vec{a}_1$ and $\vec{a}_2$. The chiral vector $\vec{C}$ is used to specify CNT geometries, where the CNT is formed by connected the end-points of $\vec{C}$. In this figure $\vec{C} = 3\vec{a}_1 + 2\vec{a}_2 = (3, 2)$

In the same way that the physical structure of the CNT can be thought of a rolled strip of graphene, the electronic properties of the CNT can be built up starting from those of graphene, using the zone folding approximation [30]. Figure 2.2a shows the energy dispersion of the conduction (π^*) band of graphene in reciprocal space. The corners of the hexagonal Brillouin zone, labeled K and K', are known as the Dirac points, where the conduction and valence band touch.

As a first-order approximation, the rolling of the graphene lattice into a CNT does not alter the band structure, except to impose periodic boundary conditions, corresponding to the CNT circumference, on the available k vectors. The periodic boundary conditions result in the circumferential wave vector component, $k_\perp$ taking only discrete values, while the component along the CNT axis, $k_{||}$, remains continuous. The band dispersion of the CNT then corresponds to slices at these discrete $k_\perp$ states across the graphene energy dispersion. The properties of the CNT will be determined by how these cuts align on the graphene dispersion. Figure 2.2b gives an example of $k_\perp$ traces when $(n-m)$ is a multiple of 3. In this case, some $k_\perp$ align exactly over the Dirac points, resulting in the conduction and valence bands of the CNT touching, as shown in figure 2.2d. Unlike graphene, there is a finite density of states in CNTs at these points, resulting in metallic conduction in these CNTs. Figure 2.2c shows the dispersion cuts when $(n-m)$ is not a multiple of 3. In this case, $k_\perp$ will not cross the Dirac points. This results in a bandgap between valence and conduction bands. The CNT behaves as a semiconductor with an approximate bandgap of $E_g \approx 0.9\text{eV}/d$, where d is the nanotube diameter in nm. An example semiconducting CNT dispersion is shown in figure 2.2e.

The zone-folding approximation, in particular the assumption that rolling the graphene

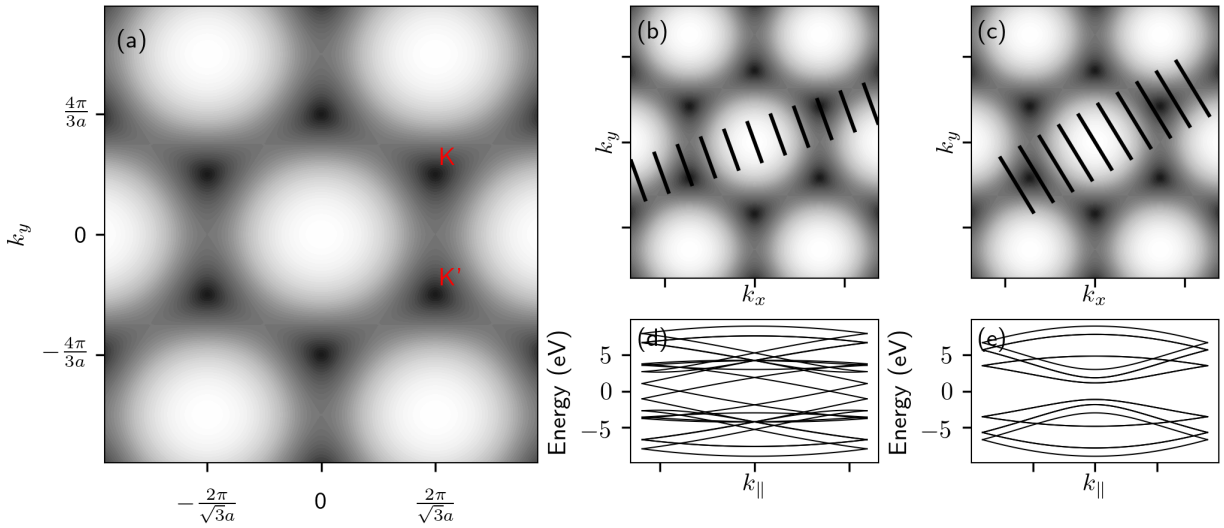

Figure 2.2: **a** The energy dispersion relations of the conduction band of graphene. Darker regions represent lower energy. The dirac points, labelled K and K', are the points at which the conduction and valence bands touch. The allowed $\vec{k}$ of the first Brillouin zone for a **b** (4,1) and **c** (5,0) CNT, displayed on the graphene conduction band dispersion. The subband energies corresponding to slices at of the graphene dispersion at the allowed $k_\perp$ are shown in **d** and **e**, respectively.

into a CNT does not perturb the underlying energy dispersion, is not completely accurate and the discrepancies are important for "metallic" CNTs from above. Briefly, the curvature of the graphene lattice breaks the symmetry of electron orbitals in the lattice, and shifts the Dirac points (K/K') in the reciprocal space. For nominally metallic CNTs, this can move the dirac points away from the allowed $k_\perp$, opening a small bandgap in the CNT. The curvature-induced bandgap is given by [31, 32]

$$E_g \approx \frac{37\ \text{meV}}{d^2[\text{nm}]} \cos(3\theta) \tag{2.2}$$

where $\theta = \tan^{-1}\left(\frac{\sqrt{3}m}{2n+m}\right)$ is the angle between the chiral vector and a_1. Additional bandgap opening can be induced through a similar mechanism caused by mechanical strain in the CNT. Axial strain results in an expected bandgap of [32, 33]

$$E_g \approx \frac{51\ \text{meV}}{\epsilon[\%]} \cos(3\theta) \tag{2.3}$$

Small bandgap CNTs created by the above perturbations to nominally metallic CNTs are the focus of experiments in this thesis. These CNTs are useful for low temperature experiments due in part to their low effective carrier mass ($m^* \sim 0.014 m_e$ for 100meV bandgap CNT). This effective mass results in large energy level spacings, allowing energy resolved quantum dots to be formed in $\sim 1\ \mu$m long CNTs [32]. At low temperatures, these micron-dimension CNTs often behave as single electron transistors owing to tunnel barriers formed at CNT-metal interfaces [34].

2.1.1 Single electron transistors

A general single electron transistor (SET) is comprised of an conducting island that is tunnel coupled to source and drain reservoirs, with the condition that the contact resistance satisfies $R_c \gg h/e^2$ to resolve energy levels [35]. The island is also capacitively coupled to a third electrode, called the gate, which can shift the electrostatic potential of the island. Adding an electron to the island requires an addition energy $U_C = e^2/C$, where e is the electron charge and $C = C_s + C_g + C_d$ is the total capacitance of the island.

When $U_C \gg k_B T$, the energy to add the next electron cannot be supplied by thermal energy alone, and the SET experiences Coulomb blockade. Figure 2.3a and 2.3b show the energy diagram for two states of a SET at $T = 0$ K, for a small bias across the device $V_{sd} = V_s - V_d < U_C$. In figure 2.3a, there is no dot energy state between the source and

drain chemical potentials. In this case, every state below the source/drain potentials is filled with an electron, and every state above is unfilled. No state is available for electrons to tunnel from the higher energy lead onto the dot, and no current will flow across the island. In figure 2.3b, one of the discrete dot energy levels is within the bias window ($\mu_d < \mu_{dot,n} < \mu_s$). In this case, an electron in that state can tunnel out of the dot to the drain, and an electron from the source can tunnel into the dot when that state is unoccupied. This tunneling channel can be observed as a finite current across the dot, the magnitude of which depends on the tunneling rates between the leads and the dot. The characteristic peaks at low bias as a function of gate voltage, shown in figure 2.3c, are referred to as Coulomb peaks.

With increasing bias, the window between source/drain chemical potentials opens, eventually becoming greater than the dot energy separation, U_C. Then there will always be an energy level available for tunneling, and thus a finite current through the SET. The map of conductance through the dot as a function of gate voltage and bias creates the Coulomb diamond pattern, depicted in figure 2.3d. The size and slopes of the Coulomb diamond can be used to determine system capacitance values (C_s,C_d,C_g) and charging energy (U_C) of the dot [36].

For particular quantum dot islands, the discrete orbital states of the quantum dot can also be observed in the Coulomb blockade features. In ideal carbon nanotubes, each of these orbital energy levels has four-fold degeneracy due to the electron and valley degrees of freedom [37]. For partially filled orbital levels, the energy to add the next electron is U_C as above. When an orbital is filled, adding the next electron also requires the energy difference to the next orbital level $U_C + \Delta E$. This leads to a four-fold pattern in the addition energy, which can be observed experimentally as the separation between adjacent Coulomb peaks. An example of this four-fold energy spacing that was measured in one of the CNT devices in this thesis is shown in figure 2.4.

2.2 Electro-mechanical coupling

In CNT NEMS, the experimentally accessible electronic properties of the CNT are typically used to both control and measure the mechanical state. The electro-mechanical coupling in suspended CNT devices stems from the electrostatic force between the gate electrode and the CNT, and modulation of the capacitance to the gate electrode with mechanical displacement. The electrostatic force allows a high-frequency gate voltage signal to excite mechanical motion, while the capacitance modulation is used for readout.

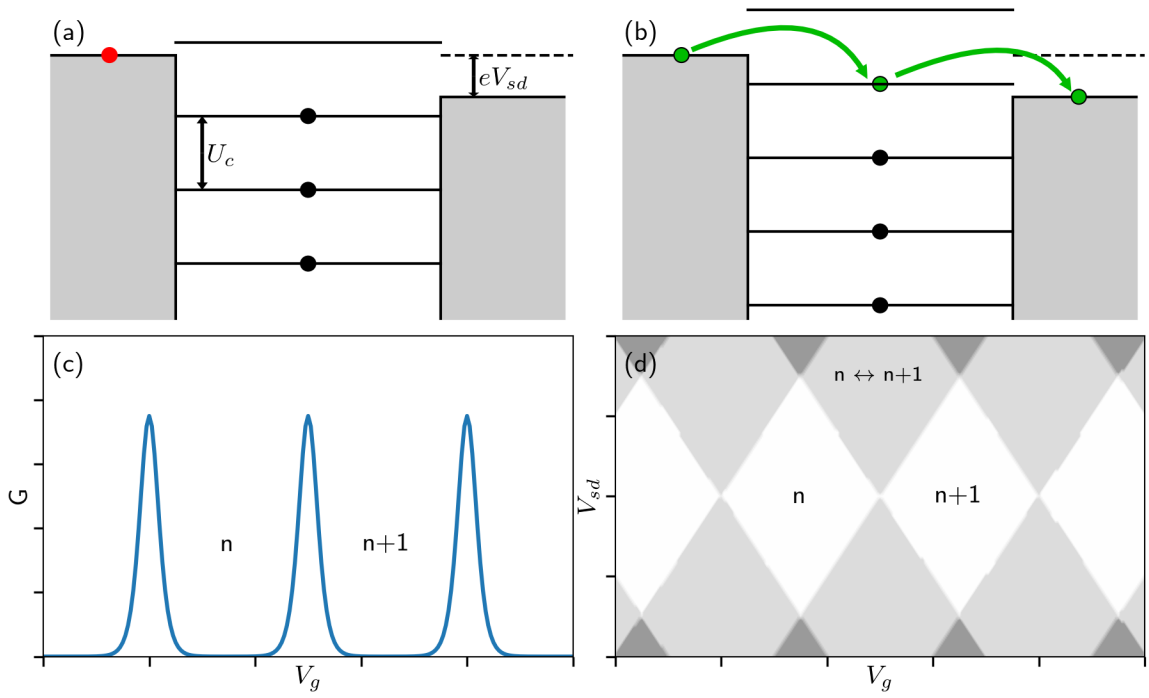

Figure 2.3: **a** A single electron transistor, in Coulomb blockade. The leads are tunnel coupled to the center quantum dot, but in this configuration no discrete energy levels of the dot lie within the bias window (eV_{sd}), so no current can flow. **b** Conduction occurs via sequential tunneling when one of the quantum dot energy levels is within the bias window. **c** At low bias voltages this leads to Coulomb peaks, a pattern in conduction with respect to gate voltage, V_g, which tunes the energy levels of the quantum dot. Between Coulomb peaks the electron number on the quantum dot is fixed, denoted by the electron occupation numbers, n and $n+1$. **d** The conduction of a quantum dot as a function of V_{sd} and V_g shows a characteristic diamond pattern. Within the low bias diamonds, conduction through the single electron transistors is blocked.

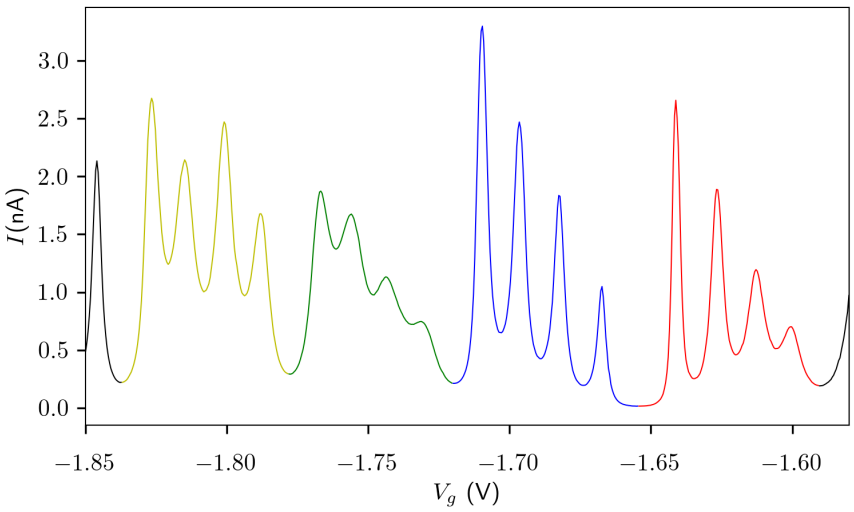

Figure 2.4: Peaks in the current (I) as a function of gate voltage (V_g) measured in a carbon nanotube transistor. The spacing of adjacent peaks exhibit a four-fold periodicity, due to the four-fold degeneracy of CNT orbital states.

2.2.1 Mechanical driving

The electrostatic force between capacitively coupled components is given by [38]

$$F_c = \nabla\left(\frac{1}{2}CV^2\right) \approx \frac{1}{2}\left(\nabla C\right)V^2 \tag{2.4}$$

where C is the capacitance and V is the voltage difference between elements. The approximation assumes that displacement induced voltage difference can be neglected, which is satisfied for CNT resonators under the condition that the amplitude of motion is much less than the gate-CNT separation. When the suspended CNT operates as a quantum dot, then there can be some non-zero induced voltage on the dot, and the gate-CNT force is written as

$$F_{g-cnt} = \frac{1}{2}\frac{\partial C_g}{\partial x}(V_g - V_{cnt})^2 \tag{2.5}$$

where

$$V_{cnt} = \frac{1}{C_{tot}}\left(C_gV_g + C_sV_s + C_dV_d - e\langle N\rangle\right) \tag{2.6}$$

with $\langle N\rangle$ the average electron occupation of the dot, $C_*(V_*)$ are the capacitance (voltage) of the gate, source, and drain, and $C_{tot} = C_g + C_s + C_d$.

The V_{cnt} component introduces an important coupling between single electron tunneling and the force on the CNT that will be discussed further in chapter 5, however for the typical operation regime $V_{cnt} \ll V_g$ so to first order driving of the CNT is dependent on

$$F_{g-cnt} \approx \frac{1}{2}\frac{\partial C_g}{\partial x}V_g^2 \tag{2.7}$$

The typical operation of suspended CNT resonators uses a large DC gate voltage to allow readout and tune the tension of the CNT, and a smaller high frequency driving voltage. Then the force acting on the CNT can be approximated,

$$\begin{aligned} F_{g-cnt} &\approx \frac{1}{2}\frac{\partial C_g}{\partial x}\left(V_{g,dc} + V_{g,ac}\right)^2 \\ &\approx \frac{1}{2}\frac{\partial C_g}{\partial x}\left({V_{g,dc}}^2 + 2V_{g,dc}V_{g,ac}\right) \end{aligned} \tag{2.8}$$

Thus, the cnt oscillations are driven by the high frequency force component

$$F_{ac} \approx \frac{\partial C_g}{\partial x}V_{g,dc}V_{g,ac} \tag{2.9}$$

2.2.2 Readout of mechanical motion

There are many schemes to transduce the mechanical motion of the CNT to an electrical output. The common element to each is that they make use of the modulation of the CNT-gate capacitance by displacement of the CNT. To illustrate this modulation, this capacitance can be approximated as that of a wire adjacent to an infinite plane

$$C_g \approx \frac{2\pi\epsilon_0 L}{\cosh^{-1}(h/r)} \approx \frac{2\pi\epsilon_0 L}{\ln(2h/r)} \tag{2.10}$$

where L is the CNT length, h is the gate-CNT separation, and r is the CNT diameter. The second approximation uses the fact that $h \gg r$ for practical CNT devices.

The motion of the CNT changes the gate separation ($h \to h + x$), so that

$$C_g(x) = \frac{2\pi\epsilon_0 L}{\ln(2(h+x)/r)} \approx \frac{2\pi\epsilon_0 L}{\ln(2h/r)} - x\frac{\pi\epsilon_0 L}{h\ln(2h/r)} \tag{2.11}$$

where the second approximation uses $x \ll h$.

The conductance through the CNT will depend on the induced charge of the CNT, $q_i = C_g V_g + C_s V_s + C_d V_d \approx C_g V_g$. Therefore, a modulation of C_g will be translated to a modulation of q_i and a change in conductance measured across the CNT. The exact form of the conductance modulation will depend on the CNT device and the applied gate voltage, and can range from weak modulation in Fabry-Perot regime to sharp changes across Coulomb-blockade peaks [34].

A complication for mechanical readout arises due to the high impedance of the metal-CNT interfaces. This intrinsic device resistance, combined with practical capacitances of most experimental measurements, will limit measurement circuit bandwidths to the RC cut-off frequency $\omega_c = \frac{1}{RC}$. For many of the CNT devices seen during this thesis research, on-state CNT resistance exceeded 250 kΩ. Typical high-frequency cabling to carry the signal out of cryostats will contribute capacitances of $C > 400$ pF. This results in cut-off frequencies $\omega_c \lesssim 10$ kHz, much less than the mechanical resonance frequencies of micron-length CNT resonators ($\omega_{res} \sim 50 - 100$ MHz).

One technique to increase the readout bandwidth is to significantly reduce the capacitance in the measurement circuit before the first-stage of amplification. An implementation of this using a heterojunction bipolar transistor is the focus of chapter 4. Other implementations using cryogenic high-electron mobility transistors [39, 40] and impedance matching RLC circuitry [41, 25] have been demonstrated in literature.

In the absence of cryogenic amplification implementations, a number of readout protocols have been introduced in literature that measure the average amplitude of the CNT motion on a slower measurement signal. In this section I will discuss a few of these techniques which were used in my thesis research.

Two Source Mixing

The first realization of CNT mechanical readout used the non-linear conductance modulation of the CNT to act as a mixer circuit element, and by doing so generate an output signal at low frequency that was dependent on the amplitude of motion [12].

In the original two-source mixing implementation the AC component of the gate voltage oscillates at frequency ω, and the bias voltage applied across the source-drain contacts is an AC voltage oscillating at offset frequency $\omega + \delta\omega$. The gate voltage and capacitance can be written as DC and AC components, $V_g = V_g^{dc} + V_g^{ac}(t)$ and $C_g = C_g^{dc} + C_g^{ac}(t)$, where $C_g^{ac}(t)$ is a result of the mechanical motion of the CNT.

$$C_g^{ac}(t) \approx \left.\frac{\partial C_g}{\partial x}\right|_{x=0} x(t) \tag{2.12}$$

where $x(t)$ is the displacement of the CNT from equilibrium averaged along the CNT. Then the conductance of the CNT is given by

$$G = \frac{\partial G}{\partial q} q = \frac{\partial G}{\partial q} C_g V_g \approx \frac{\partial G}{\partial q} \left(C_g^{dc} V_g^{dc} + C_g^{ac} V_g^{dc} + C_g^{dc} V_g^{ac} \right) \tag{2.13}$$

$$\approx \frac{\partial G}{\partial q} \left(C_g^{dc} V_g^{dc} + \left. \frac{\partial C_g}{\partial x} \right|_{x=0} x(t) V_g^{dc} + C_g^{dc} V_g^{ac} \right) \tag{2.14}$$

where the first approximation is to first order in the small terms V_g^{ac} and C_g^{ac}. Note that the conductance modulation can be calculated from experimentally accessible values as $\frac{\partial G}{\partial q} = \frac{\partial G}{\partial V_g} \frac{1}{C_g}$.

Now writing the gate and bias voltages as sinusoidal voltages at frequencies as described above, $V_g^{ac}(t) = V_g^{ac} \cos(\omega t)$ and $V_{sd} = V_{sd}^{ac} \cos((\omega + \delta\omega)t + \phi_{sd})$, gives a current through the CNT of

$$I = G V_{sd} = \frac{\partial G}{\partial q} \left(C_g^{dc} V_g^{dc} + \left. \frac{\partial C_g}{\partial x} \right|_{x=0} x(t) V_g^{dc} + C_g^{dc} V_g^{ac} \cos(\omega t) \right) V_{sd}^{ac} \cos((\omega + \delta\omega)t + \phi_{sd}) \tag{2.15}$$

If the CNT has a simple harmonic oscillator response (further discussed in section 2.3.1) then

$$x(t) = \frac{F_d/m}{\sqrt{\left(\omega_0^2 - \omega^2\right)^2 + \omega^2 \omega_0^2 / Q^2}} \cos(\omega t + \phi) \tag{2.16}$$

where $F_d \approx C_g' V_g^{dc} V_g^{ac}$ is the AC driving force as above, ω_0 is the resonant frequency, Q is the quality factor, and ϕ is a phase resulting from regular simple harmonic oscillator phase response and the details of tunneling and charging of the CNT [42].

The current at the mixing frequency $\delta\omega$ will then be

$$I_{\delta\omega} = \frac{\partial G}{\partial q} V_{sd}^{ac} \left(\frac{(V_g^{dc} C_g')^2 V_g^{ac}}{2m\sqrt{\left(\omega_0^2 - \omega^2\right)^2 + \omega^2 \omega_0^2 / Q^2}} \cos(\delta\omega t + \phi_{sd} - \phi) + \frac{1}{2} C_g^{dc} V_g^{ac} cos(\delta\omega t + \phi_{sd}) \right) \tag{2.17}$$

The first term in equation (2.17) is the result of mechanical motion of the CNT, while the second term is a purely electrical term that is present in the absence of CNT motion. Mechanical motion of the CNT is measured by distinguishing the sharp peak in I vs. ω associated with the first term, which has a full-width half-maximum of ω_0/Q.

Since the original demonstration of mixing in the CNT, several alternative methods have been proposed that used mixed signals for CNT readout. For example, amplitude modulation of a single high frequency input at the source contact leads to the same current as equation (2.17) at the amplitude modulation frequency, while requiring only one high frequency signal [42]. Another modification of the mixing technique that is used in this thesis is the frequency modulation of a single high frequency input.

Frequency Modulation

As mentioned above, the current from the two-source or amplitude-modulated mixing signal includes a purely electrical component at the mixing frequency. This signal can mask mechanical measurements, particularly for weak driving/small amplitude motion. Frequency modulation of the high frequency input signal results in an output at the modulation frequency that is dependent only on the mechanical response of the system[43, 44].

A frequency modulated source-drain voltage is given as

$$V_{sd}^{fm} = V_{sd}^{ac} \cos\left(\omega t + \frac{\Delta\omega}{\Omega}\sin(\Omega t)\right) \tag{2.18}$$

where $\Delta\omega$ is the modulation strength and Ω is the modulation frequency. The FM signal can be decomposed in the Jacobi-Anger expansion, as an infinite sum of oscillations at frequencies $\omega \pm n\Omega$. The mixing current at Ω can then be calculated as[43]

$$I_\Omega = \frac{1}{2}\frac{\partial G}{\partial V_g} V_g^{dc} \frac{C_g'}{C_g} V_{sd}^{ac} \Delta\omega \frac{\partial x}{\partial \omega} \tag{2.19}$$

which is only present when there is a mechanical response of the resonator. It should be noticed that the FM modulation couples the current to $\frac{\partial x}{\partial \omega}$, rather than directly to x, so that $|I_\Omega|$ is maximum on the edges of the resonant peak, $\omega = \omega_0 \pm \omega_0/Q$. In this thesis, FM modulated mixing is used to locate mechanical resonances in previously untested CNT devices.

Coulomb rectification readout

An alternative readout scheme which is used throughout the measurements present in subsequent chapters is the Coulomb rectification scheme, originally proposed in reference [13]. This technique does not make use of signal mixing at the CNT. Rather, it relies on the rectification of the AC modulation of capacitance into a DC current by the non-linear

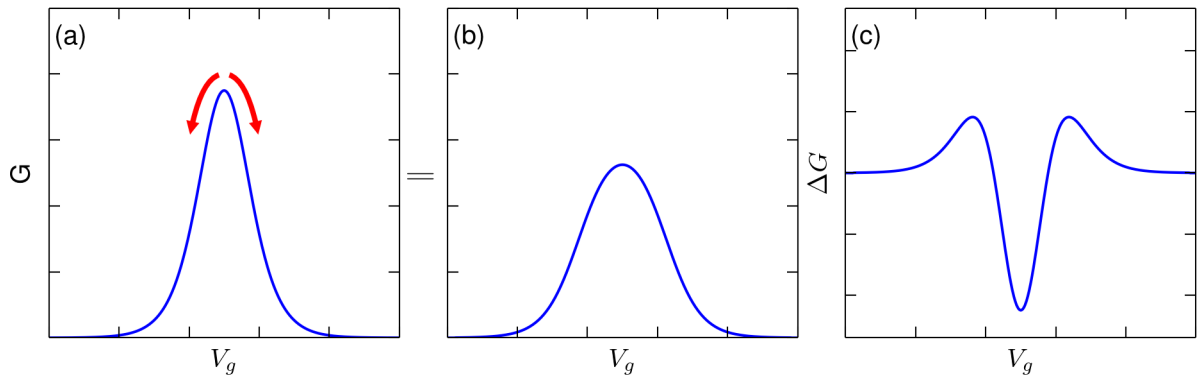

Figure 2.5: **a** An illustrative Coulomb peak of a stationary CNT transistor. **b** Mechanical oscillations of the CNT rapidly modulate the gate capacitance, effectively averaging the peak with respect to V_g. **c** The change in DC conductance between **a** and **b**, which occurs due to the mechanical motion of the CNT.

conductance of the CNT. As described in section 2.1.1, at low temperatures CNTs often experience a regime of Coulomb blockade, in which a series of sharp peaks in conductance are present at low bias. The mechanical oscillations of the CNT lead to a rapid modulation of the gate capacitance, and therefore induced charge of the CNT. This acts to "blur" the conductance as a function of gate voltage, as shown in figure 2.5a and 2.5b. When measuring the conductance at a fixed gate voltage, the mechanical motion is then seen as a sudden change in the conductance, as shown in figure 2.5c. The current through the CNT will be

$$I_{motion} = I_{stationary} + \left(\frac{x_{max}}{2}\frac{C_g'}{C_g}V_g\right)^2 \frac{\partial^2 I}{\partial V_g^2} + O(x_{max}^4) \tag{2.20}$$

where $I_{stationary}$ is the current in the absence of CNT motion, and x_{max} is the maximum amplitude of the CNT motion.

2.3 Mechanical Resonators

One of the main appeals of CNTs as nanoelectromechanical systems is the extremely low mass that can be realized in practical devices. The linear mass density of a CNT is given by $\rho A = \rho_G \pi d$, where $\rho_G = 7.7 \cdot 10^{-7}\,\mathrm{kg/m^2}$ is the area density of graphene. For a $1\,\mu$m long CNT with 1 nm diameter, the mass is $2.4 \cdot 10^{-21}$ kg, several orders of magnitude smaller than the mass of other realizable NEMS devices ($m \gtrsim 10^{-17}$ [45]).

Another valuable attribute of CNT NEMS is the high stiffness, characterized by the Young's modulus, $E \approx 1 - 1.3$ TPa [46, 47]. This mechanical rigidity is due to the sp^2 carbon-carbon bonds, among the strongest known bonds in chemistry [48] A high Young's modulus means that despite the small diameter, CNTs can act as stiff beam resonators. That is, the bending rigidity of a CNT, given by $D = EI$ remains high despite the small area moment of inertia, $I = \pi r^4/4$, relative to other NEMS.

The strong bonding in CNTs also lead to mechanically robust devices, which can withstand large tuning forces without damage. This can allow resonance frequencies to be tuned by more than a factor of 2 in many of the devices measured in this thesis. As part of this large tuning space, the mechanical behaviour of the CNT NEMS can be switched from beam-like at low applied forces to string-like resonances at higher forcing [49]. In the following sections I'll describe some of the models to capture the resonance behaviour of the CNT, from a simple harmonic oscillator picture to a more complete Euler-Bernoulli beam picture that can capture impact of changing CNT parameters.

2.3.1 Linear Harmonic Oscillators

It is often useful when describing a CNT NEMS device to use a simplifying description of the mechanical system as a lumped mass harmonic oscillator. This is particularly useful when modeling dynamics and interactions of the oscillations, in which more complete but cumbersome models would be computationally and analytically restrictive. In the harmonic oscillator picture, the CNT motion is described by a single variable, x, which corresponds to the displacement at the center of the suspended CNT section.

The general simple harmonic oscillator describes the motion of a mass with a linear relation between displacement and a restoring force, $F = -k \cdot x$, where the constant k is the spring constant of the system. This gives the simplest equation of motion for an oscillator

$$m\frac{\partial^2 x}{\partial t^2} + kx = 0 \tag{2.21}$$

For the CNT system, the mass (m) of the system is an effective mass that depends on the profile of motion of the full CNT.

There are additional components that can be included in the harmonic oscillator picture that will be relevant to any practical CNT device. The first of these is a dissipation mechanism. Clamping of the CNT at the contacts can lead to a dissipation of mechanical energy. Additionally, any fluctuations acting on the resonator, such as voltage noise on the capacitively coupled gate, will induce further dissipation [50]. These dissipation

mechanisms lead to energy loss in the resonator, and are often captured in the harmonic oscillator picture as a linear damping term

$$m\frac{\partial^2 x}{\partial t^2} + \gamma\frac{\partial x}{\partial t} + kx = 0 \tag{2.22}$$

Driving of the harmonic oscillator is included via an arbitrary time-dependent forcing term, $F(t)$. For all resonator driving used in this work, the force will be a sinusoidal drive, $F(t) = F_0 \sin(\omega_d t)$, where ω_d is the driving frequency and F_0 is the force amplitude seen by the CNT. The equation of motion for the sinusoidal driven, damped harmonic oscillator is

$$m\frac{\partial^2 x}{\partial t^2} + \gamma\frac{\partial x}{\partial t} + kx = F_0 \sin(\omega_d t) \tag{2.23}$$

which has the steady-state solution

$$x(t) = \frac{F_0}{m\sqrt{\left(\omega_d^2 - \omega_0^2\right)^2 + \left(\gamma\omega_d\right)^2}} \sin\left(\omega_d t + \phi\right) \tag{2.24}$$

where $\omega_0 = \sqrt{k/m}$ is the natural frequency of oscillation, and the phase response is given by

$$\phi = \tan^- 1\left(\frac{\gamma\omega_0}{\omega_0^2 - \omega_d^2}\right) \tag{2.25}$$

The amplitude and phase response to driving is shown in figure 2.6.

Non-linearity

The equations of motions in the above section assume linear restoring forces and damping. This assumption works well for very small amplitudes of motion, but for larger amplitudes non-linear responses must be considered. Non-linear terms are particularly important for suspended CNT resonators, where oscillations greater than CNT diameter and SET-mechanical feedback both lead to large non-linear coefficients [14, 19].

The first-order non-linearity in restoring force is called the Duffing non-linearity and takes the form αx^3 where the Duffing constant α gives the strength of the non-linearity, and can be either negative or positive. The equation of motion of a driven, damped, Duffing oscillator is

$$m\frac{\partial^2 x}{\partial t^2} + \gamma\frac{\partial x}{\partial t} + kx + \alpha x^3 = F_0 \sin(\omega_d t) \tag{2.26}$$

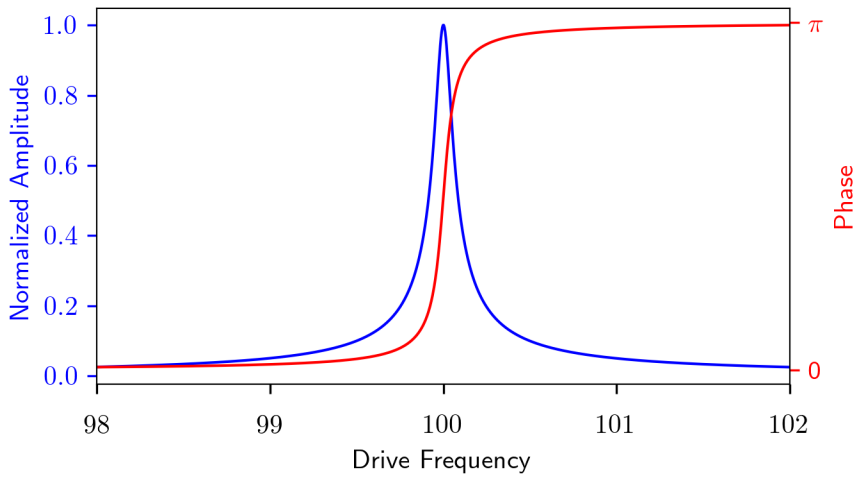

Figure 2.6: Driven response of a simple harmonic oscillator with $\omega_0 = 100$, $\gamma = 0.1$.

The Duffing oscillator is a chaotic system without exact analytic solution. However, for moderate-amplitude oscillations as will be considered for the CNT oscillators, solutions are of the form $x(t) = \mathcal{A}\sin(\omega t + \phi)$ with amplitude satisfying the equation

$$\left(\left(\omega^2 - \omega_0^2 - \frac{3}{4}\frac{\alpha}{m}\mathcal{A}^2\right)^2 + (\gamma\omega)^2\right)\mathcal{A}^2 = F^2 \tag{2.27}$$

Figure 2.7a,b shows the frequency response for an example oscillator with various duffing parameters. For strong non-linearites the solution in equation 2.27 will have three values at some frequencies. Two of these represent stable oscillation amplitudes, while the third is an unstable state. These bistable regions in frequency response of non-linear driving result in hysteresis of the frequency response of the oscillator, an example of which is shown in figure 2.7c.

The dissipation in the oscillator may also depend on the amplitude of motion. A non-linear dissipative force can be included in the equations of motion as $F = \eta x^2 \frac{\partial x}{\partial t}$, where the parameter η characterizes the strength of the non-linear damping. Non-linear damping means that the peak amplitude of oscillation no longer scales linearly with applied force, F_0, and that the characteristic timescale of the system can depend on driven amplitude (discussed further in chapter 4).

The complete equation of motion including both non-linear components is

$$m\frac{\partial^2 x}{\partial t^2} + \gamma\frac{\partial x}{\partial t} + kx + \alpha x^3 + \eta x^2\frac{\partial x}{\partial t} = F_0\sin(\omega_d t) \tag{2.28}$$

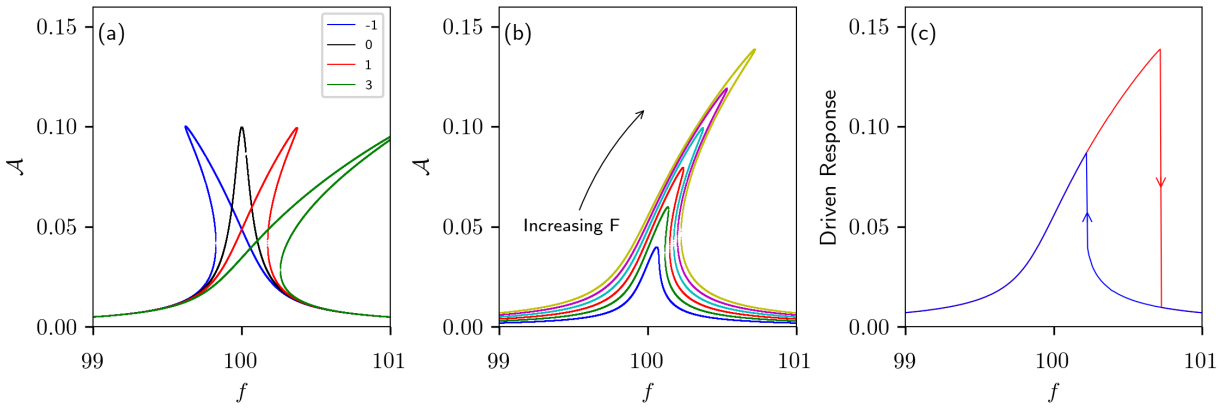

Figure 2.7: Example frequency response for a driven Duffing oscillator with $\omega_0 = 100$, $m = 1$, $\gamma = 0.1$. **a**. For fixed force $F = 1$, the effect of the Duffing parameter, α, on the amplitude response. **b**. For $\alpha = 1 \cdot 10^4$, the effect of increasing driving force from $F = 0.4$ to $F = 1.4$. **c**. The hysteretic response of a Duffing oscillator to sweeping drive frequency for $F = 1.4$, $\alpha = 1 \cdot 10^4$.

2.3.2 Euler-Bernoulli Beam Models

While the harmonic oscillator description provides a simple model of the CNT oscillations, more complete models are needed to understand the CNT motion and how it is affected by the CNT properties and experimental parameters such as gate voltage. A physical model which has shown good agreement with previous experimental results is the Euler-Bernoulli beam model [51]. This continuum model describes describes small-amplitude deflections of beams with linear elasticity. The equations describe a deflection, x, as a function of the location along the beam axis, z.

In addition to the basic beam rigidity and inertial Euler-Bernoulli terms, a few further terms are important for the CNT mechanical resonators. Gate-induced tension in the CNT can be a large factor in the beam oscillations, so a general tension term needs to be considered. The electrostatic force between the gate and the CNT is included as a uniform force, K_{elec}. Finally, a damping term is included to match the expected dissipation in experiments.

The governing equation for the CNT Euler-Bernoulli model with these components is then [52]

$$-EI\frac{\partial^4 x}{\partial z^4} + T\frac{\partial^2 x}{\partial z^2} + K_{elec} - \eta\frac{\partial x}{\partial t} = \rho A\frac{\partial^2 x}{\partial t^2} \tag{2.29}$$

where E is the Young's modulus of the CNT, $I = \frac{\pi}{4}r^4$ is the area moment of inertia of the CNT, r is the CNT radius, x is the vertical displacement of the CNT from equilibrium, $T = T_0 + \frac{EA}{2L}\int_0^L \left(\frac{\partial x}{\partial z}\right)^2 dz$ is the tension in the CNT, T_0 is the residual tension at zero applied force as a result of fabrication, $K_{elec} = \frac{1}{2}c_g' V_g^2$ is the electrostatic force per unit length, $c_g' = \frac{2\pi\epsilon_0}{h(\ln(2h/r))^2}$ is the derivative of the CNT-gate capacitance per unit length with respect to x, η is the damping factor per unit length, ρ is the CNT mass density, and A is the cross-sectional area of the CNT.

The first term in equation 2.29 describes the bending rigidity of the beam due to intrinsic stiffness. The second term describes the axial rigidity created by a tensile force. An important parameter that characterizes the relative strengths of these two terms is the critical tension, $T_c = \frac{EI}{L^2}$.

When $T \ll T_c$, the bending rigidity term is much larger than tensile term, and the CNT acts as a rigid beam. This is the expected behaviour for low gate voltages, at which the total tension is only due to residual tension. For zero gate voltage ($K_{elec} = 0$) the resonance frequency of the nth mode is given by [45]

$$f_n = \frac{\alpha_n}{2\pi L^2}\sqrt{\frac{EI}{\rho A}} \tag{2.30}$$

where $\alpha_1 = 22.4$, $\alpha_2 = 61.7$, $\alpha_3 = 120.9$.

When the tension term dominates ($T \gg T_c$) then the bending rigidity is negligible in equation 2.29 and the CNT acts as a string oscillator. For many CNT resonators, included all measured in this thesis, this is accessible at ~ 1 V gate voltage ranges. While simple estimations of the resonant frequency spectrum can be obtained in this limit, these ignore the effects of tension induced by the CNT oscillation, which is an important correction for the CNT geometries considered in this thesis. Therefore, all Euler-Bernoulli resonant frequencies are calculated numerically.

In brief, starting from equation 2.29, and assuming that the gate voltage has a small sinusoidal AC driving component and a larger static component, then the force and amplitude of motion can be decomposed

$$K_{elec} \approx \frac{1}{2}c_g'\left((V_g^{dc})^2 + V_g^{dc}V_g^{ac}\cos(\omega t)\right) \tag{2.31}$$

$$x(z,t) = u(z) + v(z,t) \tag{2.32}$$

where $v(x,t) = v(z)\cos(\omega t + \phi)$.

The tension is similarly approximated as a DC and AC component, $T \approx T_{dc} + T_{ac}$,

$$T_{dc} = T_0 + \frac{EA}{2L}\int_0^L \left(\frac{\partial u}{\partial z}\right)^2 dz \tag{2.33}$$

$$T_{ac} = \left(\frac{EA}{L}\int_0^L \left(\frac{\partial u}{\partial z}\frac{\partial v}{\partial z}\right) dz\right) \tag{2.34}$$

Substituting these decompositions into Equation (2.29) gives separate governing equations for the DC and first-order AC components of the CNT motion.

$$-EI\frac{\partial^4 u}{\partial z^4} + T_{dc}\frac{\partial^2 u}{\partial z^2} + K_{elec}^{dc} + F_{mag}\delta(z - z_0) = 0 \tag{2.35}$$

$$-EI\frac{\partial^4 v}{\partial z^4} + T_{dc}\frac{\partial^2 v}{\partial z^2} + T_{ac}\frac{\partial^2 u}{\partial z^2} + K_{elec}^{ac}\cos(\omega t) - \eta\frac{\partial v}{\partial t} = \rho A\frac{\partial^2 v}{\partial t^2} \tag{2.36}$$

The boundary conditions for the CNT resonator are taken to be clamped-clamped ($u(0) = \frac{\partial u}{\partial z}(0) = u(L) = \frac{\partial u}{\partial z}(L) = 0$). Equation 2.35 is used to self-consistently solve for T_{dc}. Assuming that coupling between resonant modes due to T_{ac} is negligible, then the resonant mode shapes are taken as an ansatz solution

$$v_{res}(z') = A_1\cos(k'_+ z') + A_2\sin(k'_+ z') + A_3\cosh(k'_- z') + A_4\sinh(k'_- z') + A_5\frac{\partial^2 u'}{\partial z'^2} \tag{2.37}$$

where $z' = z/L$, $u' = u/r$, $k'_\pm = \frac{1}{\sqrt{2}}\sqrt{\sqrt{(T_{dc}/T_c)^2 + 4(\omega/\lambda)^2} \mp T_{dc}/T_c}$, $\lambda = \frac{1}{L^2}\sqrt{\frac{EI}{\rho A}}$. Substituting this solution into equation 2.36, combined with the boundary conditions leads to a system of equations

$$\begin{bmatrix} 0 & 1 & 0 & 1 & V' \\ k'_+ & 0 & k'_- & 0 & -\frac{1}{2}F'_{dc} \\ \sin(k'_+) & \cos(k'_+) & \sinh(k'_-) & \cosh(k'_-) & V' \\ k'_+\cos(k'_+) & -k'_+\sin(k'_+) & k'_-\cosh(k'_-) & k'_-\sinh(k'_-) & \frac{1}{2}F'_{dc} \\ T'_a & T'_b & T'_c & T'_d & T'_e + \omega^2 \end{bmatrix} \begin{bmatrix} A_1 \\ A_2 \\ A_3 \\ A_4 \\ A_5 \end{bmatrix} = \begin{bmatrix} 0 \\ 0 \\ 0 \\ 0 \\ 0 \end{bmatrix} \tag{2.38}$$

$$A\overrightarrow{v} = \overrightarrow{0}$$

where $F'_{dc} = \frac{K_{elec}L^4}{rEI}$, $V' = \frac{F'_{dc}}{2k'^2}\left(\frac{k'\sinh(k')}{\cosh(k')-1} - 2\right)$, $T'_a = 4\int_0^1 \sin(k'_+ z')\frac{\partial u'}{\partial z'}dz'$, $T'_b = 4\int_0^1 \cos(k'_+ z')\frac{\partial u'}{\partial z'}dz'$, $T'_c = 4\int_0^1 \sin(k'_- z')\frac{\partial u'}{\partial z'}dz'$, $T'_d = 4\int_0^1 \cos(k'_- z')\frac{\partial u'}{\partial z'}dz'$, and $T'_e = 4\int_0^1 \frac{\partial^3 u'}{\partial z'^3}\frac{\partial u'}{\partial z'}dz'$.

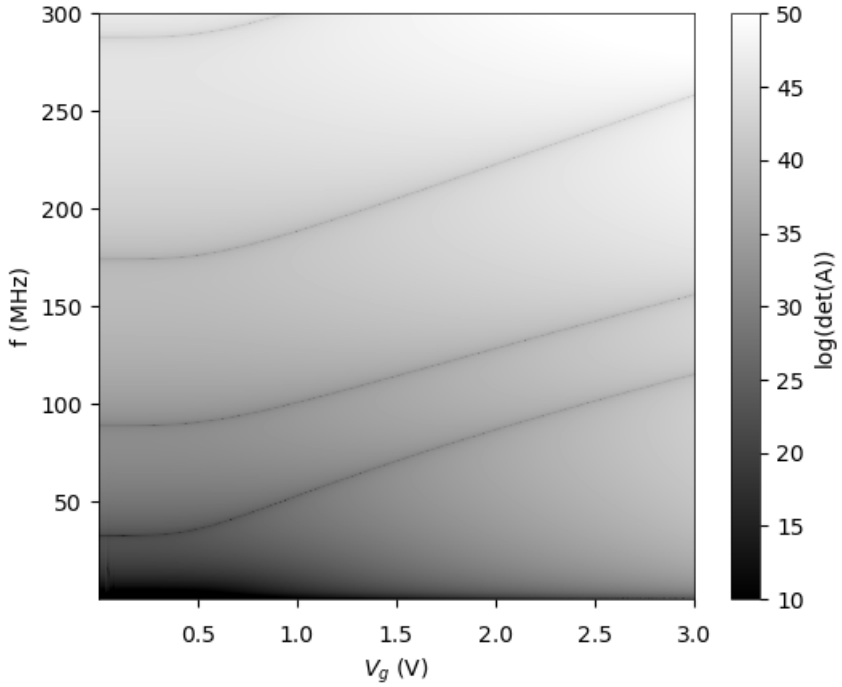

Figure 2.8: Solving the Euler-Bernoulli equations for an example CNT resonator. The determinant of the matrix A is shown as a function of frequency, ω, and gate voltage. The lines at which this determinant goes to zero give the resonant frequencies.

Frequencies which permit non-trivial solutions to equation 2.38 are the resonant frequencies of the Euler-Bernoulli beam system. Such non-trivial solutions occur only when $\det(A) = 0$. Figure 2.8 shows a plot of $\det(A)$ as a function of resonance frequency and gate voltage for an example CNT. The sharp lines of low determinant correspond to the expected resonance frequencies of that system.

Chapter 3

Fabrication of Suspended Carbon Nanotube NEMS

A consequence of the small dimensions and surface conduction of the carbon nanotube mechanical resonator is its sensitivity to contamination and contact quality. To realize the promise of CNT NEMS sensing, the pristine nature of as-grown CNTs must be preserved. The common method to achieve this is to grow the CNTs in place as the last step of the fabrication [13]. In this technique, the required contacts and gates are fabricated on a support substrate, followed by patterning of the CNT catalyst, and finally chemical vapor deposition(CVD) growth of the CNT on top of these features.

A limitation of growing the CNTs as the final step of fabrication is that all other components of the device are exposed to the high temperature CVD process. This greatly restricts the materials that can be used in the device. In particular, the typical ferromagnetic materials that can be used to create magnetic field gradients at the CNT are incompatible with the CVD process, either due to diffusion into surrounding substrate or due to their catalytic activity. Figure 3.1 show some examples of attempts to incorporate these material by encapsulating them in CVD-safe materials. After exposure to the CNT growth conditions in the CVD, all structures were damaged and often grew $\sim 100\,\mathrm{nm}$ thick amorphous carbon regions. To include incompatible materials, while maintaining a contaminant-free CNT device, the CNT can be grown on a separate substrate and mechanically transferred to the desired devices as the last step.

Due to the stochastic nature of CVD growth of CNTs, which includes random distribution of both the CNT location and electronic/mechanical properties, the suspended CNT fabrication processes do not result in high device yields. We estimate a best-case yield for

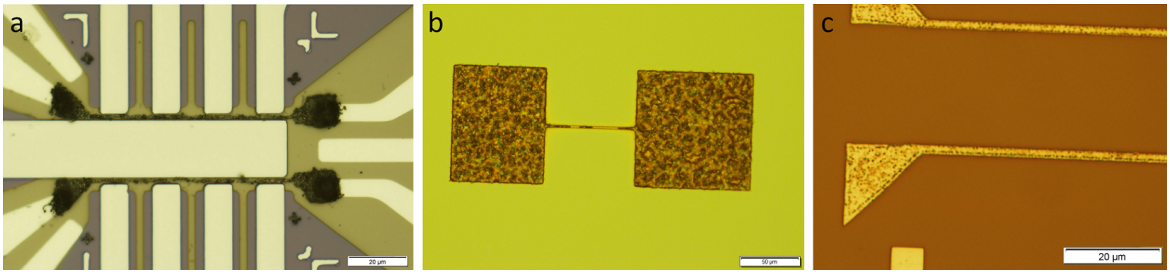

Figure 3.1: Encapsulated ferromagnetic materials after exposure to CVD growth conditions, demonstrating the damage and growth of amorphous carbon. **a** Ti/Fe/Ti fine gate structure (10/40/20 nm). **b** Permalloy(Py) test structure covered in ALD deposition of 20 nm HfO_2. **c** Py/Ti/Pt (50/10/30 nm) gate pattern.

small-bandgap suspended single wall CNT devices of $\sim 5\%$ for the geometries that will be described below [53]. To overcome the low yield, a large number of pre-patterned devices are required. Therefore, whenever feasible, full wafer processing is used. This requires the use of photolithography for most patterning, and full wafer etching and metal deposition. Any fine device patterning requiring EBL, and the small sample CVD growths, are then set as the final process steps.

This chapter details the fabrication processes that are used in the CNT device nanofabrication. First, relevant fabrication technique are described, focusing on the specific methods used for subsequent device processes. The chemical vapour deposition growth of CNTs is described, including the specific characterization and tuning that was performed to achieve useful suspended devices. Next, the nanofabrication of CVD-compatible gate and contacts for as-grown CNT devices that are measured in chapter 4 is detailed. Finally, the process for the preparation and mechanical transfer for stamped CNT devices, which are measured in chapter 5, is described.

3.1 Fabrication Techniques

This section describes the individual nanofabrication techniques that are used to create the CNT devices in this thesis.

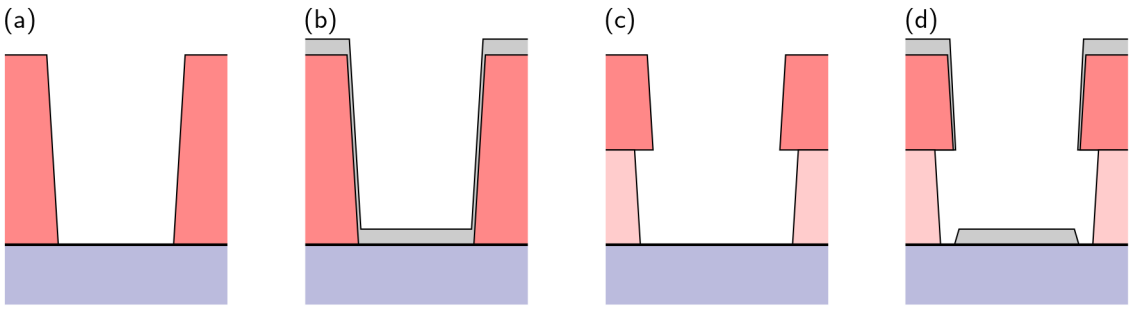

Figure 3.2: **a** Illustation of single layer photo resist cross section after development, and **b** after metal deposition. **c** The cross section of bilayer photoresist after development, and **d** after metal deposition. After liftoff, the bilayer patterned metal has sharp edges with no extra metal.

3.1.1 Photolithography

In a basic photolithography process, an ultraviolet(UV) sensitive photoresist covering the substrate is selectively exposed to intense UV light to generate a pattern of exposed/unexposed resist. The patterned illumination can be performed using predefined masks or direct-writing using spatially modulated light sources [54]. After exposure, specific solvents are used to remove either the exposed or unexposed regions while leaving the other intact. After subsequent processing as needed, the residual photoresist is removed in a lift-off solvent.

In the simplest photolithography process, a single homogeneous photoresist layer is used as the patterning agent. However, common positive photoresists typically have a slightly positive sidewall slope (85 ° to 89 ° from substrate surface) [55], which can result in difficult lift-off after metal deposition. Figure 3.2a and 3.2b show a characteristic cross section of single layer resist before and after metalization. The continuous metal film climbing the resist sidewall can lead to poor edge definition. To overcome this poor liftoff a bilayer resist can be used, in which a different underlying resist layer develops more quickly than the top layer. Figure 3.2c shows a cross section of such a bilayer after development. Figure 3.2d shows this cross section after metallization. The break in the resist profile eliminates the possibility of metal connection up the side wall, leading to reliable liftoff and clean edges which are critical for suspended CNT devices.

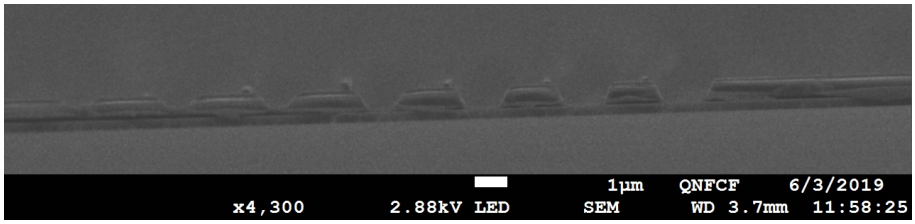

Figure 3.3: Cross-sectional SEM of 1 μm line pattern in S1811 photoresist exposed with the Heidelberg MLA150. The right-most pattern received a dose of 120 mJ/cm^2, and for each pattern to the left the dose was decreased by 10 mJ/cm^2. For doses less than 90 mJ/cm^2 the resist is not fully removed after development, preventing patterned processing. With decreasing dose, the side-wall angle also increases.

1 μm feature photolithography

To achieve 1 μm feature sizes with photolithography, both the resist and exposure method must be carefully adjusted. Best-case feature resolution for both masked and maskless photolithography is limited to approximately the resist thickness, necessitating thin resist films for highest resolution. For high resolution photolithography in this thesis, single layer Shipley S1805 resist is used, with a nominal thickness of 500 nm. At this thickness, the achievable resolution becomes limited by the resolution of the photomask or the spatial light modulation for maskless writing. The Heidelberg MLA150 in the QNCFab cleanroom facility has a specified minimum resolution of 1 μm, equal to the nominal width of the fine gate structure used in the stamped CNT devices described later in this chapter. To realize gate widths at or below this minimum resolution, the UV dosage is carefully adjusted for each resist coating. Figure 3.3 shows a cross-section SEM of 1 μm line patterns with increasing exposure dose from left to right. Under-exposed regions do not clear the resist down to the substrate resulting in no pattern transfer, while over-exposed regions create oversized features. The sidewall angle also becomes more prominent with lowering dose, such that at the minimum open feature size the sidewall has a 70° slope. The single layer resist with low angle sidewalls can make liftoff of deposited patterns difficult.

3.1.2 Electron Beam Lithography

For feature sizes below those achievable with photolithography, electron beam lithography (EBL) is used. In EBL, the patterning is analagous to photolithography, but performed using a guided electron beam and electron-sensitive resist. In the devices used in this

thesis, the e-beam resist is polymethyl methacrylate (PMMA) and exposure is performed with a RAITH150 Two Direct Write system. Achievable resolution with this system and resist is < 50 nm.

3.1.3 Metal Deposition

Thin metal films are deposited by either an IntlVac Nanochrome II-UHV electron beam evaporation system or an AJA Orion chamber magnetron sputter system.

In e-beam evaporation, an electron beam is focused onto a metal supply crucible, evaporating the metal into the ultrahigh vacuum environment. The sample to be metallized is located approximately 50 cm above the crucible. This working distance and ultrahigh vacuum environment results in deposition angles perpendicular to the surface, and therefore sharp pattern edges and easy liftoff. Typical deposition rates used for devices in this thesis are 0.5 Å/s for adhesion layer material (eg, Ti) and 1.0 Å/s for both gold and platinum.

The AJA sputtering system uses magnetron sputtering to eject metal atoms from a pure metallic target, that then bombard the sample of interest. However the diffuse transport, characteristic of sputtered deposition technique [56] means that metal is not necessarily perpendicularly incident on the sample. This can cause liftoff issues for single layer resist lithography, and shadowed edges for multi-layer resist. For this reason, sputtered deposition is only used in this thesis on unpatterned samples, with subsequent patterning and etching used to define sharp features. Sputter deposition is required in this thesis to deposit high melting point metals (Tungsten) which cannot be evaporated with IntlVac evaporation tool.

3.1.4 Anisotropic Etching

To define the trench over which CNTs will be suspended in as-grown CNT devices, as well as create the growth wafers needed for the stamping process, anisotropic etching methods are needed. These techniques are designed to etch away material in only one direction, accurately reproducing lithographically defined masks onto the underlying substrate and leaving sharp feature edges that are important for suspended CNTs. Reactive ion etching is used for bulk removal of SiO_2, while ion milling is used to etch inert metal films.

Ion Milling

Ion milling refers to the physical etching of thin films via high energy ion bombardment of the surface. This technique is much less sensitive to the material being processed than chemistry-based etching methods. The ion milling rates of most materials present on our samples vary by less than an order of magnitude. Ion milling is used in the device processing in this thesis to etch films which cannot easily be removed via reactive ion etching, such as the inert platinum metal top layer. The ion milling process is performed in an AJA ATC-2030-IM with 220m RF argon ion source. All patterned processing is done with normal ion incidence to get sharp pattern transfer to the etch pattern.

The ion bombardment used to eject atoms from the film surface also transfer a lot of thermal energy into the sample. The sample is mounted to a water cooled platter to remove some of this energy, but prolonged bombardment can still significantly raise the substrate temperature. For patterned etching this heating can damage the resists used, making later removal exceedingly difficult. Figure 3.4 shows an example of etched contacts in which the resist was damaged. The heavily cross-linked resist which formed at the pattern edges cannot be removed without risking surface damage to the contacts. To avoid the thermal damage in the etching processes used in this thesis, all ion milling was operated at a 4% duty cycle, with the ion source shutter closed for 115 s after every 5 s of exposure. When combined with a thermally robust photoresist (MaN-1410) and improved thermal contact to the cooling platter via thermal paste, this process allowed for repeatably clean removal of resists after etching.

Reactive Ion Etching

Etching of both the thermal SiO_2 layer in section 3.3 and the quartz wafer in section 3.4.2 was performed using an Oxford Instruments ICP380 plasma-based dry etching system. The etching process starts by exciting reactive gases using an RF-field in a vacuum chamber. The excited gas molecules form a stronger bond than the Si-O bonds in the oxide to be etched, and can thus remove the exposed oxide surface. In addition to this reactive component, the RF field accelerates these ions into the surface in a similar manner to the ion milling process. For correct gas pressures and ion conditions, the combined bombardment and reactivity is needed to etch the materials, allowing for rapid anisotropic material-selective etching. The SiO_2 etching in this thesis uses a O_2:C_4F_8 etching process (15:40 sccm) with 200 W RF power for a SiO_2 etch rate of approximately 340 nm/min.

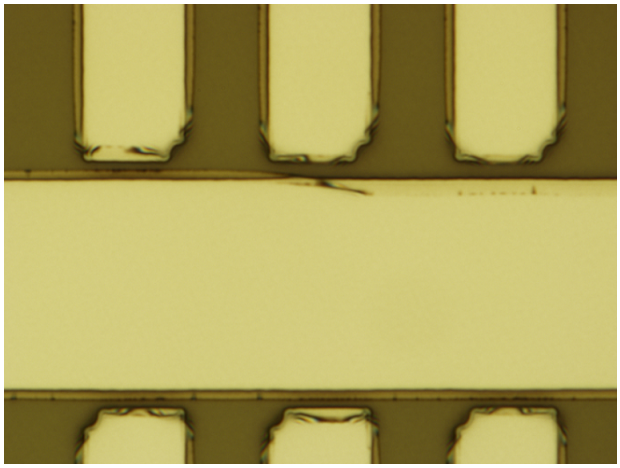

Figure 3.4: Artifacts at the edge of the metal patterns due to resist damage during ion milling and reactive ion etching processing.

3.2 Chemical Vapour Deposition

Of critical importance in the realization and performance of single suspended CNT devices is the growth of defect-free, small diameter single-wall CNTs. This is best achieved using chemical vapor deposition (CVD) [57]. In the basic CNT CVD process, a hydrocarbon precursor such as CH_4 or C_2H_4 reacts with a transition metal catalyst at elevated temperatures. The precursor gas is chemically decomposed by the catalyst, and the resulting carbon atoms are absorbed onto the metallic nanoparticle. Eventually the nanoparticle surface saturates and additional carbon nucleates and grows the CNT, as depicted in figure 3.5.

For well configured CVD processes the thermal decomposition of the precursor is minimal, and decomposition occurs only at the catalyst [58]. This means that device regions without catalyst are not active in the growth, and should not become contaminated with amorphous carbon. For the CVD growths in this thesis, the catalyst is patterned into $\sim$ 1 μm regions and CNT are selectively grown at these sites. The catalyst coated region will have large numbers of crossing CNTs, and so the CNTs of interest for suspended devices are those which grow as long straight nanotubes outward from these island.

There are many variables that influence the quality and quantity of CVD growth of CNTs. The most important for single defect-free growth are the composition of the catalyst, the supporting substrate, the process temperature, and the process gases.

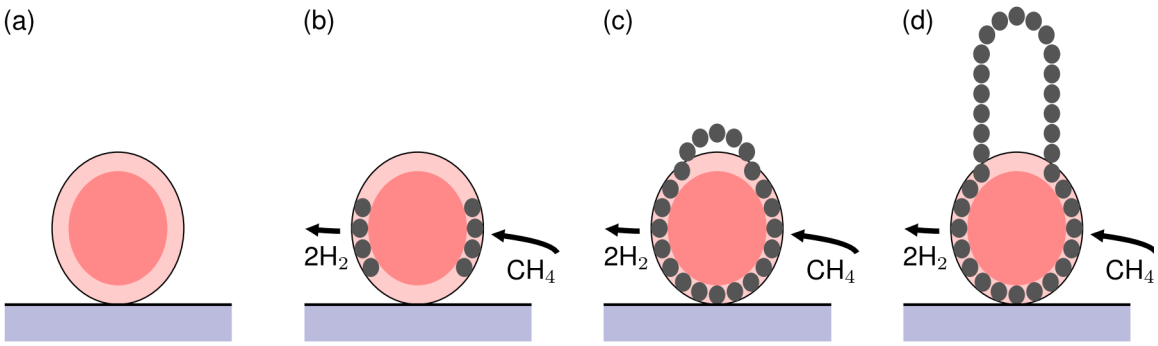

Figure 3.5: The vapour-liquid-solid growth mechanism of CNTs in CVD, as described in [58]. **a** The transition metal nanosphere resting on a supporting substrate before introduction of carbon precursor. **b** Catalytic decomposition of the precursor gas and carbon absorption results in carbon atoms on the outer shell of the catalyst. **c** The carbon oversaturates the nanosphere and a CNT begins to form. **d** The outward growing carbon atoms rapidly absorb additional atoms, forming a carbon nanotube.

The composition of the transition metal catalyst has a major influence on the resulting CNTs. The metal must have sufficient carbon solubility and catalytic activity at the growth temperatures to rapidly decompose the precursor and absorb the carbon atoms, to begin the CNT growth process [58]. The two metals which exhibit excellent CNT growth are iron and cobalt, which both have high carbon solubility at the typical CVD temperatures, 800°C - 1000°C [59].

Selectively growing small diameter single-wall CNT can be realized by introducing secondary metals to alter the reaction of the primary catalyst material. Molybdenum is commonly used for this purpose. Pure molybdenum as a catalyst will not grow CNTs due to the formation of Molybdenum-carbide states preventing the CNT nucleation. However, adding $< 8\%$ atomic concentration of molybdenum to iron catalyst create Fe-Mo alloy with higher carbon solubility than pure iron. The higher carbon solubility allows smaller catalyst material clusters to nucleate and form CNTs before being "poisoned" by amorphous carbon generated during precursor decomposition [58].

Interactions between the catalyst materials and the supporting substrate can affect the catalyst reactivity and therefore CNT growth [60]. For example, catalyst supported on metal substrates can form strong catalyst-support bonds, inhibiting carbon absorption and thus CNT nucleation. Supporting the catalyst metals on silica or alumina nanobeads can

reduce support-catalyst interaction, and remove substrate dependence of catalytic activity making growths on different materials behave similarly. Nanobead-supported catalyst also allows for easier patterning/dispersion of the catalyst metals without clumping.

The temperature of the CVD process predominately influences the rates of precursor decomposition and carbon absorption. At too low temperatures, the decomposition of the precursor gas will be slow or completely absent resulting in only low density, short CNTs. At exceedingly high temperature, thermal decomposition of the precursor begins to occur, leading to amorphous carbon deposition across the device. Within the usable temperature range, the main impact of temperature is too alter the available diameters of CNTs grown. At lower temperatures, large catalyst clusters do not decompose precursor fast enough to nucleate CNT growth meaning only small diameter CNTs are grown. Increasing temperature allows increasingly large catalyst material to grow CNTs, thus increasing overall CNT density and average diameter.

The ratio of gases in the CVD process will control the decomposition and absorption of carbon at the catalyst material. The ideal behaviour is for the hydrocarbon precursor to decompose completely, and for all carbon atoms to absorb onto the catalyst while non-carbon components recombine and flow out of the chamber. If the carbon concentration is too high, free carbon radicals will not all associate with the metal catalyst and amorphous carbon can form across the device [58]. If the carbon concentration is too low, the CNT growth will be starved for carbon atoms, resulting in only short, high-defect CNTs. To achieve high quality CNT growth it is therefore beneficial to use a suitable precursor, such as CH_4, then tune the C-H balance using additional flow of H_2 gas.

3.2.1 Characterization of CNT growth

In the process of adjusting CVD growths for suspended CNT devices, a number of characterization tools were used. Rapid measurements of bulk growth using Raman spectroscopy allows for rough tuning of the CVD growth, while fine tuning for individual CNT quality made use of slower scanning electron microscopy and atomic force microscopy.

Resonant Raman spectroscopy is a fast, non-destructive technique for CNT characterization. The resonant Raman spectrum can quickly provide basic information on CNT structure. The G-band ($\omega \approx 1600\,\mathrm{cm}^{-}1$) arises from optical phonon between the A-B carbon atoms in the graphene lattice, and is a common first-signature of graphitic material presence [61]. The D-band ($\omega \approx 1350\,\mathrm{cm}^{-}1$) and 2G-band ($\omega \approx 3200\,\mathrm{cm}^{-}1$) result from double-resonant Raman processes that are enhanced by defects in the CNT structure. In ultra low defect CNTs this band becomes very weak with only a small residual peak from

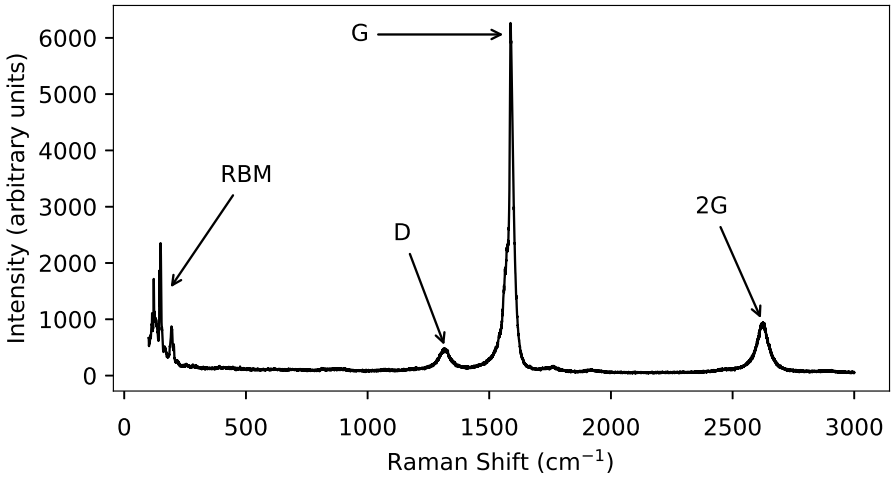

Figure 3.6: The Raman spectrum measured on an example CNT growth, with the CNT-relevant peaks labelled. The G and RBM peaks indicate the presence and approximate properties of CNTs in the film, while the D and 2G peaks provide a measure of defect density.

two-phonon processes that occur independent of defect density. Therefore the ratio of the integrated D peak intensity to the G peak intensity provides an approximate first measure of CNT quality. The radial breathing modes (RBM) ($\omega \approx 100 - 300\,\mathrm{cm}^{-}1$) are a result of "breathing" of the CNT as the entire lattice vibrates radially. Its presence is a strong signature of the CNT structure, and the RBM frequency provides an estimate of the CNT diameter [62], with the relation

$$\omega_{RBM} = \frac{c_1}{d} + c_2 \tag{3.1}$$

where $c_1 = 215 - 260\ \mathrm{cm}^{-1}\mathrm{nm}$ and $c_2 = 0 - 20\ \mathrm{cm}^{-1}$. Figure 3.6 shows an example Raman spectrum from a CNT growth labelling the relevant peaks.

As the CNTs of interest for suspended devices are those which grow individually away from the catalyst sites, a technique for evaluating these is needed. While micro raman techniques have been used to measure individual CNTs before [63], for our purposes a higher throughput evaluation using scanning electron microscopy (SEM) is needed. Figure 3.7 shows an example SEM image from a CNT growth. The CNTs outside of the catalyst islands can be individually resolved. The length and quality of these CNTs can be estimated, with mechanical kinks/bends being indicative of local CNT defects. The SEM process damages the CNTs so it is only used on test samples or after other measurements

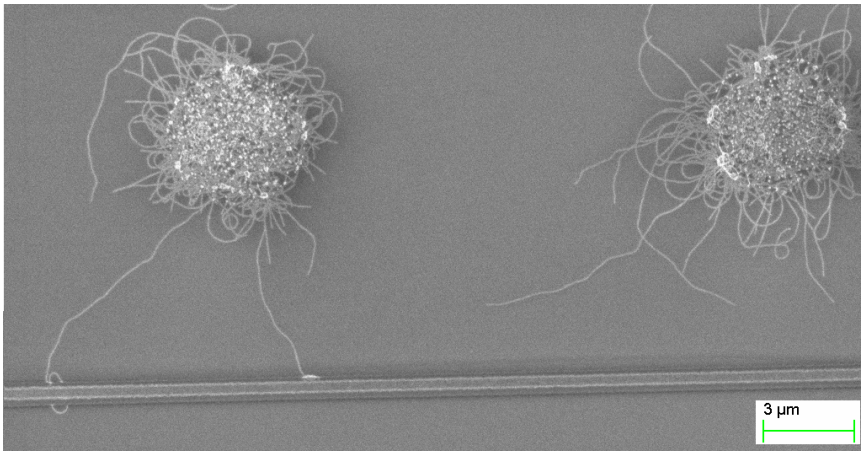

Figure 3.7: Scanning electron microscopy (SEM) image of a test growth of CNTs. Two patterned catalyst regions are shown in the upper half of the image, along with a large number of CNTs growing on and around these regions. Two CNTs growing out of the left catalyst island terminate at a Ti/Pt reference bar along the bottom of the image.

are completed.

Another technique to analyze individual CNTs is atomic force microscopy (AFM). The main advantage of AFM is that it provides precise measurement of CNT diameter. Figure 3.8 shows an example AFM image of CNT growth near patterned catalysts. The AFM diameters in this example range from 1.1 nm to 2 nm. The speed/throughput of AFM is much lower than Raman and SEM characterization, so it is typically used only for specific growth/CNT characterization.

3.2.2 CNT growth recipe

The CVD system used for the devices presented in this thesis is an atmospheric-pressure thermal CVD. The CNT growths are performed using a methane gas precursor, with Argon and Hydrogen gas flows during temperature ramping and growth processes as needed. All growths use a Fe-Mo-Co catalyst composition, details of which are given in appendix B.

Of critical importance in achieving clean CNTs is proper preparation and conditioning of the CVD. In addition to the potential transfer of contaminants directly to the sample, any contaminant material in the quartz tube reaction area can also lead to precursor decomposition, resulting in free carbon atoms that deposit as amorphous carbon across

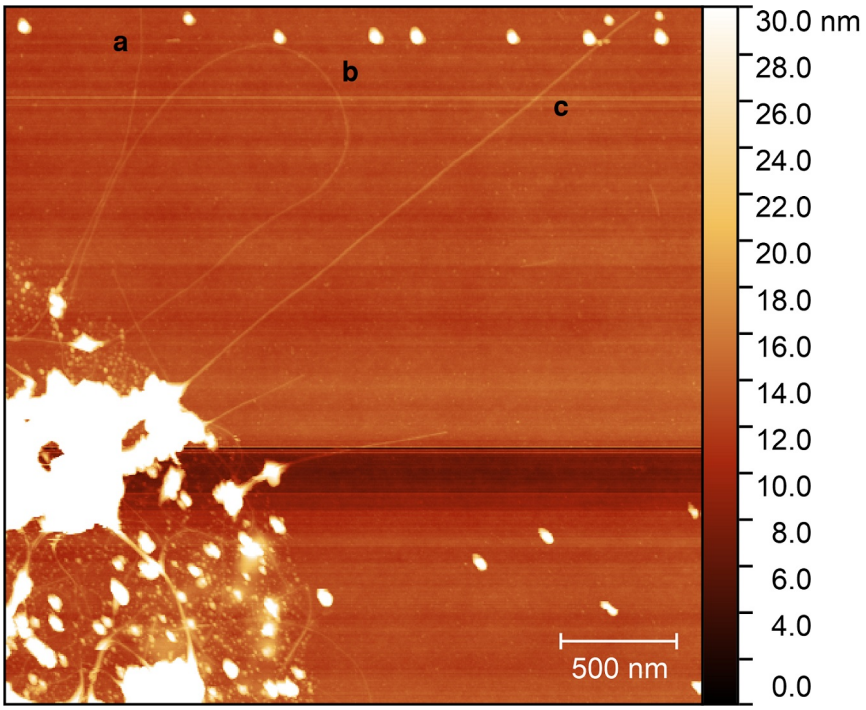

Figure 3.8: AFM image of CNTs growing near a patterned catalyst region (lower left). This image was measured using a Bruker Dimension Icon AFM in peak force tapping mode. The labeled CNTs are of heights **a** 1.1 nm, **b** 1.4 nm, **c** 2 nm.

the devices. Incomplete conditioning of the furnace can leave "trap" sites, which capture process gases, resulting in inconsistent gas quantities at the growth sites. For these reasons, every CVD growth is preceded by a cleaning-conditioning process, detailed in appendix B.

The CVD process was initially adjusted by measuring the effect of changing growth conditions on the Raman spectra measured at the CNT catalyst region. Figure 3.9 shows a series of Raman spectra for these growths. Initial growth attempts resulted in high defect densities and weak RBM signal. Refining the precursor, gas flow rates, temperature, and C:H ratio improved both of these Raman properties, eventually resulting in very small D peak and sharp RBM signals indicative of low-defect single-wall CNT with diameters in the $0.8 - 1.4$ nm range (shown in figure 3.9c). The CVD process used for this final Raman-tuned CNT growth was

1. Purge: At room temperature, purge growth chamber with 400 sccm H_2 and 600 sccm Ar (3 minutes)
2. Warm up: Ramp temperature to 850 °C under 400 sccm H_2 and 600 sccm Ar (20 minutes)
3. Growth: While holding temperature at 850 °C, flow 1000 sccm CH_4 and 400 sccm H_2 (20 minutes)
4. Cool down: Turn off heating elements and let process chamber cool to 80 °C under 400 sccm H_2 and 600 sccm Ar (60 minutes)

However, when this raman-tuned CVD process was used to grow CNTs across test device structures that replicated the design dimensions for suspended devices, a very low yield ($< 1\%$) of devices had CNTs bridging between contacts. When contact bridging was achieved however, AFM imaging of the contact gap revealed long, straight, ≈ 1 nm diameter CNTs as desired for suspended devices.

An explanation for the low device yield is that while Raman measurements can identify low defect concentration and a measure of CNT density, it is a large area measurement over the catalyst region while the CNT devices of interest rely on CNTs that grow long distances outward from the catalyst. The conditions which increase overall CNT density at the catalyst do not necessarily lead to such growths. Thus, further refinement of the growth conditions was needed with a focus on those CNTs which would create the devices of interest.

Figure 3.10a shows a representative SEM image of a test pattern of catalyst islands after CVD growth using the above Raman-tuned process. While straight CNT growing

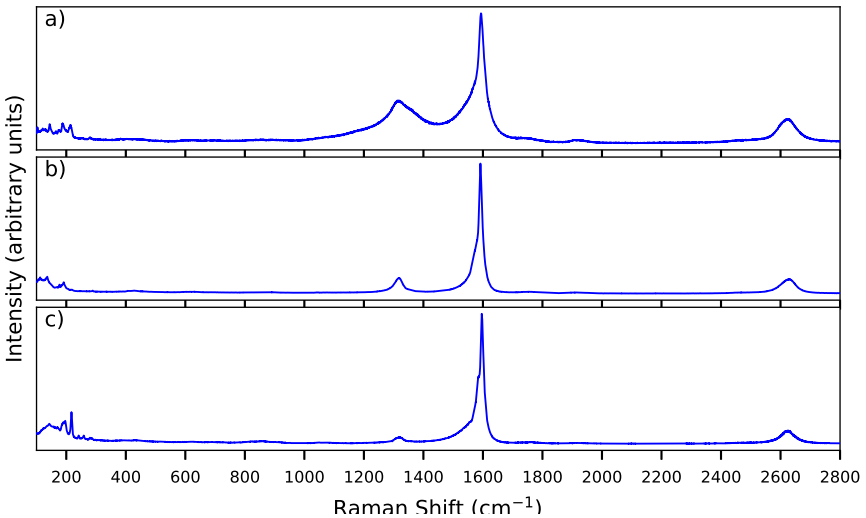

Figure 3.9: Raman spectra of CNT films for various CVD growth conditions. **a** Using an ethylene precursor recipe resulted in a large amount of defects. **b** Switching the precursor to methane greatly improved the CNT quality. **c** Further refinement of the CVD growth parameters using the methane precursor achieved very low defect densities, and strong RBM peaks around 200 cm^{-1}.

outward from the catalyst are seen on these test patterns, the length and quantity of such CNTs is low.

It is expected that the CNT growth process has an initial time delay, as the catalyst material is broken down to active metal clusters and the precursor is first decomposed and absorbed onto the catalyst, followed by very rapid nucleation and growth of the straight CNT section [58]. After the initial growth, the CNT collapses to the surface and any additional growth of that CNT is greatly impacted by the adjacent surface, resulting in high-defect "snaking" CNT sections that are not relevant for suspended devices. However, the catalyst material breakdown dynamics are not well quantified, and whether active catalyst can be formed long after initial breakdown (eg, due to changing size) is unknown. The growth time was changed to observe it's impact on quantity of straight CNTs grown outward from catalysts. Further increasing growth time up to 60 minutes or decreasing down to 10 minutes had no significant impact on the outward growing CNTs. However, decreasing growth time to 5 minutes noticeably decreased the CNTs quantity and length around catalyst, see figure 3.10b, as well as the Raman peak intensity, suggesting $\geq$ 10 minute growth times are required to activate all catalyst.

To improve the long, straight CNT growth further, fine tuning of the C-H balance was performed. The CH_4:H_2 gas flows during the growth step were tested at a number of ratios, from the 5:2 ratio above to 1:1. Figure 3.10c shows an example SEM of a growth using a 1:1 ratio (400 sccm CH_4). While CNT growth away from the catalyst is very prevalent, the CNTs are mostly high-defect growths.

The best C-H ratio was found to occur at 750 sccm CH_4 : 440 sccm H_2 gas flow. Figure 3.10d shows an example SEM of such a growth, in which multiple straight CNTs are observed. Using this tuned CVD for representative device geometries, contact bridging yield of $\sim$ 5% was observed, comparable to device yields achieved for similar gap sizes in literature [53]. This final CVD process is then:

1. Purge: At room temperature, purge growth chamber with 440 sccm H_2 and 600 sccm Ar (3 minutes)
2. Warm up: Ramp temperature to 850 °C under 440 sccm H_2 and 600 sccm Ar (20 minutes)
3. Growth: While holding temperature at 850 °C, flow **770** sccm CH_4 and **440** sccm H_2 (10 minutes)
4. Cool down: Turn off heating elements and let process chamber cool to 80 °C under 440 sccm H_2 and 600 sccm Ar (60 minutes)

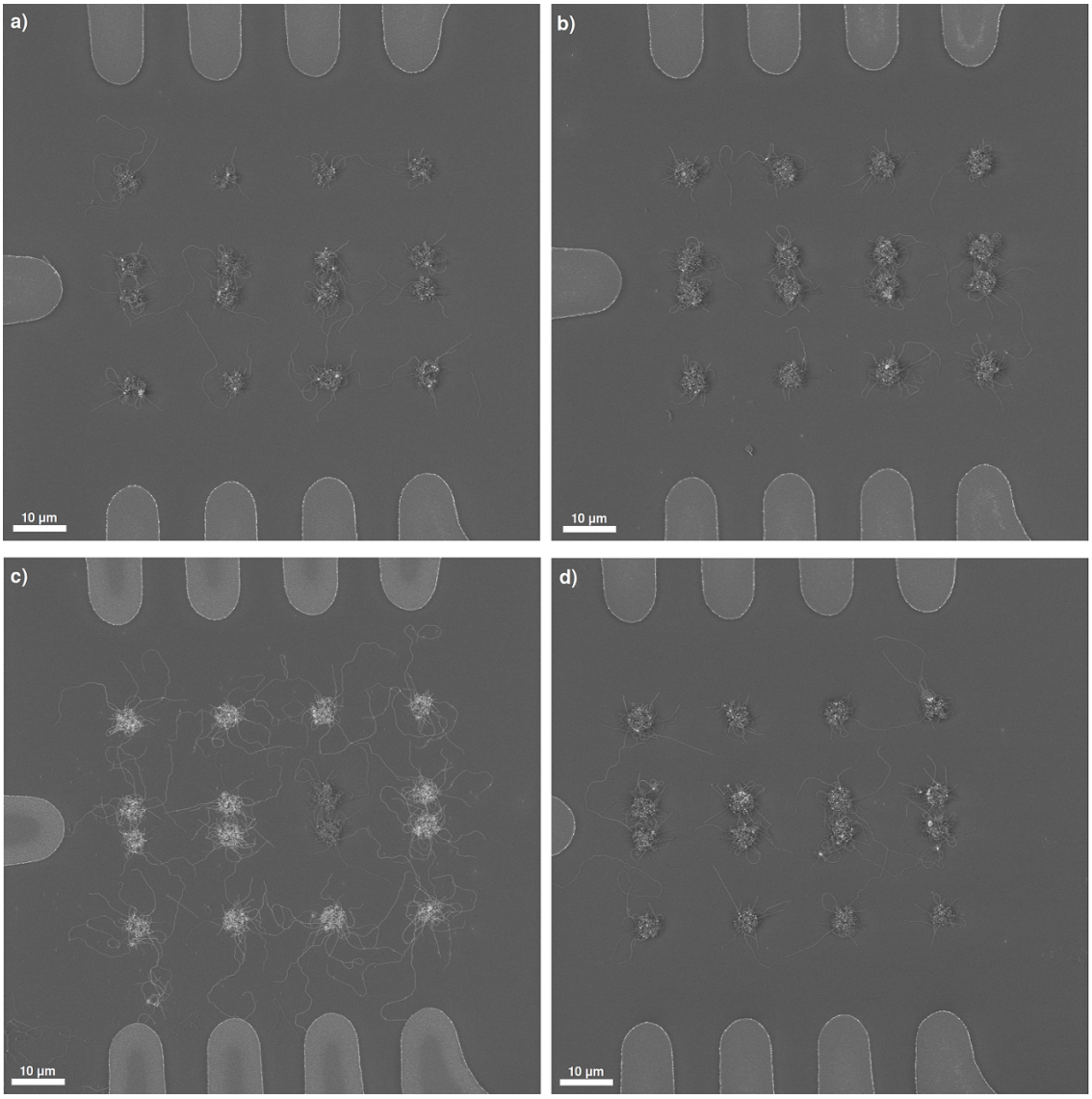

Figure 3.10: Representative SEM of different CVD growths of carbon nanotubes on silicon substrates. **a** The original Raman-tuned CVD recipe produced some straight CNTs suitable for suspension, but quantity and length are both low. **b** For growth times less than 10 minutes, fewer CNTs growing away from the catalyst regions were observed. **c** Increasing the ratio of C atoms with respect to H present during growth increases CNT quantity and length but results in high defect growths not suitable for suspended device. **d** At the proper C:H ratio, several long straight CNTs are achieved near each catalyst site, with minimal growth of high-defect CNTs.

For the mechanical transfer devices described in section 3.4, the gap between growth surfaces was increased from 2 μm to 6 μm. Using the same CVD process at 850 °C resulted in $\ll 1\%$ suspended CNT yield. To increase this yield, the CNT growth for those devices was run at a process temperature of 950 °C with all other parameters unchanged. This results in a higher average diameter of CNTs, but improved the device yield to $\sim 2\%$.

3.3 As-grown suspended CNT devices

This section describes the fabrication of the suspended CNT devices with the CNT grown as the last step across predefined contacts. Figure 3.11 shows the design of the devices. Each full wafer consists of 60 1 cm by 1 cm device chips, with each chip having 30 device areas. Each device area has a single drain contact and eight individual source contacts, resulting in 240 potential devices per chip. The raised metal source/drain contacts abut a deep trench over which the CNT will be suspended. A local gate is placed at the bottom of this trench by electron beam lithography.

The CNTs are grown as the last step. To selectively grow CNTs at the contact crossing of interest, small holes are patterned via photolithography on each contact near the trench, and the catalyst material is drop-cast. After liftoff of the photoresist, small islands of catalyst are all that remain. The islands are positioned approximately 2 μm away from the trench edge. This separation is designed to prevent the many short CNTs grown close to the catalyst from collapsing into the trench, where they could create shorts between the source/drain and the gate.

Contact Metal Selection

The materials used in this device are critically important, particularly for the surfaces that will make electrical contact to the CNT. In addition to the effect of various metal work functions on the CNT-metal interface, the physical condition of the metal surface after the high temperature CVD process will affect the electrical contact quality and mechanical clamping strength. Figure 3.12 shows atomic force microscopy scans of platinum surfaces before and after exposure to the CVD growth procedure, for two different adhesion layers (titanium and tungsten). Prior to the CVD process, both surfaces have similar RMS roughness of $0.3 - 0.4$ nm. While both adhesion layer-platinum stacks survive the 850 °C CVD process, the titanium-platinum stack roughness increases to 1.1 nm while the tungsten-platinum roughness is unchanged, making tungsten-platinum preferable for the

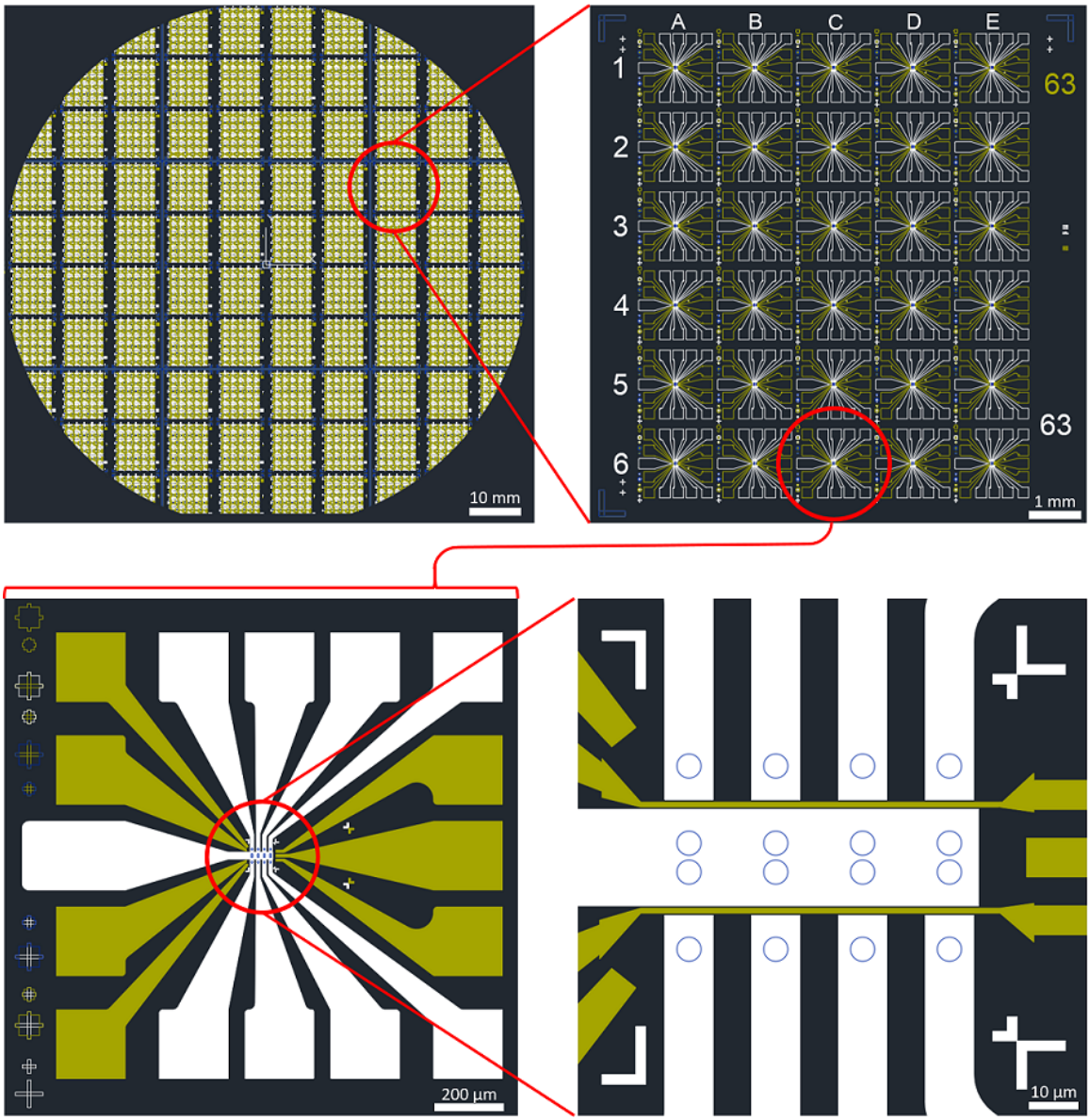

Figure 3.11: Design of the as-grown suspended CNT device pattern. A full 4" wafer is processed to increase the quantity of final device chips for CVD growth. A single 1 cm by 1 cm device chip is shown in the second panel. The third panel shows the wire bonding pad layout of a single device from that chip, and the final panel focuses on the active device region. The background substrate surface is shown in dark blue. The upper surface source/drain contacts are indicated in white, and the recessed gate electrodes are shown in yellow. Blue circles in the fourth panel indicate the location for CNT catalyst material deposition.

source/drain contacts to the CNT. The tungsten-platinum processing does require sputtering deposition, and so is performed on the unpatterned wafer as the first step, followed by etching to define the contact geometry.

The fabrication process for as-grown CNT devices, used in chapter 4, is (further details in appendix A):

1. Start with undoped silicon wafer with 300 nm SiO_2 thermal oxide
2. Deposit 10 nm tungsten and 20 nm platinum using AJA sputter deposition
3. Source/Drain definition by photolithography, followed by ion milling of W/Pt and reactive ion etching of SiO_2 to a total depth of ≈ 270 nm
4. Ti/Pt (10/30 nm) gate bond pads deposited by photolithography and e-beam evaporation
5. Cleave wafer into smaller sections for further processing
6. Ti/Pt (10/30 nm) fine gate deposition by electron beam lithograph and e-beam evaporation
7. CNT Catalyst Deposition as described in text
8. CVD growth of CNTs

Figure 3.13 shows an optical image of a completed device before CNT growth.

3.4 Mechanical Transfer Suspended CNT Device

While the above nanofabrication process can create clean suspended CNT devices, it restricts the device design and material choices to those which survive the CVD process. In this section, a mechanical transfer (stamping) technique is presented that overcomes this restriction by separating the final device sample from the growth substrate [41, 64].

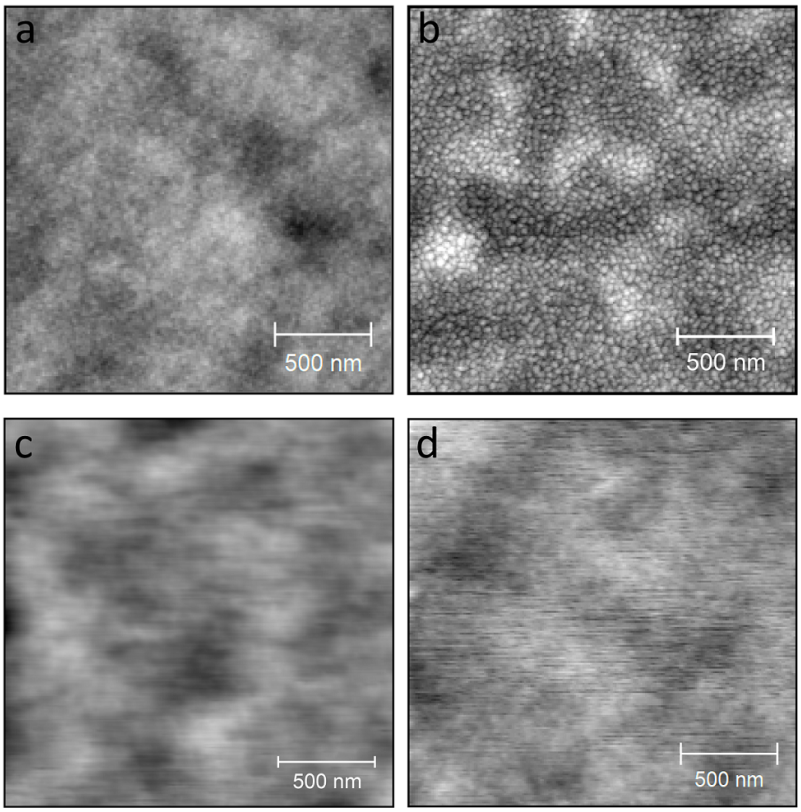

Figure 3.12: AFM images of contact metal surfaces after CVD exposure. **a** Ti/Pt surface before CVD, with RMS roughness 0.3 nm. **b** Ti/Pt after CVD growth recipe. RMS roughness is increased to 1.1 nm. **c** W/Pt surface before CVD growth, and **d** after CVD exposure. Both surfaces has RMS roughness of 0.4 nm. Color axis (black to white) is 4nm in **a**,**c**,**d**, and 8nm in **b**.

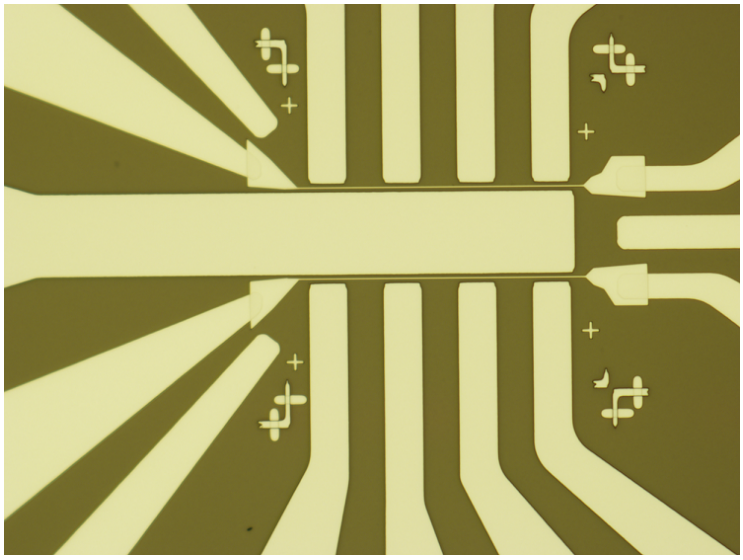

Figure 3.13: Optical microscope image of a finished as-grown CNT device before CNT growth.

3.4.1 Device Wafer

In this process, the sample chips that will hold the final device can be designed as desired. The main restriction imposed on the device pattern by the stamping process is a limit on the width of the contacts. The mechanical transfer requires the growth wafer surface to travel past the contact interface, and so there must be recessed regions adjacent to the contact surface. To have a practical yield of suspended devices on the growth wafer the separation between growth regions, and therefore the maximum distance to the outside of all contact surface on the device wafer, should be minimized. In our transfer process this is also impacted by 1 μm alignment tolerances of the transfer tool, as misalignment in any region of the chip can cause the growth surface to collide with device chip and prevent any CNT transfer across the whole chip. The final design for these devices has a 6 μm gap between the growth surfaces on chip, and a 4 μm restriction on the outer contact dimensions.

Figure 3.14 shows the design of the chip used for the devices that are measured in chapter 5. Each chip contains 136 potential devices. The right panel of figure 3.14 shows a focus on the active region of one such device, including the nominal location for the quartz wafer to hit the substrate during stamping.

The freedom in contact metal selection allows for a process in which the trench between

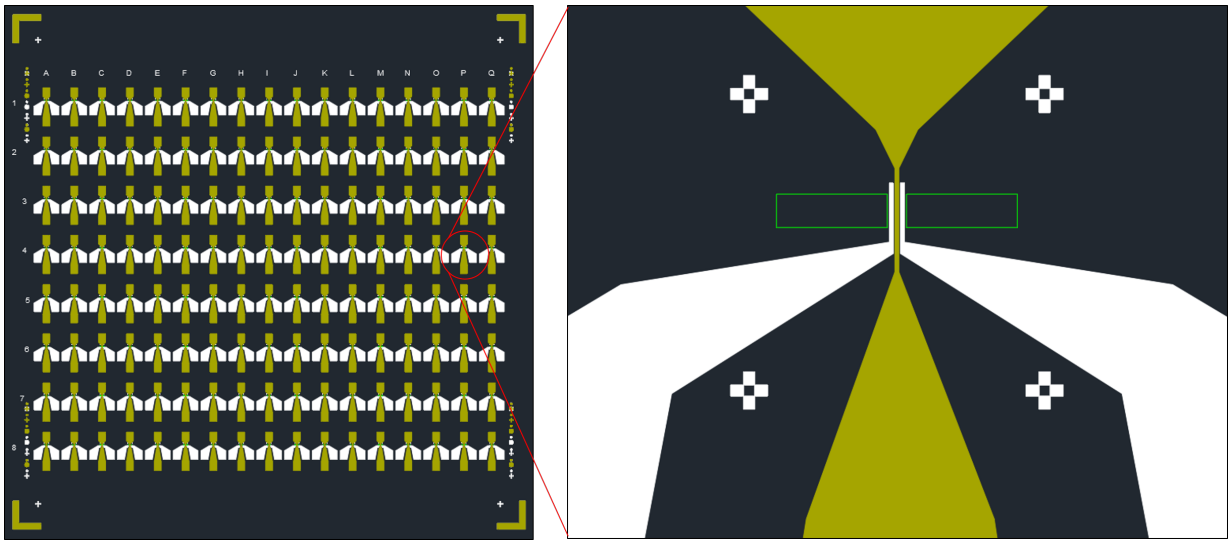

Figure 3.14: The pattern design for a single 1 cm by 1 cm chip for the device side of the stamped CNT devices. The left panel shows all 136 potential device areas and outer reference/alignment features used during processing/stamping. The right panel shows a close-up of one active device area. The thick source/drain contact are shown in white. The recessed gate is shown in yellow. The green rectangles indicate the designed location for the quartz pillar contact during aligned stamping.

source/drain contacts can be defined solely by thick metal deposition of the contacts, avoiding the potentially damaging anisotropic etching required in the as-grown CNT device process. This also allows for the fine gate structure to be deposited prior to the trench creation, smoothing the resist profile for this gate lithography and allowing all-optical patterning of these devices, avoiding costly electron beam lithography.

The final iteration of the fabrication process for these device chips is then (further details in appendix A)

1. Start with undoped Si wafers with 300 nm SiO_2 dry thermal oxide
2. Deposit 60 nm thick nickel gate via single layer 1 μm photolithography and e-beam evaporation.
3. Deposit thick Ti/Au (40 nm/360 nm) source/drain contacts by photolithography and e-beam evaporation. Note this process requires alignment beyond MLA150 specifications, so optical inspection of developed patterns should confirm alignment.
4. Dice wafer into individual 1 cm by 1 cm chips for CNT transfer

Figure 3.15 shows an optical image of an active device region from a completed fabrication process.

3.4.2 Quartz Growth Wafer

The requirements on the CNT growth wafer are

- Optically transparent - The mechanical transfer requires optical alignment of opposing wafer faces
- CVD compatible - This wafer will undergo the CNT growth and must have no reaction outside of the designed catalyst locations
- Large upper/lower surface separation - Only the specified CNT growth surface should contact the device chips during transfer

Figure 3.16 shows an overview of the quartz wafer design. The pillars that will be used for growth surfaces are defined by reactive ion etching. To avoid any damage to the growth surface during etching, an Aluminum mask is used. This aluminum layer would react during

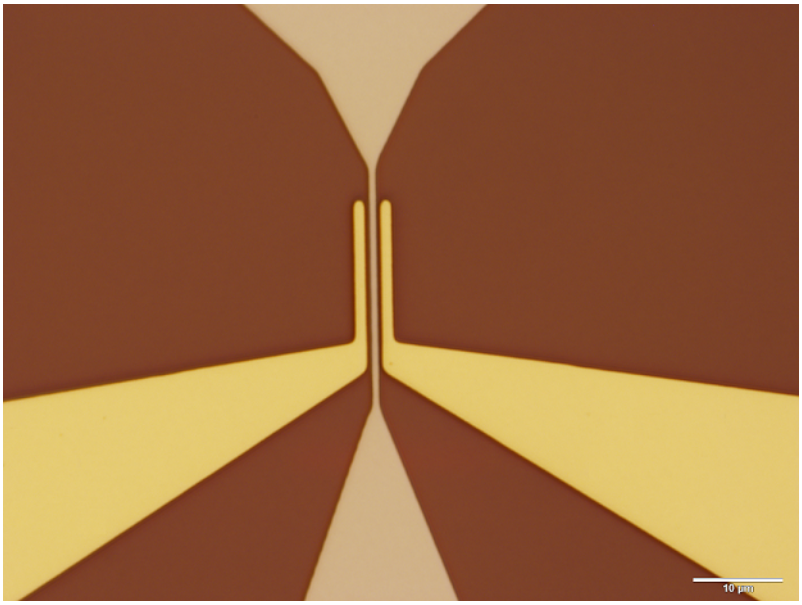

Figure 3.15: Optical image of the active device region of a device chip after fabrication, prior to CNT transfer.

CVD, so must be removed prior to CNT growth. Therefore an aligned platinum layer is deposited after pillar etching, on the lower non-critical surface, to give an optical reference which is used for alignment during transfer. After removing the aluminum layer, the wafer is spin coated with a resist material for patterning of catalyst deposition.

It is favorable for device yields to get the catalyst material exactly to the edge of the etched pillars, so the physical etched profile is taken advantage of in defining the catalyst pattern. In place of exposure-based lithography, the resist is slowly etched across the full quartz piece. Due to the profile of the etched quartz during resist spinning, the resist thickness atop the pillar is lower than that of the lower surface resist. Therefore, with calibrated etching the top of the pillars can be exposed while all lower level regions remain covered. Then, the catalyst material is spun across the pieces, the resist is removed by liftoff and the remaining quartz pieces have catalyst covering the entire upper surface with no deposition on lower surface. These pieces then undergo CVD growth of CNTs and are ready for the transfer.

The quartz growth wafer fabrication process is (further details in appendix A):

1. Start with a 4” z-cut quartz wafer

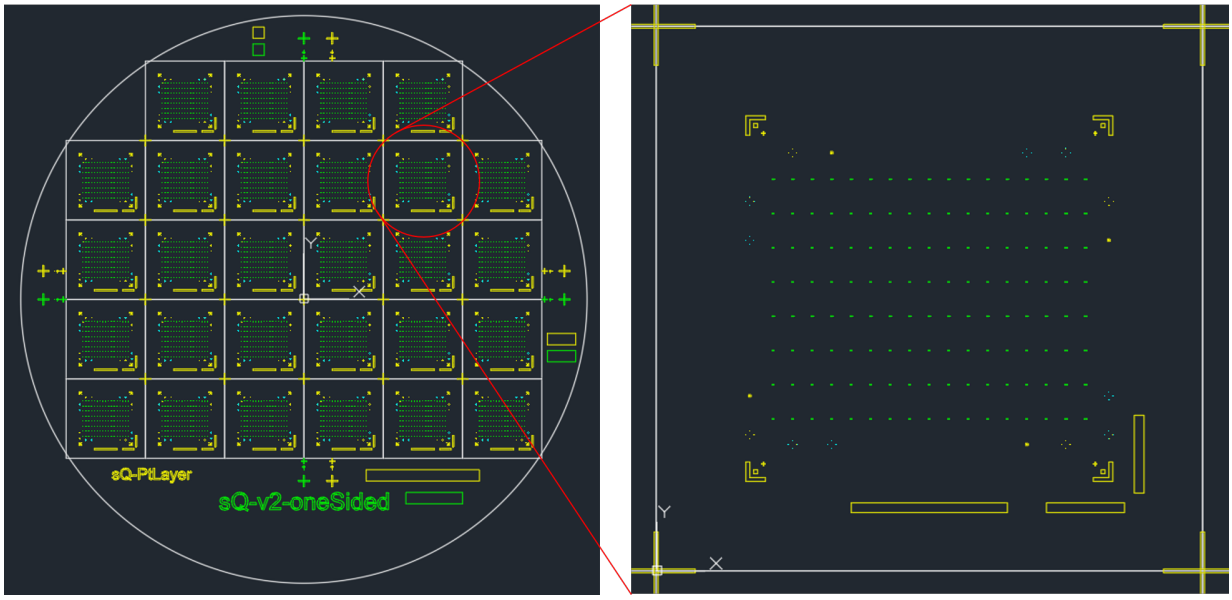

Figure 3.16: The pattern used for the quartz growth substrate for stamped CNT devices. A full wafer, including labels and reference markers, is shown in the left panel. Prior to CVD growth of the CNTs, the wafer is diced into 1.4 cm by 1.4 cm chips, one of which is shown on the right. The green outlines depict the unetched regions that form the upper/growth surface. The yellow outlines are the Ti/Pt pattern deposited on the lower surface and used for optical reference during stamping.

2. Deposit 200 nm thick aluminum etch mask using photolithography and e-beam evaporation
3. Etch 1.4 μm using reactive ion etching
4. Define Ti/Pt (10 nm/30 nm) alignment pattern by photolithography and e-beam evaporation
5. Remove aluminum etch mask
6. Spin-coat full wafer in PMMA 950 A6
7. Dice full wafer into 1.4 cm by 1.4 cm pieces
8. For each piece before growth:
   (a) Partially etch PMMA to expose upper surface, spin coat catalyst solution, and liftoff PMMA
   (b) CVD growth of CNTs with 950 °C recipe.

3.4.3 Transfer

After CNT growth on the quartz chips, the CNTs are mechanically transferred to the prepared device chips. This operation is performed using a Suss Microtec MA6 mask aligner. Figure 3.17 depicts the transfer procedure. The quartz chip is inverted and held flat above the device chip, acting as a "mask" in the MA6 aligner. After optical alignment, the surfaces are slowly moved together until the quartz growth surface contacts the oxide surface of the device chip. During the contacting process, the region of the growth chip that will contact the oxide surface is optically monitored to ensure contact occurs via the observation of thin-film interference. After contact, the samples are separated, and the device chip is optically inspected for evidence of catalyst transfer from the quartz growth surface.

Figure 3.18 shows SEM images of some test structures after the stamping process. Many CNTs are transferred to the device chip, with the majority near the region of the oxide surface surface which is contacted by the growth substrate. Some CNTs are suspended across the contacts as desired. In these images, a few CNTs are shown crossing one contact then collapsing into the middle trench.

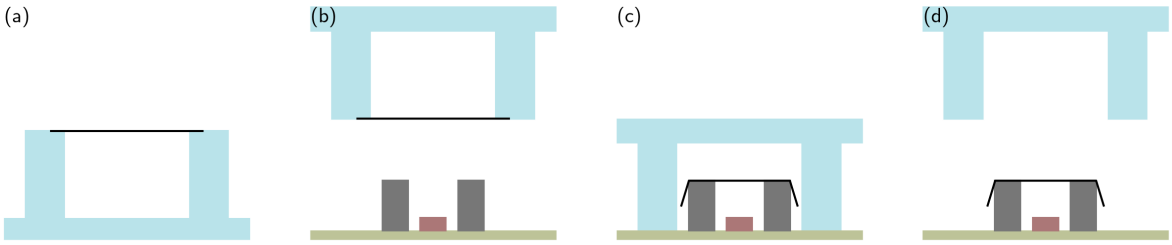

Figure 3.17: Depiction of the CNT stamping process. **a** The CNTs are grown across the raised pillars on the quartz wafer. **b** The quartz chip is inverted and aligned over the prepared device substrate. **c** The two substrates are brought into contact. **d** After removal of the quartz substrate, the CNTs are left suspended across the source/drain contacts.

After initial transfer tests, some devices were observed with significantly worse than expected electrical contact resistance and large (> 2 V) offset of band gap at room temperature. On cooling to 1.4 K, the contacts became opaque and the devices could not be measured. An annealing process was tested that greatly improved the CNT contacts, achieving similar device quality to that achieved for the as-grown suspended devices. Therefore, after the transfer process is completed, all devices are annealed in an Ar:H_2 (98:2) atmosphere for 1 hour at 300°C.

Figure 3.19 shows an optical image and SEM of stamped CNT devices after the complete process.

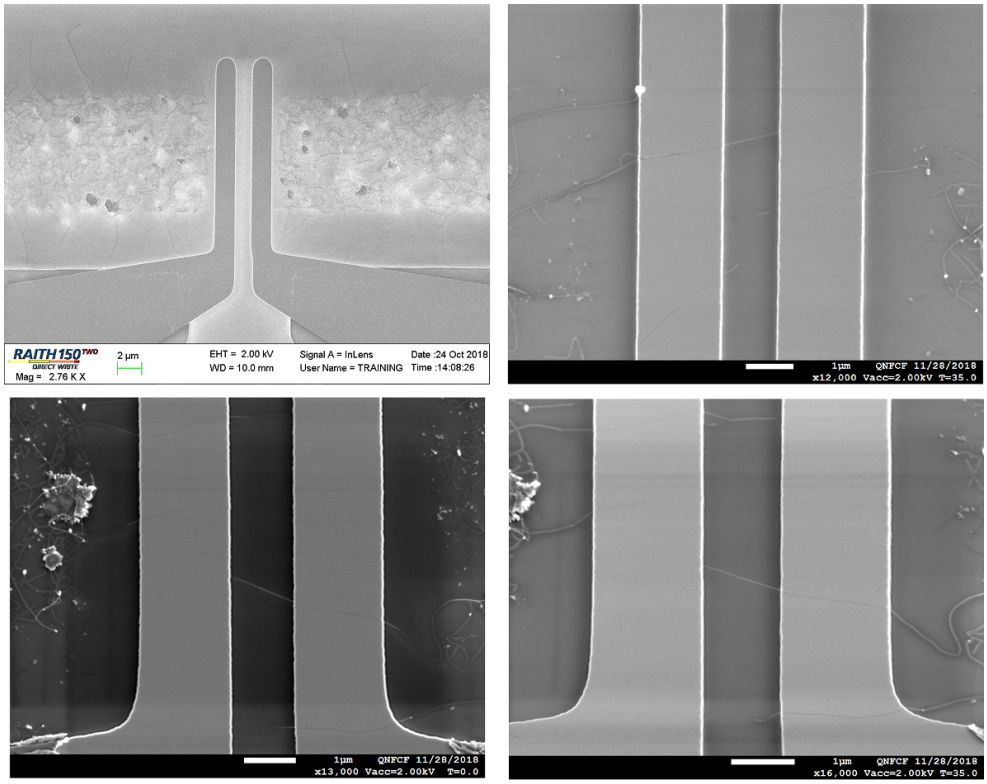

Figure 3.18: SEM imaging of CNTs transferred to test contact samples. Catalyst material transferred from the quartz substrates during the process can be seen on the SiO_2 surface outside the contact region. Some suspended CNTS are seen bridging between the contacts. Additionally, some devices showed shorter CNTs collapsing into the trench (lower panels).

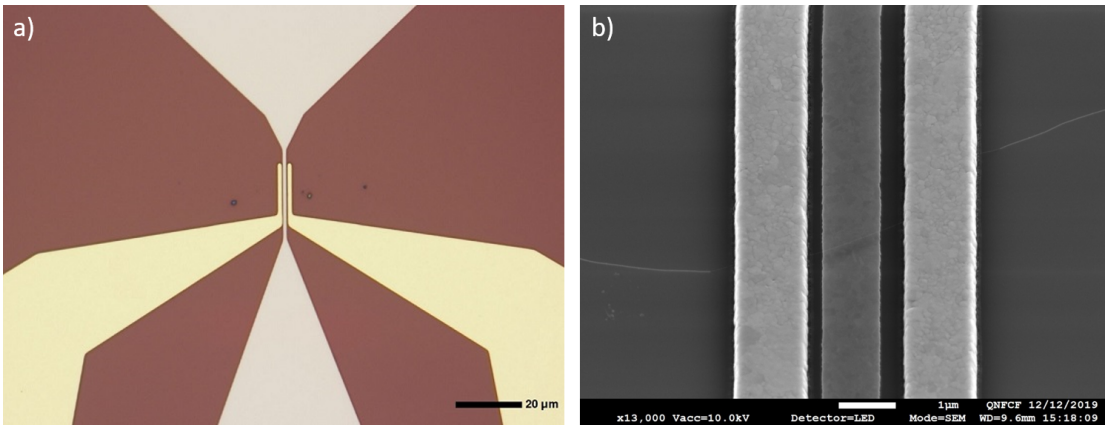

Figure 3.19: **a** Optical image of a stamped CNT device after completed stamping process. The transferred catalyst material can be seen outside of the contacts. **b** SEM image of a completed device showing a CNT suspended across the source/drain contacts (light), over the local back gate (dark).

Chapter 4

Non-linear Transient Response of CNT Mechanical Resonator

While the state-of-the-art sensitivity of CNT nanomechanical resonators has been used to detect record low mass and force signals, it can also be harnessed for fast measurement of larger changes. There is particular value in increasing measurement bandwidth to levels comparable to critical timescales of the system under test. For example, the mechanical frequency shift from molecular nanomagnet spin changes with a suitable field gradient would be on the order of 10 kHz [1]. Single-shot observations of this magnetic switching at time scales comparable to the spin dephasing and relaxation times would be of interest. Molecular nanomagnets of interest in quantum information processing have been found to dephase and relax on timescales of microseconds and milliseconds, respectively, at low temperatures [65, 66]. However, as discussed in section 2.2.2, the contact resistance and measurement circuit stray capacitance typically limit the readout bandwidth. Furthermore, transient response time scale of linear mechanical resonators is given by Q/ω_0, which can limit fast sensing in high-Q suspended CNT devices.

In this chapter I describe an experiment in which a Si-SiGe heterojunction bipolar transistor (HBT) was used as a cryogenic first-stage amplifier to measure a CNT mechanical state on microsecond-timescales. Fast sensing of CNT mechanical resonance had been previously demonstrated using a HEMT voltage amplifier and two-source mixing readout [39, 40]. Here, we show that similar results can be obtained with a non-mixing readout technique using an HBT current amplification circuit. HBTs offer similar operating bandwidth and noise figures to HEMTs, with typically lower intrinsic power dissipation. The non-mixing readout scheme is based on a modified Coulomb rectification technique, and has the advantage that relatively strong measurement probe signals can be used without

affecting the mechanical motion, as the measurement signal frequency is far removed from any mechanical resonance. We use this configuration to study the transient response of the CNT resonator to pulsed driving in both the linear and strongly non-linear regimes, finding that the latter regime can give a faster response in force sensing applications.

4.1 Heterojunction Bipolar Transistors

Heterojunction bipolar transistors are a type of bipolar junction transistor (BJT) that uses heterojunctions between large and small bandgap semiconductor regions to improve the performance compared to traditional BJTs. The differing bandgaps allow for large forward current (due to close conduction bands) while keeping reverse current small (large valence band offsets), resulting in high gain transistors with low base currents. The base region of an HBT can also have gradient doping from large bandgap at the emitter to small bandgap near the collector, which creates an effective electric field within the base and increases the transport speed and therefore bandwidth of the device. Typical integrated circuit HBTs are able to reach ~ 100 GHz bandwidths in normal room temperature operation[67].

In addition to being very high-bandwidth, low-noise amplifiers at room temperature, SiGe HBTs have been demonstrated to work at cryogenic temperatures [68]. Below 30 K the SiGe HBT operates via tunneling between emitter-base-collector regions, and does not experience carrier freeze-out, allowing operation at cryogenic temperatures with little change in operating properties. The HBT also has very little instrinsic heat dissipation (e.g., $0.1-1.0\,\mu$W at $\sim 10^2$ gain) making it compatible with direct integration at any stage of a cryostat. HBT amplification has recently been demonstrated operating on the mixing chamber stage of a dilution refrigerator [69].

4.2 Common Collector HBT Circuit

When used in a common-collector amplifier configuration, an HBT realizes a high-impedance AC current amplifier. Figure 4.1a shows the basic measurement circuit. A DC resistor network is used to switch the HBT into the amplification regime via a supplied voltage, $V_{power} = 1.15$ V. The resistors and capacitors were selected to pass frequencies $\sim$100 kHz while minimizing power dissipation. The estimated power dissipation of this circuit is 120 μW, which is dominated by the DC current through the 2 kΩ emitter resistor. Note that direct HBT amplification (no resistor network) could be used as in reference [68], to allow MHz frequency operation with μW power dissipation, at the cost of highly

non-linear biasing of the CNT device. All measurements were carried out in a pumped ^{4}He cryostat with the sample in vacuum at a temperature of 1.4 K, using the custom cryostat probe describe in appendix C and the HBT circuit board shown in figure 4.1b and c.

To realize fast measurements, the electrical ringdown time of the measurement circuit should be short compared to the mechanical response timescale. Figure 4.2 shows the averaged electrical current, I_{out}, of the HBT circuit when switching off an AC bias voltage V_{bias} with no mechanical driving (i.e. $V_{g,ac} = 0$). The applied V_{bias} is a 100 kHz sine wave with 1 mV amplitude, which is switched off at $t = 0$. There is a 5 μs delay between the applied pulse (both switching on or off) and the response observed through the measurement setup. The electrical ringdown has a time constant $\tau \lesssim 10$ μs.

4.3 Suspended CNT Device

The CNT device measured in this chapter was fabricated using the as-grown suspended CNT process from 3.3. It was characterized in a prior cool-down at 1.4 K using a frequency-modulation technique as describe in section 2.2.2, without the HBT circuit present. Figure 4.3 shows the mixing current measured with strong driving ($V_{g,ac} = 500$ μV), as a function of the DC component of the gate voltage $V_{g,dc}$, where two primary modes were observed. The lower frequency mode is only weakly coupled to the gate, and is not observed at lower driving power. It is expected that this mode is in-plane with the gate, while the higher frequency mode is out-of-plane. The mode separation at low V_g can be a result of built in tension anisotropy due to contacts[15]. In this chapter we focus on the strongly gate-coupled out-of-plane mode.

4.4 Transient Response Measurements

The CNT mechanical motion is detected with a modified Coulomb rectification readout scheme [13]. The mechanical driving signal, $V_{g,ac}$, is applied to the gate along with a DC gate voltage to electrically tune the device, $V_{g,dc}$. An AC voltage is applied to bias the device, as in figure 4.2. When the bias frequency is much lower than the mechanical driving, the observed current at the bias frequency will be time-averaged over the mechanical oscillations, so that

$$I \approx I' + \left(\frac{x_0}{2}\frac{dC_g}{dx}\frac{V_{g,dc}}{C_g}\right)^2 \frac{\partial^2 I'}{\partial V_g^2} \tag{4.1}$$

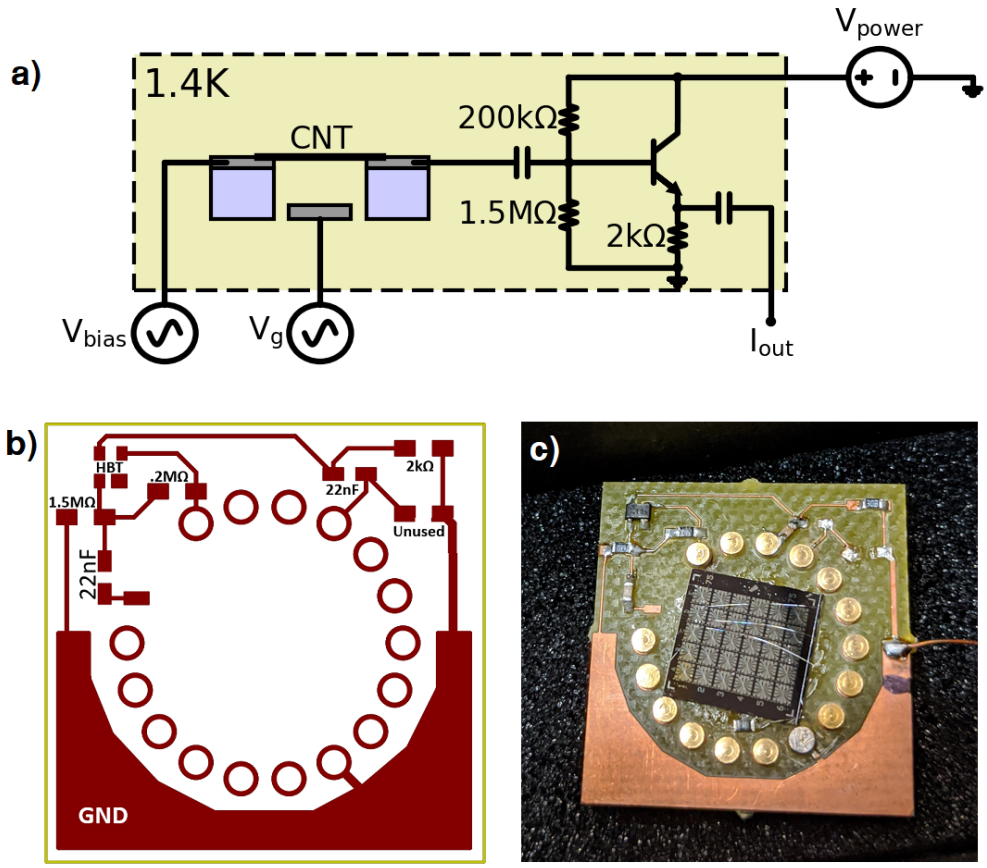

Figure 4.1: **a**. The measurement circuit used for fast readout of CNT mechanical motion. The CNT resonator is connected to a nearby common-collector HBT amplifier circuit, all at a temperature of 1.4 K. The capacitors are both 22 nF, and the HBT is an Infineon BFP842ESD powered with a DC voltage $V_{power} = 1.15$V. **b**. An annotated schematic of the PCB design for the HBT circuit shown in **a**. The inner ring of circles is populated with 0.5 mm Mill-Max Manufacturing pin terminal connectors, which plug into matching sockets in the cryostat probe. The upper surface of these pins are used as bonding pads for wire-bond connections to the device chip. **c**. A photograph of an as-grown suspended CNT device chip mounted and wire-bonded to an HBT measurement board.

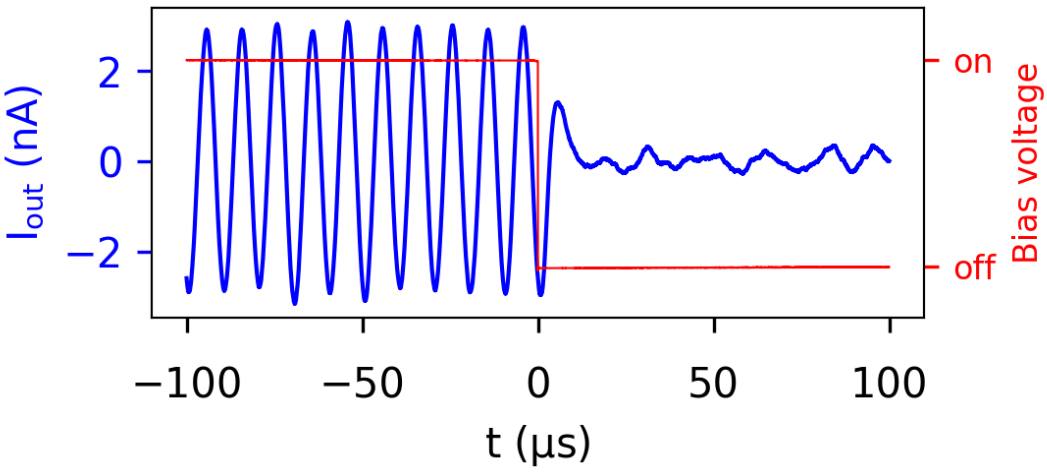

Figure 4.2: Current response measured at I_{out} when a 100 kHz, 1 mV signal on V_{bias} is switched off (at $t = 0$). The electrical response shows a 5μs delay and a $\lesssim$ 10μs ringdown, which is shorter than the typical timescale of CNT mechanical response. The current fluctuations observed for $t > 0$ indicate the noise floor of the measurement setup, approximately 0.15 nA.

where I is the measured current, I' is the current in absence of mechanical driving, C_g is the gate-CNT capacitance, x is the distance between the CNT and gate, and x_0 is the amplitude of motion of the CNT. The dependence of I on $\partial^2 I'/\partial V_g^2$ constrains this readout to measurements at non-linear conductance features such as Coulomb peaks. The Coulomb rectification readout method requires no component of the measurement signal (bias) to be near the resonance frequency, as is required for mixing techniques. This allows for large measurement voltages without inducing mechanical driving. This is especially advantageous when measuring strongly nonlinear resonators, where large drive powers near the resonance frequency result in broad resonant linewidths.

The results shown in figures 4.4 and 4.5 use the rectification scheme, with a 1 mV, 100 kHz AC bias voltage. For the measurements in figure 4.4a and b, I_{out} from the HBT circuit is measured through a current-voltage preamplifier and input to a lock-in amplifier. For time-domain measurements, I_{out} is amplified and recorded on an oscilloscope. The time-domain data is post-processed to extract the root mean square envelope function (see appendix D for details of this envelope extraction).

Figure 4.4a and b shows the mechanical resonance measured across a Coulomb peak (bright vertical region), with driving voltages of $V_{g,ac} = 50$ μV and 200 μV, respectively.

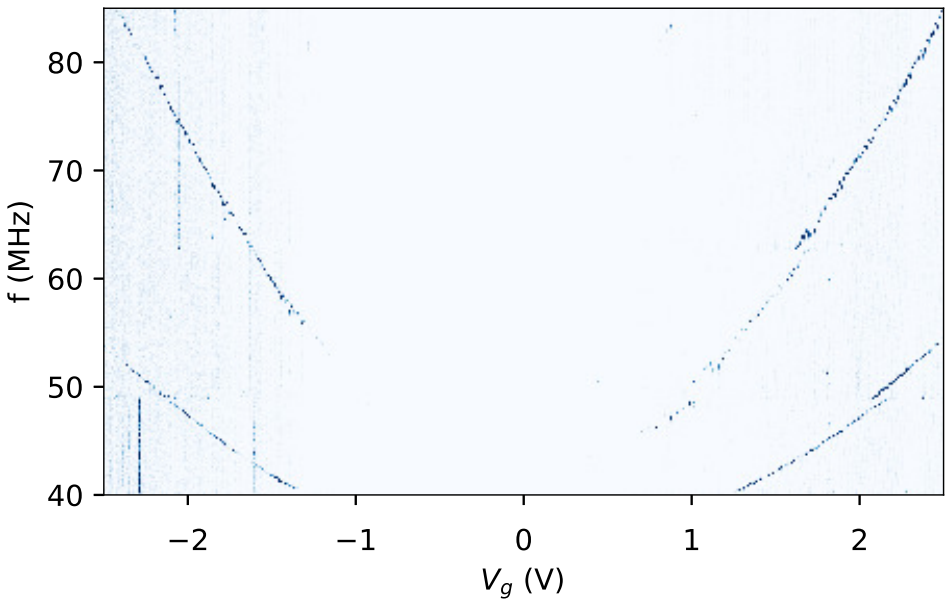

Figure 4.3: Mixing current (arbitrary units) observed for the CNT resonator in a previous measurement without the HBT circuit, using frequency-modulated mixing and an AC driving voltage of 500μV. The lower frequency mode is more weakly coupled to the gate, and is likely an in-plane mode. The higher frequency mode, which we focus on in this paper, is strongly coupled to the gate and is likely out-of-plane.

For low driving power, on the conductance peak we observe a small decrease in both the mechanical frequency and Q factor, as seen in similar devices and described by the coupling of single electron tunneling to mechanical modes [17, 18, 14]. The stronger driving power in figure 4.4b causes nonlinear effects to become visible, and a switch from spring softening to spring hardening nonlinearities is seen, as was observed in reference [14].

Figure 4.4c and d show time-domain measurements of mechanical motion in which transient decays are observed upon switching the drive on or off. Both measurements were performed at the maximum of the conductance peak shown in (a,b), and at the drive frequency 89.7 MHz, which is the mechanical resonance frequency in the linear (low drive power) regime. $V_{g,ac}$ is switched on/off at 1 kHz with 50% duty cycle. In figure 4.4c, $V_{g,ac} = 50\ \mu$V and the resonator shows transient mechanical ringdown expected for a linear harmonic oscillator driven on resonance. The signal decay time constant gives $Q \approx 2 \times 10^4$. At the higher drive power $V_{g,ac} = 200\ \mu$V in figure 4.4d, a similar transient response is seen for turn-off of the drive, but the turn-on has a more rapid response due to resonator non-linearity. Note that the 16 kHz oscillatory baseline seen in this measurement is due to residual external noise of the measurement system, and is not an intrinsic response of the device.

To fit this behaviour, the oscillator was modelled using a Duffing non-linearity and non-linear damping in the harmonic oscillator equation from section 2.3.1

$$m\frac{d^2x}{dt^2} + (k + \alpha x^2)x + (\gamma + \eta x^2)\frac{dx}{dt} = F_{drive}\cos(\omega t) \tag{4.2}$$

where m is the effective mass of the CNT mode, $k = m\omega_0^2$ is the linear spring constant, γ is the linear damping coefficient, α is the Duffing parameter, η is the non-linear damping coefficient, and $F_{drive} = (\partial C_g/\partial x)V_{g,dc}V_{g,ac}$ is the electrostatic driving force. The parameters in equation 4.2 are initially estimated from the device geometry and expected CNT diameter, then adjusted to fit the transient response (see appendix D for fitting example). The time evolution is solved numerically, and converted to a current using off-resonance transport data and equation 4.1. Importantly, the fits in figure 4.4c and d use the same set of parameters, with only the value of $V_{g,ac}$ being different.

Measurements at a second Coulomb peak revealed further non-linearity in the transient response. Figure 4.5b shows transient current measured at the edge of a conductance peak at $V_{g,dc} = -3.03\ V$ shown in figure 4.5a, using low drive power $V_{g,ac} = 50\ \mu$V. Sitting at the edge of the Coulomb peak maintains a large $\partial^2 I'/\partial V_g^2$ for the rectification signal, but changes the non-linear parameters, in particular changing the sign of α. Additionally, this Coulomb peak had a higher conductance than that measured in figure 4.4, which is expected

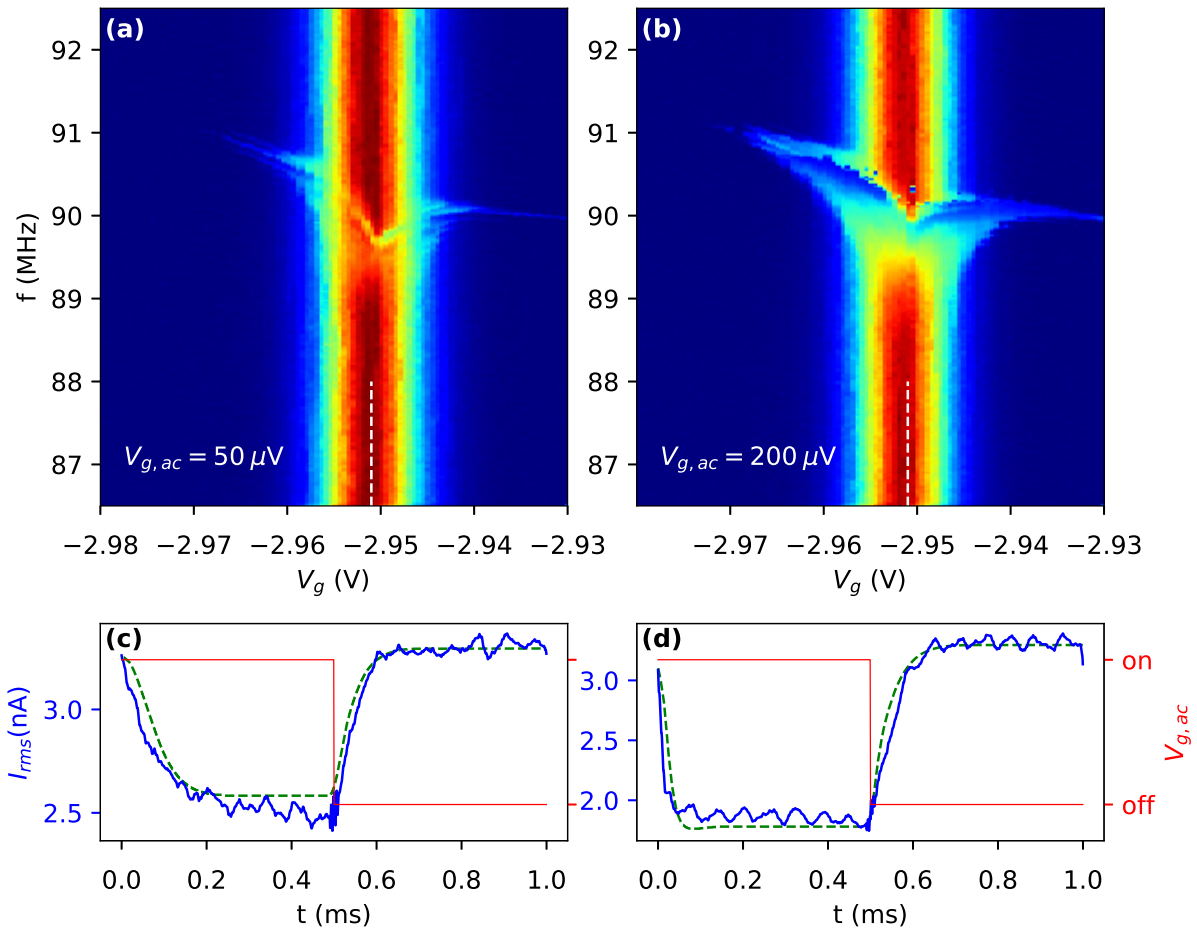

Figure 4.4: **a,b** Current through the CNT mechanical resonator versus DC gate voltage (horizontal axis) and mechanical drive frequency (vertical axis). The color scale represents I_{out} from 0 (dark blue) to 3.5 nA (red). The current is measured via lock-in amplifier with an applied bias voltage of 1 mV at 100 kHz. The mechanical drive is an AC gate voltage of 50 μV and 200 μV, respectively. Nonlinear behaviour is clearly observed at the higher driving power. White dashed line indicates V_g used in c,d. **c** Transient current response due to pulsed driving, related to the CNT mechanical amplitude by equation 4.1. This data was measured on the Coulomb peak in (a) and with 50 μV drive voltage. The red line shows when $V_{g,ac}$ is applied, the blue line shows the measured current envelope, and the green dashed line shows a fit using equation 4.2 with $\alpha = 5 \times 10^9$ kg m^{-2} s^{-2}, $\gamma = 10^{-17}$ kg s^{-1}, $\eta = 22$ kg m^{-2} s^{-1}. **d** Transient response under the same conditions except that $V_{g,ac} = 200$ μV. The green line fit uses the same α, γ, η values as (c).

to give a stronger non-linearity. In this case, the transient signal shows an overshoot [70] of the steady state amplitude during turn-on, which is also captured by equation 4.2. In this regime, the non-linear amplitude response pulls the effective resonance frequency away from the drive frequency, creating a damped beating similar to a linear oscillator with off-resonant driving.

4.5 Discussion

The non-linear damping measured in the above time-domain measurements can be utilized to realize fast response in sensing applications. In the linear regime, the response speed of the mechanical amplitude to any changes in mass/force will be limited by the time constant $\tau = Q/\omega_0$. By operating in a regime of stronger non-linear damping, the response time can be reduced. Figure 4.6 shows simulation results to demonstrate this, using device parameters from figure 4.4. The spring constant, k, is instantaneously shifted at $t = 0$ by a Δk so that resonance frequency, $\omega_0 = \sqrt{k/m}$, is decreased by $\Delta\omega_0 = 2\pi \times 10$ kHz.

This simulates a shift of the mechanical resonance frequency induced by a change in the CNT tension. This could be generated, for example, by the spin flip of a molecular nanomagnet in a magnetic field gradient [1]. In both panels, for $t < 0$, the device is driven at a frequency slightly below the mechanical resonance, so that the amplitude of motion is below the maximum value. The change in resonance frequency at $t = 0$ brings the CNT closer to resonance and increases the amplitude of motion, in this case by $\Delta x_0 \approx 0.3$ nm. This change in amplitude would shift the measured current by ~ 0.2 nA for a similar conductance peak as the one shown in figure 4.4. The top panel of figure 4.6 shows the response for a weak drive in which the device is dominated by linear terms, and the lower panel shows the case for a stronger drive in which the non-linear terms dominate. The weakly driven linear response time constant is 72 μs, whereas under strong driving it is 16 μs, about 5 times faster.

4.6 Conclusion

In this chapter I demonstrated fast electrical readout of the mechanical state of a suspended CNT resonator, enabled by a cryogenic HBT circuit. Using a Coulomb rectification readout, the mechanical oscillation amplitude could be determined at $\sim 10\,\mu$s time scales. The transient mechanical response was measured using pulsed driving of the CNT resonance. With the Coulomb rectification readout, strong driving could be used to demonstrate the

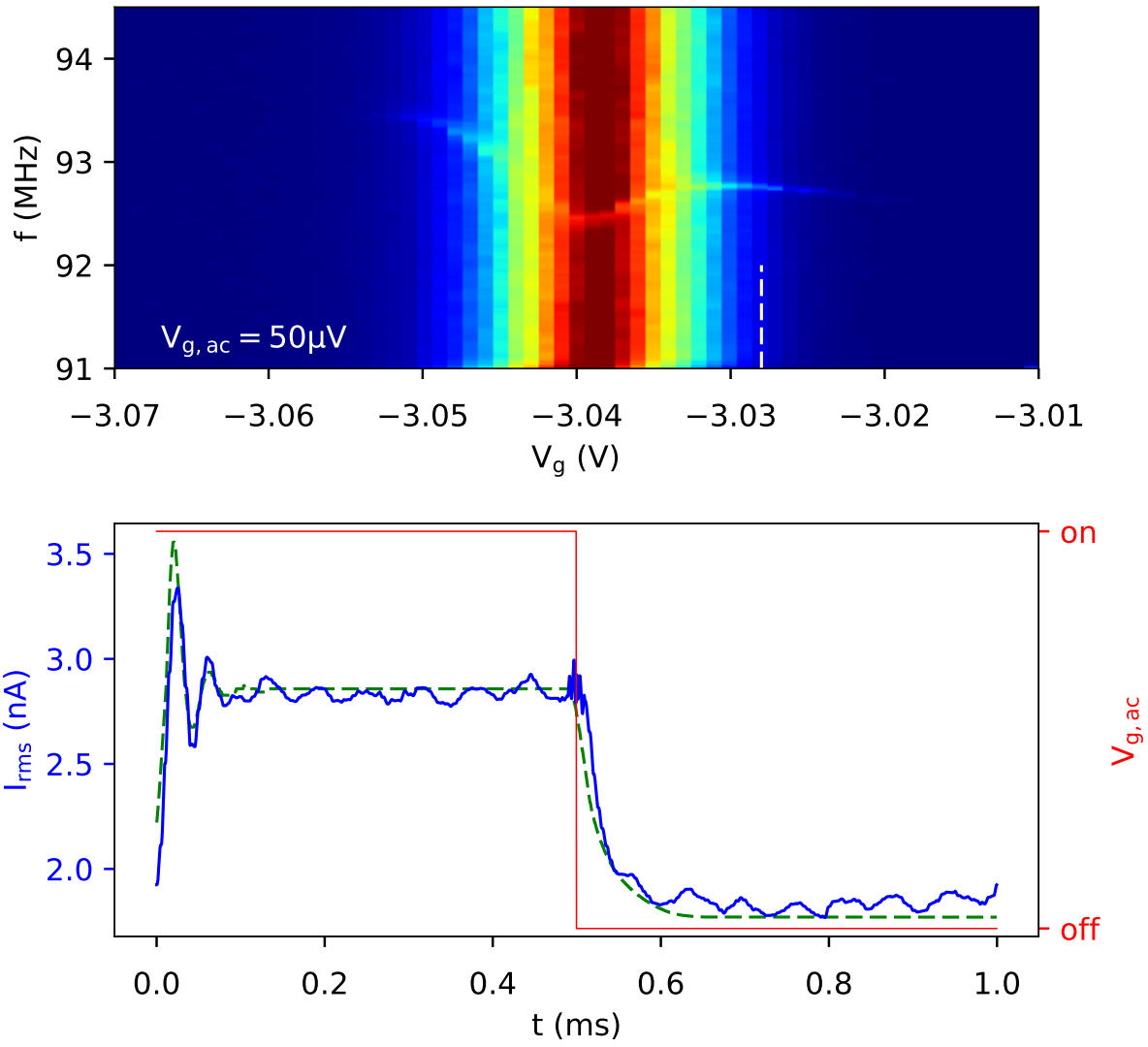

Figure 4.5: Transient current response showing mechanical overshoot at the turn-on of a 50 μV drive voltage. The red line shows when $V_{g,ac}$ is applied, the blue line shows the measured current envelope, and the green dashed line shows a fit using equation 4.2 with $\alpha = -6 \times 10^{10}$ kg m^{-2} s^{-2}, $\gamma = 3 \times 10^{-17}$ kg s^{-1}, and $\eta = 100$ kg m^{-2} s^{-1}.

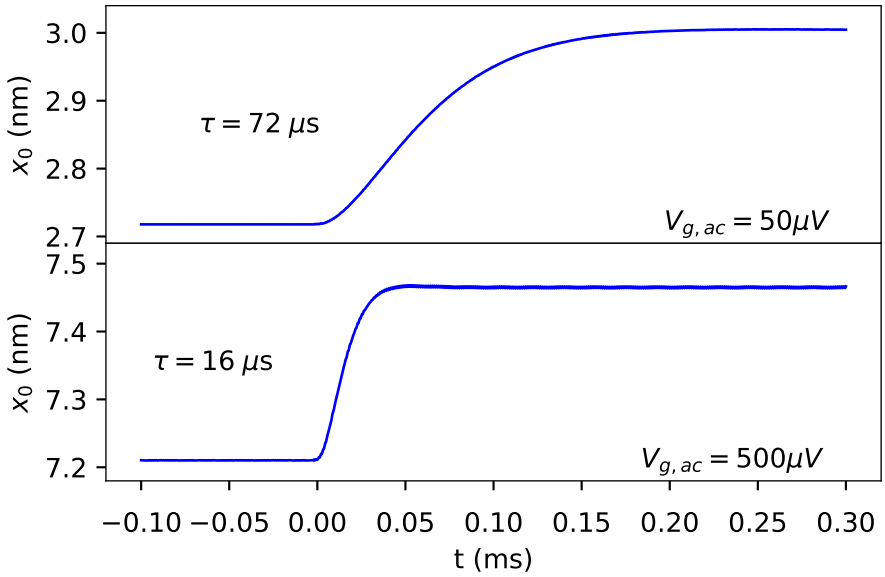

Figure 4.6: Simulated transient response to a resonance frequency shift of 10 kHz at $t = 0$. The resonator is modelled with $\alpha = 5 \times 10^9$ kg m^{-2} s^{-2}, $\gamma = 10^{-17}$ kg s^{-1}, and $\eta = 22$ kg m^{-2}s^{-1}. At low drive power, $V_{g,ac} = 50\ \mu$V, the time constant is 72 μs. At higher drive power, $V_{g,ac} = 500\ \mu$V, the resonator non-linearity yields a more rapid response time of 16 μs.

nonlinear response of this transient behaviour, which was well described by Duffing and non-linear damping terms in equation 4.2. For the CNT device measured in this chapter, a mechanical response time around 10 μs could be obtained by using strong driving. Future work could investigate the use of direct HBT amplification [68] with no resistor network, which should allow up to $\sim$ 100 MHz bandwidths at μW dissipation levels, enabling sub-microsecond force sensing in a dilution refrigerator. This would permit single-shot readout of the magnetic states of molecular nanomagnets on timescales comparable to their spin relaxation and dephasing times.

Chapter 5

Self-driven oscillation of Suspended Carbon Nanotubes in Coulomb Blockade

Self-oscillation features in suspended carbon nanotubes were first observed as instabilities in the transport of early high-Q suspended CNT devices [14]. Further study of similar features confirmed the mechanical nature and high-Q requirements for observation of these self-driven signatures [71, 72]. Recent experiments have observed self-driven oscillations in Kondo regime [73] and high-bias tunnel transport [74], and through improved readout techniques have verified the large amplitude and bistability of the self driven states. Unlike previous self-driven oscillations, the self-driving reported in this chapter manifests as current within nominally zero-current Coulomb blockade of the CNT transport.

5.1 Device description

The suspended CNT devices measured in this chapter were fabricated with the stamping process described in section 3.4. Figure 5.1a show a schematic of the device and figure 5.1b shows an SEM image of a device similar to those measured in this chapter. The 30 mK and 800 mK measurements presented in this chapter were taken in an Oxford Instruments DR200 dilution refrigerator using the custom wiring described in appendix E. The same device was measured at 1.4 K in a pumped He_4 cryostat using the probe described in appendix C.

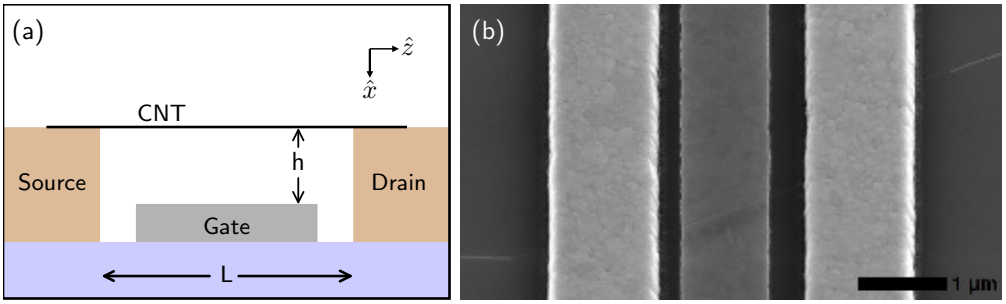

Figure 5.1: **a** Schematic of suspended CNT device measured in this chapter. The CNT is suspended across Ti/Au source and drain contacts, and over a nickel gate. The CNT-gate separation is approximately 340 nm with a nominal suspended length of 2 μm. **b**. SEM image of a suspended CNT device similar to that measured in this chapter.

As a first measure of the CNT behaviour, figure 5.2 shows the current as a function of gate voltage at $V_{sd} = 1$ mV. The bandgap region of suppressed conduction around $V_g = 0.4$ V and high conductance at $V_g < 0$ suggests hole biased metal-CNT interfaces and a bandgap of $E_{gap} \approx 80$ meV. For $V_g > 0.5$ V, the conductance is governed by Coulomb blockade, with some modulation of conductance likely due to surface disorder [75].

Towards estimating the device dimensions, figure 5.3 shows three Coulomb peak positions as a function of applied axial magnetic field, $B_{\|}$. Energy crossings between different orbitals create a switching pattern of peak shifts with $B_{\|}$ [76]. The slope of the peak position between the transitions, $\frac{dV_{g,peak}}{dB}$, provides a measure of the orbital magnetic moment in the CNT, $\mu_{orb} = \alpha \frac{dV_{g,peak}}{dB}$ where $\alpha = 0.45$ is the lever arm of the gate on the dot chemical potential. From figure 5.3, an orbital magnetic moment of $\mu_{orb} = 0.4$meV/T is determined. This corresponds to a CNT diameter of approximately 2 nm [77].

Figure 5.4 shows the mechanical resonance frequency as a function of gate voltage for this device at 30 mK. The resonance frequency was measured using the Coulomb rectification technique, operated within the Coulomb blockade regime to minimize SET induced frequency shifts. Figure 5.4 also includes a fitting to the resonance curve using solutions to the Euler-Bernoulli beam model described in section 2.3.2. The model fit provides a further estimate of the CNT diameter (1.9 nm), suspended length (2.2 μm), and residual compression ($T_0 = 35$ pN). The figure inset shows one of conduction peaks used to find the resonant frequency, the linewidth of which provides a lower bound of the mechanical quality factor, $Q > 10^4$.

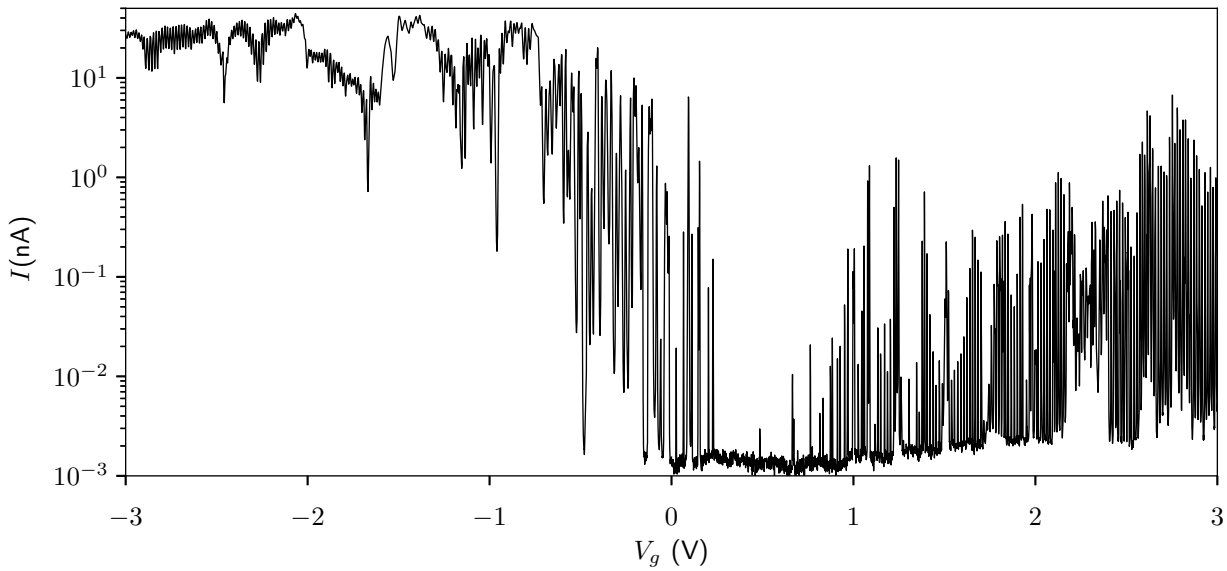

Figure 5.2: Current as a function of applied gate voltage for the primary device measured in this chapter. Large currents for $V_g < 0$ and Coulomb-blockaded conductance for $V_g > 0.5\,\mathrm{V}$ are indicative of p-biased contacts to a single CNT.

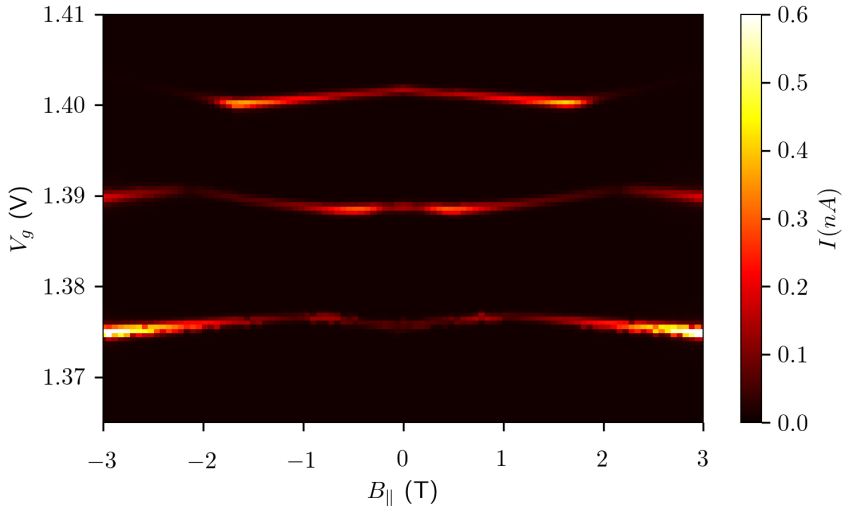

Figure 5.3: Coulomb peak position as a function of applied axial magnetic field. The magnetic field shifts the orbital energies, causing crossing between orbitals. From the straight sections, an orbital magnetic moment of 40 meV/T is determined.

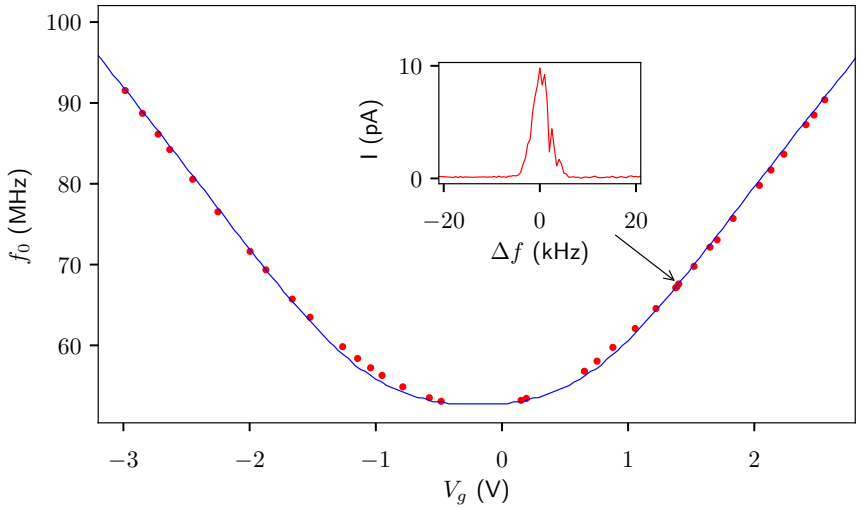

Figure 5.4: Measured mechanical resonance frequency as a function of applied DC gate voltage. The red markers indicate experimental values, while the blue line is a fit using an Euler-Bernoulli beam model. The model fit uses a CNT diameter of 1.9 nm, suspended length of 2.2 μm, and residual compression of $T_0 = 35$ pN. The inset shows one of the conductance peaks used to measure the resonance frequency. The linewidth of this peak gives a lower bound on the mechanical quality factor, $Q > 10^4$.

The low conduction of electron transport as seen in figure 5.2 prohibits electron occupation counting and observation of effects such as four-fold shell filling. However, the hole transport regime in the same device did exhibit some of these expected CNT conduction features. Figure 5.5a shows the differential conductance measured for a region of hole conduction ($V_g < 0$), which demonstrates the four-fold shell filling. Figure 5.5b shows a focus on one region of that data which demonstrates Kondo-mediated transport, in which states with odd carrier occupation have enhanced zero bias conduction below the critical Kondo temperature. Figure 5.5c shows the same measurement taken at temperature $T = 800\,\mathrm{mK}$, where the Kondo enhanced transport has been suppressed.

5.2 Observation of self-driven oscillation

The self-driven oscillation features became apparent when performing DC conductance measurements at 30 mK. Figure 5.6a shows such a differential conductance measurement when operating in the Coulomb blockade regime of the suspended CNT. Overlaid on the expected Coulomb diamond structure, there are several finite conduction features that occur within the nominally fixed-occupation region (in-diamond). Note that these features do not depend on measurement sweep direction, and are stable in time. Figure 4.4b shows a similar DC conductance measurement performed on the same device at 1.4 K, for which the expected Coulomb diamond pattern is observed. In figure 4.4b there are several sharp bright features in the high bias tunneling region, similar to self-driven oscillations reported in literature [74]. From the Coulomb diamond edges, the device capacitance and approximate resonant tunnel rates are determined: $C_g = 12.3\,\mathrm{aF}$, $C_s = 5.6\,\mathrm{aF}$, $C_d = 8.4\,\mathrm{aF}$, $\Gamma_s = 3\,\mathrm{GHz}$, $\Gamma_d = 8\,\mathrm{GHz}$.

The in-diamond features observed in figure 5.6a share the sharp, rough edges of the high-bias self-driven features of figure 5.6b. The stretching of these features into the Coulomb diamond regions in figure 5.6a is reminiscent of the widening of the Coulomb peak width under strong resonant mechanical driving, as used in the Coulomb rectification readout. The self-driven features are typically asymmetric with respect to the gate voltage and indicate a large amplitude of motion. For example, using the device parameters determined above to estimate C_g and $\partial C_g/\partial x$, the finite current observed near $V_g = 1.82\mathrm{V}, V_{sd} = -1\mathrm{mV}$ corresponds to an approximate oscillation amplitude of 5 nm.

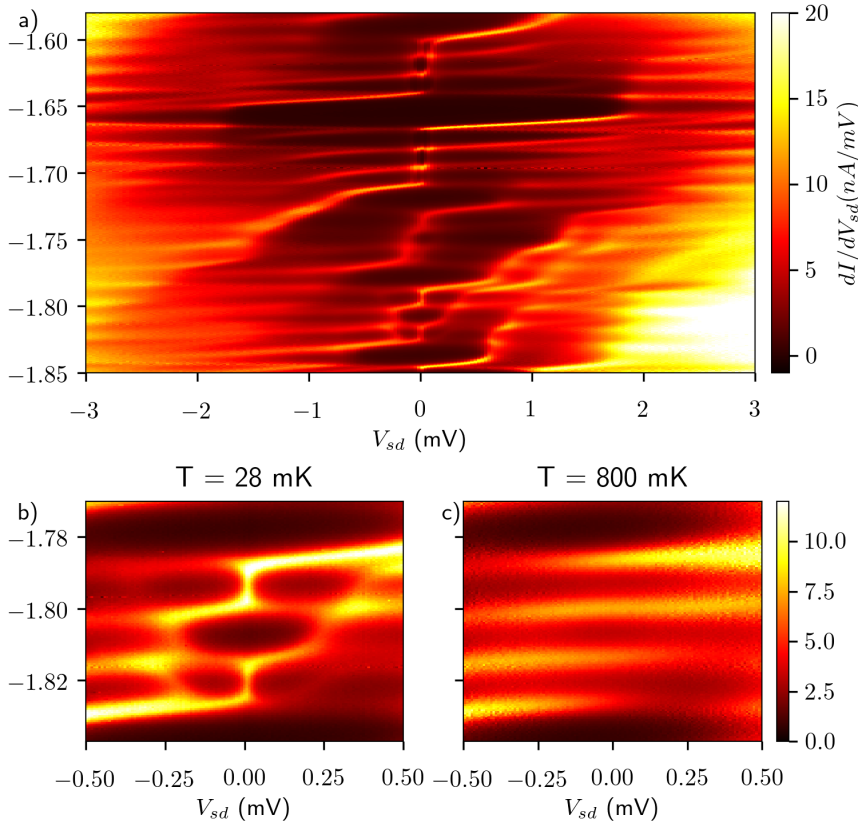

Figure 5.5: Differential conductance measurements showing Kondo transport features and four-fold shell filling in hole-transport of the CNT device. **a** A wide area measurement showing four-fold shell filling over many occupations. **b** Focused measurement showing one set of four-shell filling, in which Kondo-enhanced transport at zero bias occurs for odd carrier occupation. **c** At $T = 800$ mK, the transport is above the Kondo critical temperature, and the enhanced zero-bias transport is suppressed.

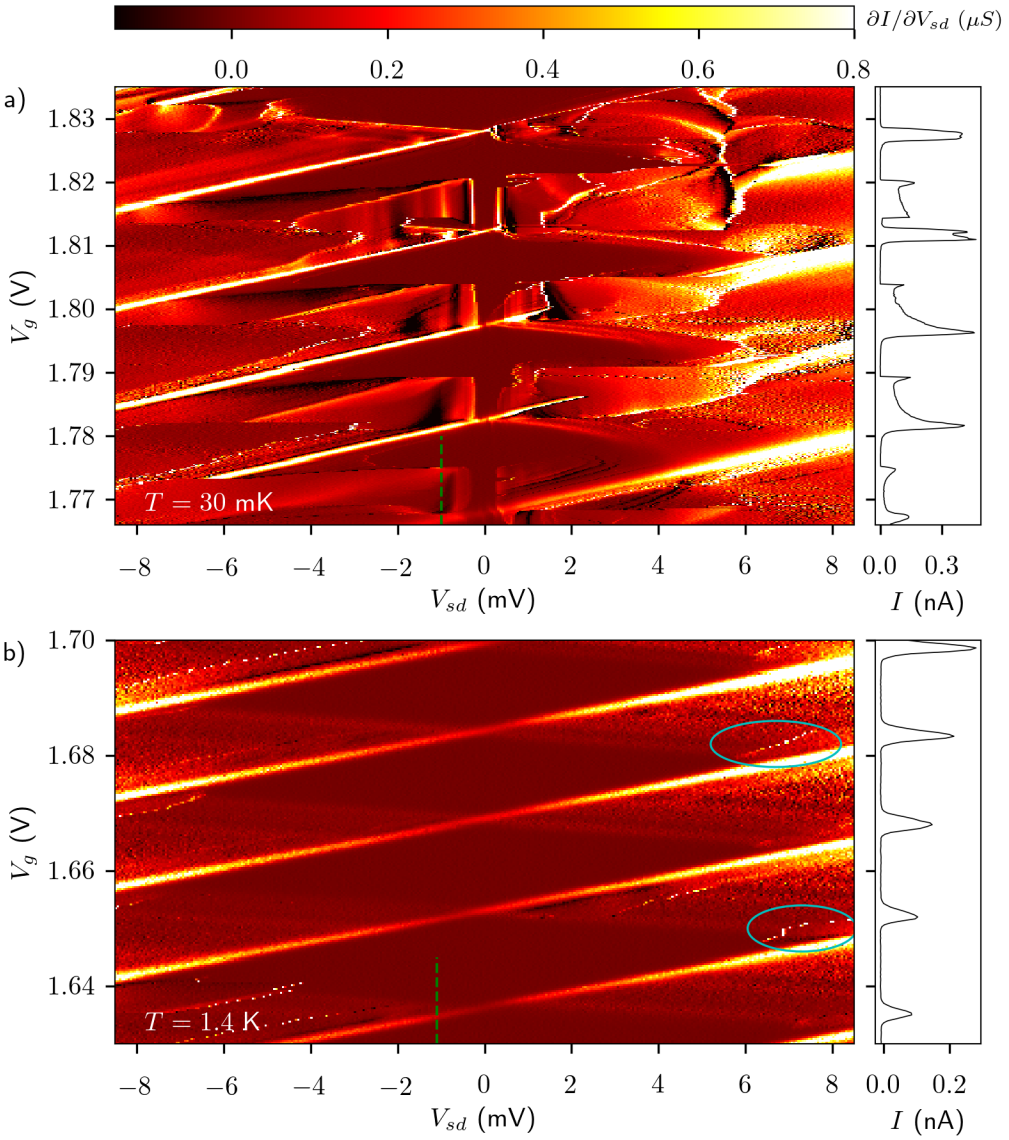

Figure 5.6: **a**. Differential conductance, $\frac{\partial I}{\partial V_s d}$, as a function of DC gate voltage and bias for a suspended CNT device at $T = 30$ mK. Large areas of conductance are observed within the nominally zero-conductance Coulomb diamond. The right side plot shows the current, I, measured at $V_{sd} = -1$ mV bias, in which these conductance features appear as large side lobes on the expected Coulomb peaks. **b** Differential conductance and current measurement of the same device taken at $T = 1.4$ K, in which the expected Coulomb diamonds and Coulomb peaks are observed. Sharp switching ridges are seen at high bias (see two examples highlighted in blue circles), indicative of self-driven oscillations.

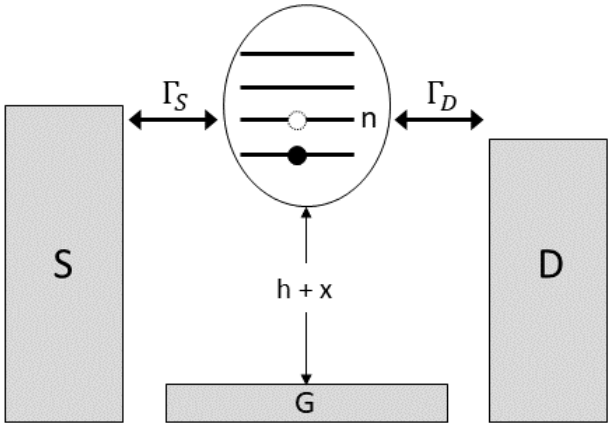

Figure 5.7: Model system for the nanomechanical quantum dot model discussed in text. A quantum dot is tunnel coupled to source(S) and drain(D) leads, and capacitively coupled to a gate(G). The dot is free to move relative to the gate position, changing gate capacitance. The displacement, x, from the equilibrium gate-dot separation h is considered as a harmonic oscillator.

5.3 Nanomechanical quantum dot model

To describe the mechanical oscillation-quantum dot system, I consider an extension of the model developed in reference [78]. The extension presented here reduces the weak coupling requirement and considers the region between two electron occupation transitions ($n \to n+1$ and $n \to n-1$). The model system is shown in figure 5.7. A quantum dot is suspended above a fixed gate (G) and tunnel-coupled to two leads (S and D). The dot position relative to the gate is free to change, with x being the displacement from initial separation h.

5.3.1 Electromechanical coupling parameter

The electrostatic force between the gate and the quantum dot is given by [79]

$$F_{dot} = \frac{1}{2}\frac{\partial C_g}{\partial x}(V_g - V_{dot})^2 \tag{5.1}$$

where

$$V_{dot} = \frac{1}{C_{tot}}\left(C_g V_g + C_s V_s + C_d V_d - e\langle N\rangle\right) \tag{5.2}$$

with $\langle N \rangle$ the average electron occupation of the dot. For the voltages considered in this chapter $\langle N \rangle \approx \frac{C_g V_g}{e}$ so that $V_{dot} \ll V_g$ and

$$F_{dot} \approx \frac{1}{2}\frac{\partial C_g}{\partial x}V_g^2 - \frac{\partial C_g}{\partial x}\frac{V_g}{C_{tot}}\left(C_g V_g + C_s V_s + C_d V_d\right) + \frac{e}{C_{tot}}\frac{\partial C_g}{\partial x}V_g\langle N \rangle \tag{5.3}$$

Meanwhile, the electronic occupation of the dot depends on the chemical potential alignment of the leads and the dot, as described in section 2.1.1. The potential of the dot is given by the energy

$$\mu_{dot} = \frac{e}{C_{tot}}\left(C_g V_g + C_s V_s + C_d V_d\right) \tag{5.4}$$

which depends on the dot's mechanical position via the position dependence of C_g.

For the CNT system considered in this chapter, the amplitude of motion will be much smaller than the CNT-gate separation ($x \ll h$), and the capacitance can be approximated by the first order Taylor expansion

$$C_g(x) \approx C_g(0)\left(1 + x\frac{\partial C_g}{\partial x}\right) \tag{5.5}$$

The chemical potential of the dot can then be expressed as a function of position

$$\mu_{dot}(x) = \frac{e}{C_{tot}}\left(C_g(0) V_g + C_s V_s + C_d V_d\right) + \frac{e}{C_g}\frac{\partial C_{tot}}{\partial x}V_g x \tag{5.6}$$

Therefore the coupling between the chemical potential of the dot and its position is characterized by the parameter

$$F = \frac{e}{C_{tot}}\frac{\partial C_g}{\partial x}V_g \tag{5.7}$$

The chemical potential of the quantum dot can be written

$$\mu_{dot} = \mu_0 + Fx \tag{5.8}$$

where μ_0 is the dot potential given by equation (5.4) with C_g evaluated at $x = 0$.

5.3.2 Energy scales

To simplify the following analysis, consider the relevant energy scales of the system. For the CNT device measured in this chapter, approximate energy scales of all of the relevant processes are given in table 5.1.

Process	Symbol	Approx. values	Energy scale (Hz)
Electron tunneling	$\Gamma^{+,-}_{L,R}$	7 GHz	$7 \cdot 10^9$
Applied voltages	$V_{s,d,g}$	1 mV	$1.5 \cdot 10^{12}$
Charging energy	E_c	7 meV	$1 \cdot 10^{13}$
Mechanical oscillation	ω_0	70 MHz	$7 \cdot 10^7$
Mechanical relaxation	ω_0/Q	700 Hz	$7 \cdot 10^2$
Temperature	T	100 mK	$1.3 \cdot 10^{10}$

Table 5.1: Energy scales for the CNT device described in this chapter.

The mechanical motion is in the classical regime ($\hbar\omega_0 \ll k_b T$), so it is well described by a classical position and velocity (x, v).

The tunnel rates are much faster than the mechanical motion ($\Gamma \gg \omega_0$) so that individual tunneling events occur at approximately fixed positions, with only small changes in position between successive tunneling events. This permits the approximation $\Gamma(x, v) \approx \Gamma(x)$.

Finally, the mechanical resonance is only weakly damped ($Q \gg 1$) so that the mechanical state changes little between successive oscillations.

5.3.3 Amplitude of oscillation

For classical tunneling and mechanical oscillations, the state of the system can be described by joint probability distributions, $P_n(x, v, t)$, where P_n is the probability distribution for the variables (x, v, t) at electron occupation n. Consider the initial state for which at $x = 0$, the average occupation is fixed, $\langle N \rangle = n$. Then the probability distributions obeys the coupled equations [80, 81, 78]

$$\mathscr{L} P_{n-1} - \frac{F}{M}\frac{\partial P_{n-1}}{\partial v} = -\Gamma_{n-1\to n} P_{n-1} + \Gamma_{n\to n-1} P_n \tag{5.9}$$

$$\mathscr{L} P_n = \Gamma_{n-1\to n} P_{n-1} - \left(\Gamma_{n\to n-1} + \Gamma_{n\to n+1}\right) P_n + \Gamma_{n+1\to n} P_{n+1} \tag{5.10}$$

$$\mathscr{L} P_{n+1} + \frac{F}{M}\frac{\partial P_{n+1}}{\partial v} = \Gamma_{n\to n+1} P_n - \Gamma_{n+1\to n} P_{n+1} \tag{5.11}$$

where $\Gamma_{a\to b} = \Gamma^s_{a\to b} + \Gamma^d_{a\to b}$ is the combined tunnel rate from state a to state b through both leads, and $\mathscr{L}$ describes the mean-coordinate evolution of an oscillator with frequency ω_0 and quality factor Q [80]

$$\mathscr{L} P_* = \frac{\partial P_*}{\partial t} + v\frac{\partial P_*}{\partial x} - \omega_0^2 x\frac{\partial P_*}{\partial v} - \frac{\omega_0}{Q}\frac{\partial v P_*}{\partial v}$$

Under the assumptions $\Gamma \gg \omega_0$ and $eV_{s,d} < E_c$, the tunneling events will occur much faster than the time scale of mechanical motion, so that one of P_{n-1} or P_{n+1} will be zero when evaluating the above expression for any (x, v, t).

I am interested in steady state solutions of the above system. In the absence of the mechanical degrees of freedom, the steady state electronic occupation at the transition between two fixed electron occupations (a and b) is given by

$$N_{a\leftrightarrow b} = \frac{\Gamma_{a\to b}}{\Gamma_{a\leftrightarrow b}} \tag{5.12}$$

where $\Gamma_{a\leftrightarrow b} = \Gamma_{a\to b} + \Gamma_{b\to a}$.

Assume that the instantaneous influence of mechanical motion is a weak correction to this occupation number. Thus, near the $n-1 \leftrightarrow n$ transition, the probability distribution for occupation n is written as

$$P_n = N_{n-1\leftrightarrow n} P + \delta P \tag{5.13}$$

where P is the joint probability distribution $P = P_{n-1} + P_n + P_{n+1}$, and δP is a weak perturbation. A similar expression can be used for $n \leftrightarrow n+1$ transition. For both cases, evaluating δP to first order gives

$$\delta P = \frac{\Gamma_{a\to b}\Gamma_{b\to a}}{(\Gamma_{a\leftrightarrow b})^3}\frac{F}{M}\frac{\partial P}{\partial v} - \frac{vPF}{\Gamma_{a\leftrightarrow b}}\frac{\partial N_{a\leftrightarrow b}}{\partial \mu} \tag{5.14}$$

where $a(b)$ is the lower(higher) occupation state.

Inserting equation 5.14 back into the coupled equations (5.9-5.11) and solving for the joint probability P, gives:

$$\frac{\partial P}{\partial t} + v\frac{\partial P}{\partial x} - m\omega_0^2 x\frac{\partial P}{\partial v} + \xi(x)\frac{\partial P}{\partial v} = \gamma(x)\frac{\partial vP}{\partial v} + D(x)\frac{\partial^2 P}{\partial v^2} \tag{5.15}$$

where

$$\xi(x) = \frac{F}{M}\left(\frac{\Gamma_{n\to n-1}}{\Gamma_{n\leftrightarrow n-1}} - \frac{\Gamma_{n\to n+1}}{\Gamma_{n\leftrightarrow n+1}}\right) \tag{5.16}$$

$$D(x) = \frac{F^2}{m^2}\left(\frac{\Gamma_{n-1\to n}\Gamma_{n\to n-1}}{(\Gamma_{n-1\leftrightarrow n})^2} + \frac{\Gamma_{n\to n+1}\Gamma_{n+1\to n}}{(\Gamma_{n\leftrightarrow n+1})^2}\right) \tag{5.17}$$

$$\gamma(x) = \frac{F^2}{M}\left(\frac{1}{\Gamma_{n-1\leftrightarrow n}}\frac{\partial N_{n-1\leftrightarrow n}}{\partial \mu} + \frac{1}{\Gamma_{n\leftrightarrow n+1}}\frac{\partial N_{n\leftrightarrow n+1}}{\partial \mu}\right) + \frac{\omega_0}{Q} \tag{5.18}$$

with the position dependence coming from the dependence of Γ_* on $\mu_{dot} = \mu_0 + Fx$.

The motion of the dot is now assumed to follow a harmonic oscillator description

$$x = A\sin(\phi) \tag{5.19}$$

$$v = A\,\omega_0\cos(\phi) \tag{5.20}$$

where $\phi = \omega_0 t$.

Under the assumption that the mechanical oscillation energy is approximately constant over one oscillation period (ie, $Q \gg 1$), then the probability P will not depend strongly on ϕ. In this case equation 5.15 can be averaged over a single oscillation (i.e., averaged over the phase, ϕ), and evaluated as a function of amplitude. It further simplifies the resulting expression to express the amplitude by the energy of the oscillator $E = \frac{1}{2}m\omega_0^2 A^2$. Then equation 5.15 can be written

$$\frac{\partial P}{\partial t} - \sqrt{2EM}\langle\xi(x)\cos(\phi)\rangle\frac{\partial P}{\partial E} = \langle\gamma(X)\left(P + 2E\cos^2(\phi)\frac{\partial P}{\partial E}\right)\rangle + \langle D(x)\left(M\frac{\partial P}{\partial E} + 2EM\cos^2(\phi)\frac{\partial P^2}{\partial^2 E}\right)\rangle \tag{5.21}$$

where $\langle f\rangle = \frac{1}{2\pi}\int_0^{2\pi} f d\phi$ is the phase averaged contribution of f.

The contribution of $\xi(x)$ is of the form $\int_0^{2\pi} f(A\sin(\phi))\cos(\phi)d\phi$. By the symmetry of $\cos(\phi)$, $\sin(\phi)$ this term will then be zero for any single-valued function $f(x)$.

Finally, to simplify the final expression it can be shown that $\frac{\partial}{\partial E}\langle 2E\gamma(x)\cos^2\phi P\rangle = \langle\gamma(X)\left(P + 2E\cos^2(\phi)\frac{\partial P}{\partial E}\right)\rangle$ and $\frac{\partial}{\partial E}\langle 2ED(x)\cos^2\phi\frac{\partial P}{\partial E}\rangle = \langle D(X)\left(\frac{\partial P}{\partial E} + 2E\cos^2(\phi)\frac{\partial P^2}{\partial^2 E}\right)\rangle$ so that equation 5.21 can be written in the abbreviated form

$$\frac{\partial P}{\partial t} = \frac{\partial}{\partial E}\left(2E\gamma_1 P + 2EMD_1\frac{\partial P}{\partial E}\right) \tag{5.22}$$

where $\gamma_1 = \langle\gamma(x)\cos^2(\phi)\rangle$ and $D_1 = \langle D(x)\cos^2(\phi)\rangle$.

The stationary solution to equation (5.22) is

$$P(E) \propto \exp\left(-\int_0^E \frac{\gamma_1(E')}{MD_1(E')}dE'\right) \tag{5.23}$$

For the Coulomb blockade region of interest in this letter, equation (5.23) will always permit a non-zero peak at $E = 0$, which corresponds to zero motion. The regime of interest

for self-driven oscillation is then when there exists a second probability peak at non-zero E. In this case, the oscillator-quantum dot system can sustain self-driving at a finite amplitude. The experimental observation of in-diamond current in figure 5.6a suggests occupation of these higher energy states. In the following simulations we consider the case in which the higher energy state is occupied whenever it has a nonzero probability. This could, for example, be driven by thermal fluctuations of the resonator temporarily driving to a regime of negative damping, which is then rapidly driven to a larger stable oscillation amplitude.

A necessary condition for non-zero solutions in the $P(E)$ is that the damping term, $\gamma(x)$, is negative for some x, which requires

$$\frac{\partial N_{a\leftrightarrow b}}{\partial \mu} < -\frac{M\Gamma_{a\leftrightarrow b}}{F^2}\frac{\omega_0}{Q} \tag{5.24}$$

This requires a high Q mechanical resonator and some tunnel barrier energy dependence. An example of the average occupation ($N_{a\leftrightarrow b}$) across a finite bias Coulomb peak with energy dependent tunneling is shown in figure 5.8, along with the resultant damping. Self-driven oscillations are possible when the motion-averaged damping becomes negative. This occurs when there exists a region of negative γ within a transition, and only small positive damping contributions at the transition edges.

5.3.4 CNT Tunnel Barriers

As noted in the previous section, observation of non-zero self-driven oscillation energies require the tunnel rates to the quantum dot to have some energy dependence. Energy-dependent tunnelling is typical for electrically defined quantum dots with wide, low tunnel barriers [82] and have been observed previously in suspended CNT devices [19]. Band-to-band tunneling in the carbon nanotube could further enhance energy dependence and bias direction dependence, as illustrated in figure 5.9. Further energy dependence could also result from mechanisms such as finite density of states in the leads [83], and non-uniform profile of CNT potential above contacts [84, 85, 86]. For example, in the extreme case of the leads having discrete energy-resolved states (eg, leads are also quantum dots) tunneling would occur only on resonance with lead energy levels.

For simplicity, we use a phenomenological model of the tunnel rates similar to that which was previously applied to CNT quantum dots [19],

$$\Gamma^{s,d} = \Gamma_0^{s,d} e^{b_{s,d}^{-,+}\Delta\mu_{s,d}} f_F(\Delta\mu_{L,R}) \tag{5.25}$$

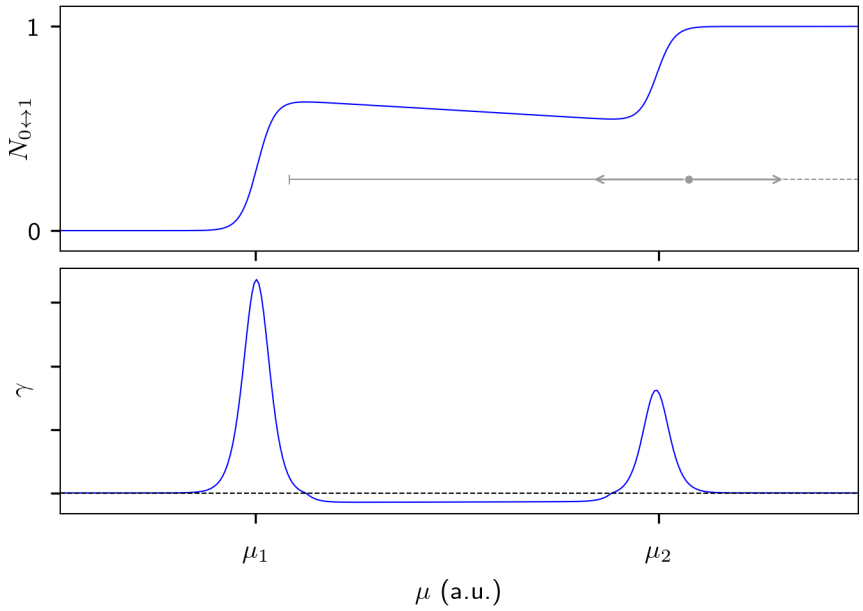

Figure 5.8: Energy dependent tunneling across a single electron occupation transition at finite bias, in which sequential tunneling occurs when the dot chemical potential is within the bias window ($\mu_1 < \mu < \mu_2$). For energy dependent tunneling, the average occupation ($N_{0\leftrightarrow1}$) is not fixed within this transition, as shown in the top panel. This can result in negative damping of the mechanical motion, γ, demonstrated in the lower panel. In the negative damping regime, oscillations will increase in amplitude until reaching a stable amplitude at the edge of positive damping. The grey illustration in the upper panel depicts a mechanical-dot system near the μ_2 edge entering into this negative damping region and increasing in amplitude until stabilizing at a large self-driven oscillation.

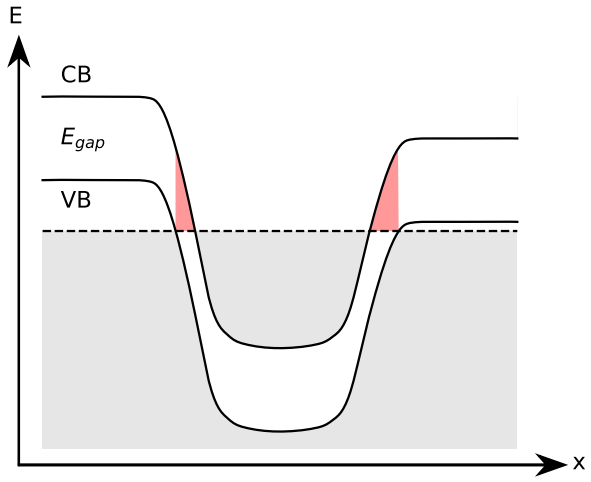

Figure 5.9: Illustration of CNT energy diagram as a function of position for the suspended CNT device, highlighting the band-to-band energy barriers. The energy above the source and drain contacts depends only on the bias offset. The gate under the center region lowers the energy, defining the electron occupied quantum dot between the barriers created by the CNT bandgap. The width and shape of these barriers depends on gate voltage and bias direction.

where $\Delta\mu_{s,d} = (\mu_{dot} - \mu_{s,d})$, $\mu_{s,d}$ is the energy level of the source/drain contact, $\Gamma_0^{s,d}$ is the resonant tunnel rate at $\Delta\mu_{s,d} = 0$, $f_F()$ is the Fermi function, and $b_{s,d}^{-,+}$ are fitting parameters for the energy dependence from the source/drain contact at negative/positive bias.

5.3.5 Determining DC Conductance

To demonstrate the effect that self-driven oscillations have on DC measurements, consider the differential conductance in a region of V_g and V_{sd} spanning one Coulomb diamond. For each (V_g, V_{sd}) point in the region of interest, determine the stationary dot potential, μ_0 from equation 5.4, and the dependence of all tunnel rates on offset position by equations 5.25 and 5.8. Then, solve for the mechanical energy probability distribution, $P(E)$ in equation 5.23.

If a self-driven state is supported, the measured current will be averaged over the mechanical oscillation. For a quantum dot undergoing sequential tunneling, the current from left to right leads depends on the tunneling rates onto and off the dot at each lead. In

the case of non-zero motion of the dot, each of these tunnel rates Γ will depend on position x, and the current measured at bandwidths less than the oscillation frequency will be

$$I = \langle I(x) \rangle = \sum_{\{a,b\}=[\{n-1,n\},\{n,n+1\}]} e \left\langle \frac{\Gamma^s_{a\to b}(x)\Gamma^d_{b\to a}(x) - \Gamma^s_{b\to a}(x)\Gamma^d_{a\to b}(x)}{\Gamma_{a\leftrightarrow b}(x)} \right\rangle \tag{5.26}$$

Finally, after determining the current at each (V_g, V_{sd}), the differential conductance $\frac{\partial I}{\partial V_{sd}}$ is calculated to produce a simulation of the conductance experiments.

5.4 Results

Figure 5.10a shows one occupation level of the differential conductance experiment previously shown in figure 5.6a. Figure 5.10b shows a simulated differential conductance using the model presented above over an equivalent gate voltage range with the device values determined previously, and $b^{-,+}_{s,d}$ as fitting parameters. For the parameters shown, the simulation qualitatively reproduce many of the features observed in the experiments. Primarily, the self driven features are absent at low bias, and abruptly stop at the mid-line of the Coulomb diamond. At this mid-line the mechanical oscillations begin to interact with both the $n \to n-1$ and $n \to n+1$ transitions simultaneously leading to large positive damping. The low bias gap is a result of the thermal broadening of the shoulders (at μ_1 and μ_2 in figure 5.8) overtaking the negative slope region of $\langle N \rangle$. Also note the appearance of the bright line within the conductance feature at negative bias that runs parallel to the opposite Coulomb diamond edge. At this bright ridge, the self-oscillation created by energy dependence in the $n \to n-1$ transition has sufficient amplitude to allow transport through the $n+1$ energy level for a portion of the oscillation period, resulting in a sharp increase in conductance.

Figure 5.11 shows both experimental and simulated differential conductance for the same parameter space, at elevated temperature $T = 800$ mK. As temperature increases, the self oscillation feature size decreases and requires larger bias voltage before observation. The temperature dependence of the simulated self oscillation is weaker than experimental measurements, likely due to temperature dependence of the tunneling parameters, Γ_0 and $b^{-,+}_{s,d}$, which is not considered in the simulation.

The presence of the in-diamond self-driven oscillation features indicate a strong energy dependence of tunneling at the adjacent Coulomb diamond edge. Changing of the energy dependence parameters, $b^{-,+}_{s,d}$ shift the low-bias threshold below which the self-oscillations

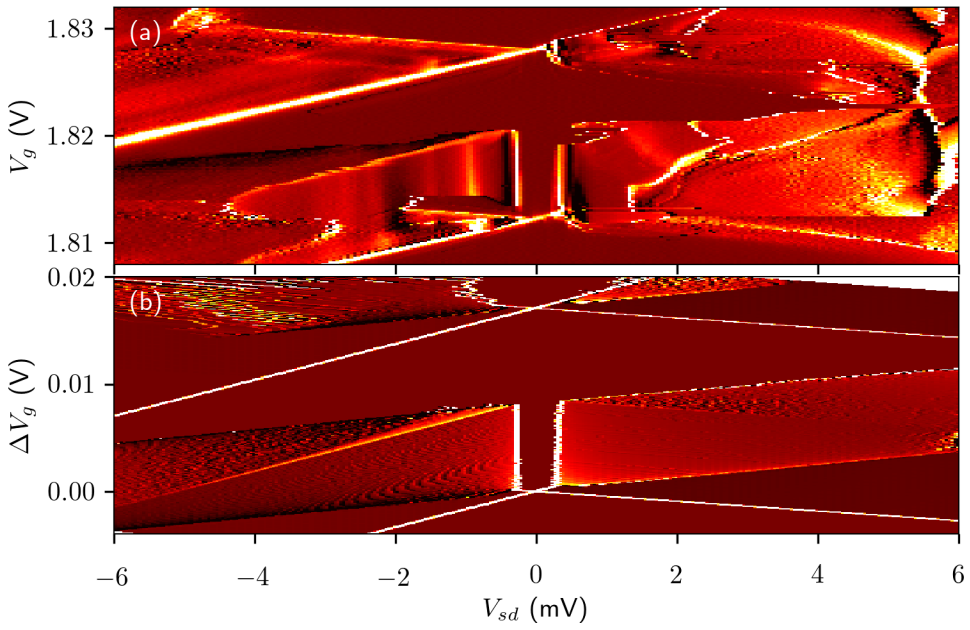

Figure 5.10: **a** Differential conductance measured at T = 30 mK, showing self-driven oscillation feature in the Coulomb diamond region between two electron occupation transitions. **b** Simulated differential conductance using the master equation model described in text, with best-fit energy dependent tunneling parameters $b_s^+ = b_d^- = 6\,\mathrm{meV}^{-1}$, $b_d^+ = b_s^- = 0.2\,\mathrm{meV}^{-1}$.

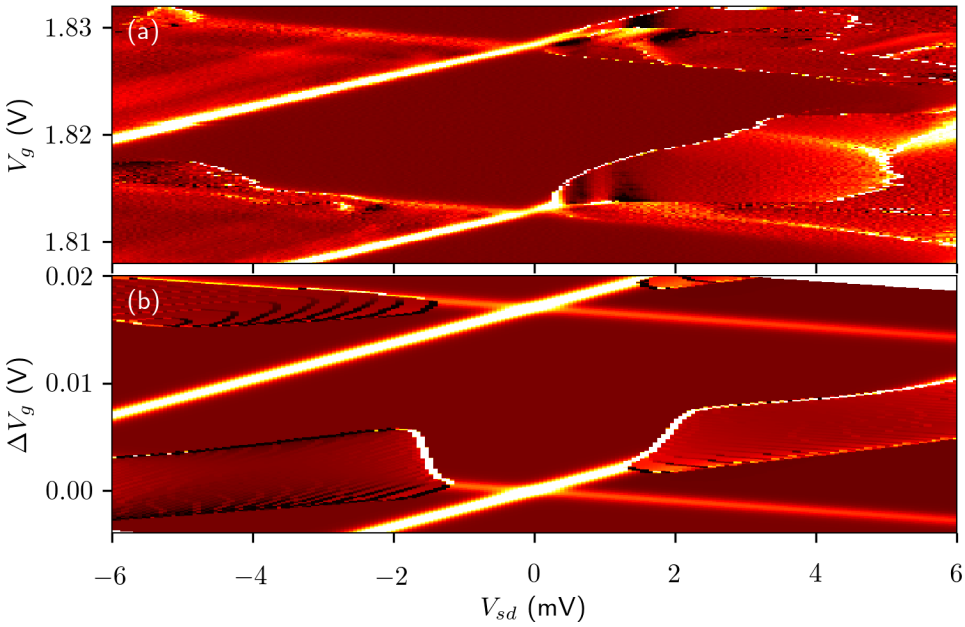

Figure 5.11: Differential conductance measurement, **a**, and simulation, **b**, at temperature T = 800 mK, using the same simulation parameters as the T = 30 mK simulations.

are not observed. For the simulation presented in 5.10b, decreasing $b_{s,d}^{-,+}$ by a factor of 10 completely suppresses the self-oscillation features.

5.5 Further observation of self-driven oscillations

Self-driven oscillations were also observed in the same device for other gate voltage ranges, and under applied magnetic fields. With changing parameters, the edge of the Coulomb diamond along which the self-driven features are seen varies, suggesting changes of the tunnel energy dependence. Figure 5.12 shows differential conductance measurements taken at several different gate voltage regions on the same device.

Under an applied magnetic field, the tunneling between contacts and the CNT will be modified and some change of the self-driven features is expected. Figure 5.13 shows a differential conductance measurement in the same region as 5.6a, but with an applied axial magnetic field of 2 T. The self-driven oscillations are heavily modified, most notably the in-diamond conduction features for $V_{sd} > 0$ occur on the opposite edge of the Coulomb Diamond.

In-diamond self-driven oscillations were also observed in a second suspended CNT device on the same chip, called device B. Figure 5.14 shows some basic characterization of this device. From the Euler-Bernoulli beam fitting shown in figure 5.14c, the estimated device parameters are a CNT diameter of 2.9 nm, suspended length of 2.3 μm, and a residual compression of $T_0 = 0.4$ nN. Resonance peak linewidth (not shown) gives $Q > 5 \cdot 10^3$. Figure 5.15 shows differential conductance measurements at two different gate voltage ranges in device B, in which the self-driven oscillation features qualitatively similar to those in the primary device were observed.

5.6 Conclusion

High sensitivity nanomechanical measurements require control and understanding of the mechanical state of the measurement device. In this chapter, I have presented the observation and description of a self oscillation feature that can be observed in Coulomb blockade conductance of suspended carbon nanotubes when measured at sub-Kelvin temperatures. These stable, large amplitude oscillations could interfere with the usual operation of these devices as nanomechanical sensors when cooling to sub-Kelvin temperatures. This temperature regime is frequently used for general high sensitivity nanomechanical devices to

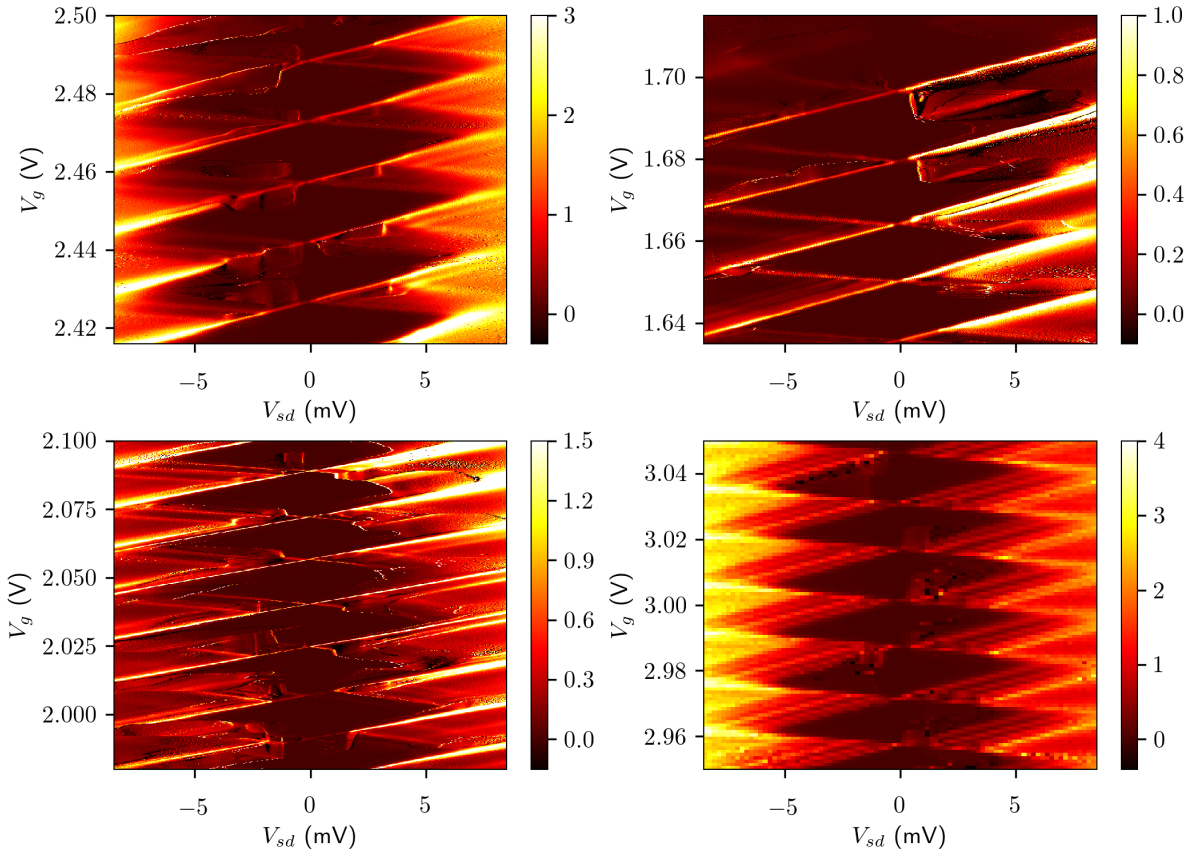

Figure 5.12: Differential conductance measurements as a function of gate voltage and applied bias, measured in the main device at 30 mK. In each gate voltage range shown, finite conductance features similar to those discussed in the main text are observed. The location of these features within the Coulomb diamonds differ for each gate voltage range, indicating a change in the tunneling energy dependence.

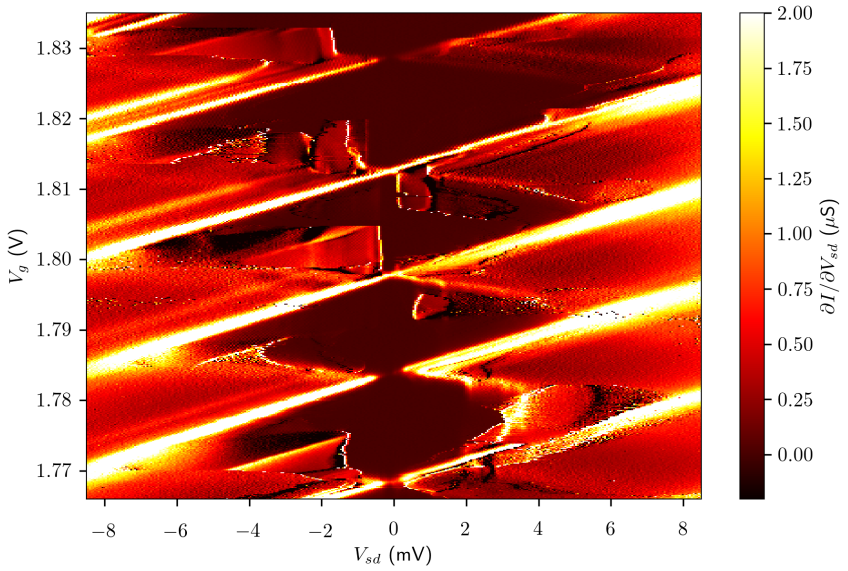

Figure 5.13: Differential conductance as a function of bias and gate voltage, in the presence of an applied axial magnetic field of $B_{\parallel} = 2$ T.

reduce thermal noise. It is also particularly important for nanomagnet sensing applications, as many molecular nanomagnets require sub-Kelvin temperature to enter well defined spin ground states.

While potentially interfering with traditional driven operation, the self-driven oscillations could provide benefits to nanomechanical sensing if properly harnessed. Self-driven oscillations may exhibit narrower linewidths than the intrinsic driven resonator linewidth [87], and a properly tailored electromechanical coupling can provide a pathway to active cooling of the mechanical state [73]. Additionally, with sensitive frequency resolved readout [41], self-driven oscillations may be used for sensitive mass/force detection without the need for high frequency external excitation to the device [88].

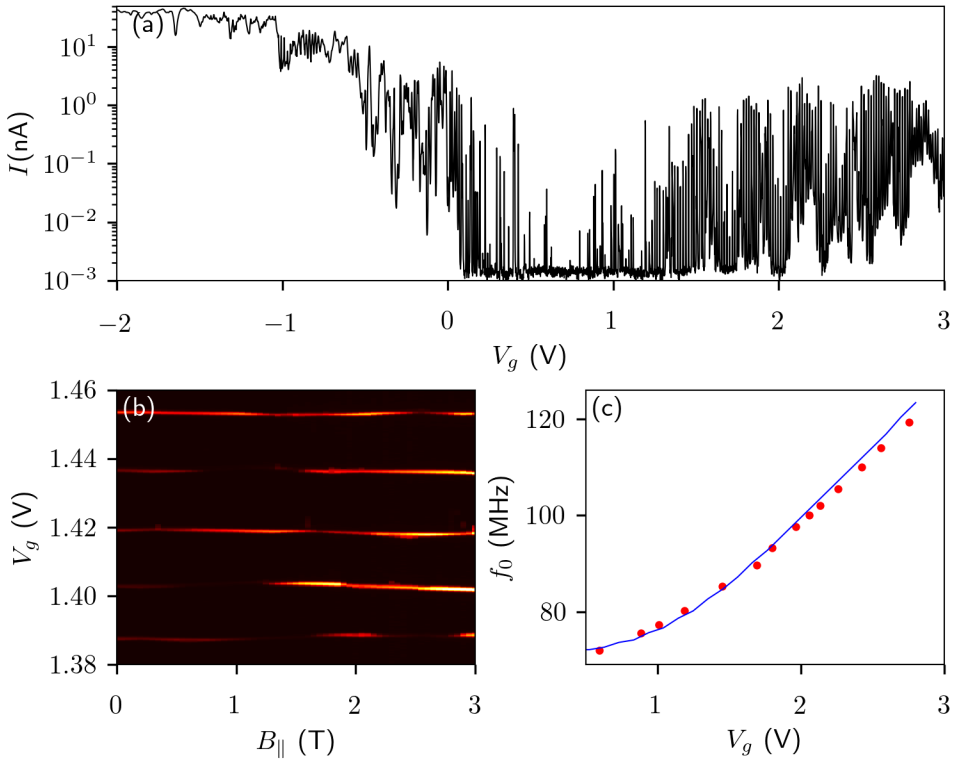

Figure 5.14: **a**. Current as a function of applied gate voltage for a second suspended CNT device on the same chip. Similar to the primary device, this shows large currents for $V_g < 0$ and lower, Coulomb-blockaded conductance for $V_g > 1$ V. **b**. Conductance peak positions as a function of applied axial magnetic field. The peak slopes give an orbital magnetic moment of ≈ 0.58 meV/T, corresponding to a CNT diameter of 2.9 nm. **c**. Resonance frequency as a function of gate voltage, and an Euler-Bernoulli beam model fit using CNT diameter of 2.9 nm, suspended length of 2.3 μm, and residual compression of $T_0 = 0.4$ nN.

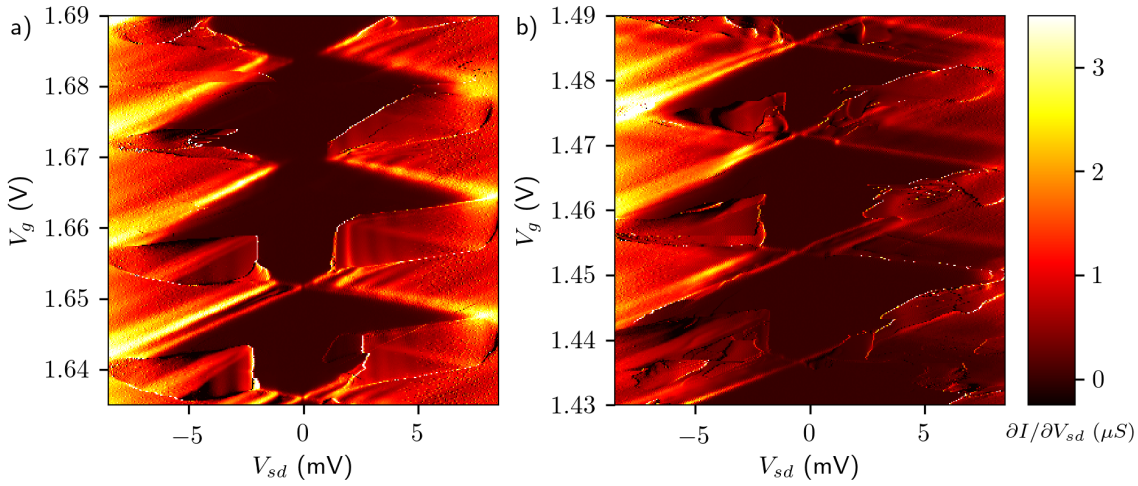

Figure 5.15: Differential conductance measured in device B. Self-driven oscillation features of finite conductance are observed within the nominally Coulomb blockaded diamond regions.

Chapter 6

Continuous wave noise spectroscopy beyond weak coupling

In this chapter, I discuss a research problem separate from the previous investigation of suspended carbon nanotubes. In particular, I'm addressing the quantum information processing problem of a spin qubit interacting with a noisy environment (bath), and how to accurately quantify the action of the noise on the qubit evolution.

6.1 Introduction

For many solid-state qubits, single-axis phase noise is the dominant noise process, and the environmental interactions are well described in a stochastic semi-classical approximation. For example, a typical system-environment Hamiltonian can be written $H_{SE} = \sigma_z^{(s)} \sum_i \lambda_i \sigma_z^{(i)}/4$, where $\sigma^{(s)}$ ($\sigma^{(i)}$) is the Pauli operator for the system (environment) and λ_i is the coupling strength. For many environmental states in the spin bath, and with intra-bath couplings strong compared to system couplings, the Hamiltonian can be approximated semi-classically, $H_{sc}(t) = f(t)\sigma_z/2$, where $f(t)$ is a stationary, Gaussian-distributed function with zero mean, i.e. $\langle f(t) \rangle = 0$. These properties will be assumed throughout the remainder of the chapter.

For systems described in this manner, the time correlation of the noise $f(t)$ is an important property for understanding the system dynamics and optimizing qubit control [89]. This is most frequently represented by the noise spectral density, $S(\omega)$, the Fourier transform of the two point time correlation. One way to estimate $S(\omega)$ is to measure the

response of the qubit to dynamical decoupling pulse sequences [90, 91, 92, 93, 94, 95, 96, 97, 98]. The evolution can be understood using the overlap integral approach in which the evolution is a convolution of the noise spectrum, $S(\omega)$, and an overlap filter determined by the decoupling pulse, $|F(\omega,T)|^2$ [99, 100, 101, 102, 103]. For example, under a series of equally spaced, instantaneous π pulses (CPMG sequence), the bath-traced Hamiltonian becomes $H_{sc}(t) = y(t)f(t)\sigma_z/2$ where $y(t)$ alternates between $+1$ and -1 at a period corresponding to the pulse spacing τ. In this case, the decay of qubit coherence is predicted to be $\langle\sigma_x(T)\rangle = \langle\sigma_x(0)\rangle e^{-\chi(T)}$, where the time-dependent decay rate is determined by the overlap integral of the noise spectral density and the frequency-domain filter function

$$\chi(T) = \int_{-\infty}^{\infty} d\omega S(\omega)|F(\omega,T)|^2. \tag{6.1}$$

For the CPMG sequence, $|F(\omega,T)|^2$ has peaks at frequency $\Omega = \pi/\tau$ and its harmonics, $k\Omega$. For sufficiently long decay time $T \gg 2\tau$, the peaks approach a delta-function limit, allowing for narrow band-pass filtering of the noise $S(\omega)$. A protocol for estimating $S(\omega)$ using the discrete form of equation 6.1 and by taking the harmonics into account was designed and implemented experimentally in reference [91].

The CPMG pulsed method becomes disadvantageous at high probe frequencies, when the finite pulse width effects cannot be ignored and limit the minimum pulse spacing. Moreover, the lowest frequency (given by the maximum pulse delay) dictates the frequency resolution with which the spectral density function is probed [91]. This makes the protocol inefficient in certain situations. For example, probing an unknown noise spectrum over a wide frequency window requires a very large number of experiments.

An alternative approach is to monitor coherence decay under a continuous wave (CW) "spin-locking" pulse, also known in NMR literature as a $T_{1\rho}$ measurement. In this case, the qubit dynamics can only be evaluated perturbatively due to the non-commutativity of the effective Hamiltonian. $T_{1\rho}$ experiments have been used in NMR to probe slow atomic motions that give rise to fluctuations in the dipolar field [104, 105, 106, 107]. The NMR literature, however, has not directly addressed the problem of extracting an unknown and arbitrary $S(\omega)$. This was first addressed using the generalized Bloch equations (GBE) formalism [108, 94]. The generalized Bloch equations were derived to describe the relaxation dynamics of a system simultaneously interacting with a heat bath and an arbitrarily strong excitation field. The derivation is based on the following assumptions: (1) the system and the bath are weakly coupled, and are initially in a product state; (2) the time scale of the relaxation of the system is much slower than that associated with the decay of the bath correlation functions and the period of the driving field; (3) the bath-induced coherent system dynamics are negligible compared to that induced by the system Hamiltonian; (4)

the rotating wave approximation (RWA) is valid. The weak coupling assumption means that only terms up to second order in the system-bath coupling strength, $f(t)$, are retained. The second assumption leads to the aforementioned delta-function approximation. For the noise model described earlier, the GBE predicts an exponential decay of coherence $\langle\sigma_x\rangle$ in the CW driving experiment. The decay rate is directly proportional to $S(\Omega)$ where Ω is the driving amplitude (Rabi frequency). Note that the decay rate here is time independent and thus cannot capture non-Markovian dynamics. The CW approach can often perform well to higher frequencies than the pulsed method, since finite pulse width effects tend to appear before the maximum excitation power is reached or before the RWA is violated. Moreover, the CW protocol can be more experimentally efficient than pulsed methods since a single coherence decay measurement yields the spectral density of noise at the target frequency. CW noise spectroscopy was demonstrated experimentally in Ref. [92] for optically-trapped ultracold atoms coupled to a collisional bath, and in Ref. [96] in the context of superconducting qubit decoherence. In the latter case, the analysis was based on the GBE but included more general noise (relaxation) than considered here.

Neither the CW nor pulsed methods can probe to arbitrarily low frequencies using the standard analysis above. In these analyses, the number of drive field periods (decoupling cycles) should be large enough to justify the delta function approximation, i. e. $\Omega T/(2\pi) >> 1$. Since the signal decay timescale is $T \sim 1/S(\Omega)$, the minimum probe frequency is limited by the condition $\Omega >> 2\pi S(\Omega)$ (where $\Omega = \pi/\tau$ in the pulsed method). The main goal of this chapter is to study spin dynamics under CW excitation beyond approximations (1) and (2) above, so that the signal decay at low frequencies $\Omega \sim 2\pi S(\Omega)$ can be better modeled. This information is then used to increase the spectral range over which noise spectroscopy produces valid results. The state evolution is described in the Liouville representation [109] and the cumulant expansion method [110, 111] is used to calculate the ensemble average, finding the functional form of the coherence decay up to fourth order in $f(t)$ (or second order in $S(\omega)$). The resulting equations are derived without any assumptions about the CW pulse length or the bath correlation time, in order to capture non-Markovian behaviour. These results are used to design a CW noise spectroscopy protocol that extends the range for which $S(\omega)$ can be accurately determined down to $\omega = 0$.

6.2 Coherence decay function

In this section the coherence decay function of a system under CW driving is derived as a function of the spectral density, $S(\omega)$, of Gaussian, zero-mean semi-classical phase noise

as introduced above. In the interaction frame of the CW pulse of amplitude Ω along σ_x in the rotating frame, the semi-classical stochastic Hamiltonian transforms in time t as

$$\tilde{H}_{sc}(t) = f(t)(\cos(\Omega t)\sigma_z + \sin(\Omega t)\sigma_y)/2. \tag{6.2}$$

The derivation of the coherence decay function under this Hamiltonian must involve perturbation series, since $[\tilde{H}_{sc}(t_1), \tilde{H}_{sc}(t_2)] \neq 0$. Using stochastic Liouville theory and super operator formalism [109], the ensemble averaged qubit evolution can be described as $\langle\hat{\hat{\rho}}(T)\rangle = \langle\Lambda(T)\rangle\hat{\hat{\rho}}(0)$, where $\rho(T)$ is the density matrix decribing the qubit at time T, $\langle\cdot\rangle$ denotes ensembles averaging over noise realizations, $\hat{\cdot}$ denotes vectorization that stacks the rows of a $d \times d$ matrix into a $d^2 \times 1$ vector, and

$$\Lambda(T) = \mathcal{T}\exp\left\{-i\int_0^T \mathcal{L}(t)dt\right\}, \mathcal{L}(t) = \tilde{H}^*_{sc}(t) \otimes \mathbb{1} - \mathbb{1} \otimes \tilde{H}_{sc}(t), \tag{6.3}$$

where $\mathbb{1}$ is the unit matrix, and $\mathcal{T}$ is the Dyson time ordering operator [111]. The ensemble average of the noisy operator $\Lambda(T)$ can be evaluated with the cumulant expansion

$$\langle\Lambda(T)\rangle = \exp\{K(T)\}, \quad K(T) = \sum_{n=1}^{\infty} \frac{(-iT)^n}{n!} k_n, \tag{6.4}$$

where $K(T)$ is called the cumulant function and k_n is called the nth cumulant [110, 111]. By Taylor-expanding and comparing equations 6.3 and 6.4, the cumulants can be found.

For the Hamiltonian in equation 6.2, the powers of $\mathcal{L}(t)$ are linear combinations of the operators from following set:

$$\mathcal{N} = \{\mathbb{1} \otimes \mathbb{1},\ \sigma_x \otimes \sigma_x,\ \sigma_y \otimes \sigma_y,\ \sigma_z \otimes \sigma_z,\ \sigma_x \otimes \mathbb{1} - \mathbb{1} \otimes \sigma_x,\ \sigma_y \otimes \sigma_z - \sigma_z \otimes \sigma_y\}, \tag{6.5}$$

Moreover, k_n is proportional to the nth power of $\mathcal{L}(t)$. As a result, k_n is a linear combination of the operators in $\mathcal{N}$. Thus, $\langle\Lambda(T)\rangle$ can be expressed as

$$\langle\Lambda(T)\rangle = \exp\left(\sum_{m=1}^{|\mathcal{N}|} a_m \mathcal{N}_m\right), \tag{6.6}$$

where $\mathcal{N}_m$ is the mth element in $\mathcal{N}$. In the spin-locking experiment, the normalized signal is

$$\langle\sigma_x(T)\rangle = \frac{\hat{\hat{\sigma}}_x^{\mathrm{T}}\langle\Lambda(T)\rangle\hat{\hat{\sigma}}_x}{\hat{\hat{\sigma}}_x^{\mathrm{T}}\hat{\hat{\sigma}}_x} \tag{6.7}$$

$$= \frac{\langle\Lambda(T)\rangle_{2,2} + \langle\Lambda(T)\rangle_{2,3} + \langle\Lambda(T)\rangle_{3,2} + \langle\Lambda(T)\rangle_{3,3}}{2} \tag{6.8}$$

where $\langle\cdot\rangle_{i,j}$ is the element of an operator at row i and column j. Combining equations 6.6 and 6.7,

$$\langle\sigma_x(T)\rangle = \exp\left(a_1 + a_2 + a_3 - a_4\right). \tag{6.9}$$

It is convenient to write above equation as

$$\langle\sigma_x(T)\rangle = \exp\left(\sum_n a_{1,n} + a_{2,n} + a_{3,n} - a_{4,n}\right) \tag{6.10}$$

$$= \exp\left(\sum_n \chi_n(T)\right), \tag{6.11}$$

where $\sum_n a_{m,n} = a_m$, and the index n indicates that the contribution is linked to the nth cumulant. The above equation has several significant implications. First, the average signal in the $T_{1\rho}$ measurement is an exponential function whose argument (decay rate) is given as a perturbation series. Second, the nth order decay rate is proportional to k_n, and therefore proportional to the ensemble average of products of Liouvillians, $\langle\prod_{j=1}^n \mathcal{L}(t_j)\rangle$, and hence proportional to the average over products of the classical Gaussian distributed random variable, $\langle\prod_{j=1}^n f(t_j)\rangle$). Third, the nth order decay rate can simply be calculated from the coefficients of the $\mathbb{1}\otimes\mathbb{1}$, $\sigma_x\otimes\sigma_x$, $\sigma_y\otimes\sigma_y$, and $\sigma_z\otimes\sigma_z$ terms corresponding to the nth order cumulant, independently from other cumulants. Moreover, since $f(t)$ is Gaussian-distributed with zero mean, for an integer n, $\langle f(t_1)\dots f(t_{2n-1})\rangle = 0$ according to Isserlis' Gaussian moment theorem [112]. Subsequently, only even order cumulants are non-zero, and the first few terms are

$$k_2 = \frac{1}{T^2}\mathcal{T}\int_0^T dt_1\int_0^T dt_2\langle\mathcal{L}(t_1)\mathcal{L}(t_2)\rangle, \tag{6.12}$$

$$k_4 + 3k_2^2 = \frac{1}{T^4}\mathcal{T}\int_0^T dt_1\int_0^T dt_2\int_0^T dt_3\int_0^T dt_4\langle\mathcal{L}(t_1)\mathcal{L}(t_2)\mathcal{L}(t_3)\mathcal{L}(t_4)\rangle, \tag{6.13}$$

$$k_6 + 15(k_2k_4 + k_2^3) = \frac{1}{T^6}\mathcal{T}\int_0^T dt_1\cdots\int_0^T dt_6\langle\mathcal{L}(t_1)\cdots\mathcal{L}(t_6)\rangle. \tag{6.14}$$

In the following subsections, the first two non-zero decay terms are calculated. In the limit of $T\to\infty$, the 2nd order decay rate is identical to the GBE result. To go beyond the GBE-based analysis, the large T approximation is omitted, and the qubit dynamics including the 4th order decay rate are considered.

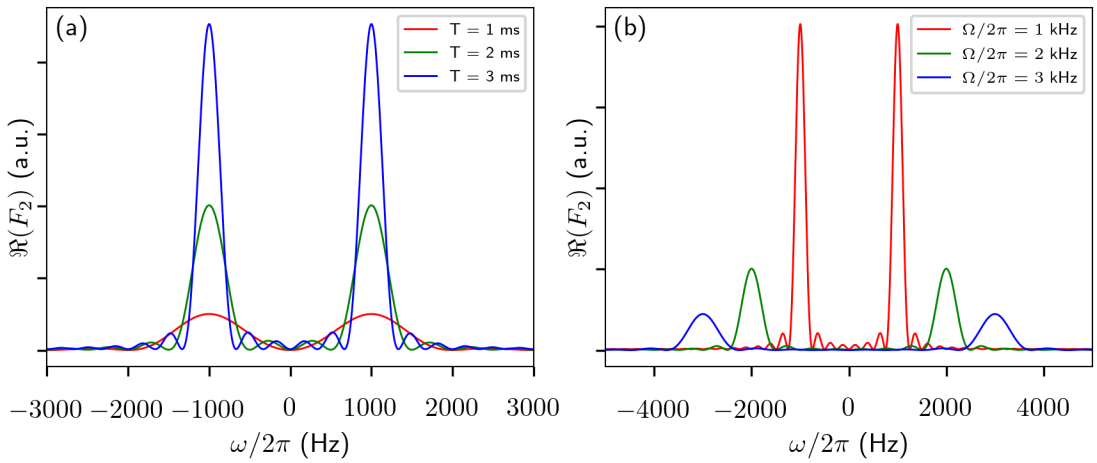

Figure 6.1: The real parts of $\mathcal{F}_2(\omega, \Omega, T)$, for (a) $\Omega/2\pi = 1000$ Hz and $T = 1,\ 2,\ 3$ ms, and (b) for $T = 8\pi/\Omega$ and $\Omega/2\pi = 1000,\ 2000,\ 3000$ Hz.

6.2.1 Second-order decay rate

To find $a_{m,2}$, expand equation 6.12 (the 2nd order cumulant) using the operators in equation 6.5. Then equation 6.11 is used to find the decay rate attributed to the 2nd order cumulant

$$\chi_2(T) = -\int_0^T dt_1 \int_0^{t_1} dt_2 \langle f(t_1) f(t_2) \rangle \cos\left(\Omega\left(t_1 - t_2\right)\right) \tag{6.15}$$

$$= -\frac{1}{2\pi} \int_{-\infty}^{\infty} d\omega S(\omega) \mathcal{F}_2(\omega, \Omega, T) \tag{6.16}$$

where

$$\mathcal{F}_2(\omega, \Omega, T) = \int_0^T dt_1 \int_0^{t_1} dt_2 \mathrm{e}^{i\omega(t_1 - t_2)} \cos\left(\Omega\left(t_1 - t_2\right)\right).$$

The imaginary part of $\mathcal{F}_2(\omega, \Omega, T)$ is an odd function with respect to ω, and $S(\omega)$ is an even function, thus equation 6.16 can be further simplified as

$$\chi_2(T) = -\frac{1}{2\pi} \int_{-\infty}^{\infty} d\omega S(\omega) \mathrm{Re}\left(\mathcal{F}_2\left(\omega, \Omega, T\right)\right). \tag{6.17}$$

Figure 6.1 shows the real parts of $\mathcal{F}_2(\omega, \Omega, T)$ for fixed values of (a) Ω and (b) the number of Rabi cycles $l = \Omega T/2\pi$. The even function $\mathrm{Re}\left(\mathcal{F}_2\left(\omega, \Omega, T\right)\right)$ behaves like $\delta(\omega \pm \Omega)$

as $T \to \infty$. Thus, for a fixed value of Ω and in the limit of $T \gg 1$, the 2nd order decay rate can be approximated as

$$\begin{aligned}\chi_2(T) &\approx -\frac{S(\Omega)}{\pi}\int_0^\infty d\omega \mathrm{Re}\left(\mathcal{F}_2\left(\omega,\Omega,T\right)\right)\\ &= -S(\Omega)T/2.\end{aligned} \tag{6.18}$$

The normalized spin signal attributed to the 2nd order cumulant in the limit of large T is then a simple exponential decay:

$$\langle\sigma_x(T)\rangle \approx \exp\left\{-S(\Omega)T/2\right\}. \tag{6.19}$$

This expression is equal to the result derived from the GBE in the high temperature limit $k_B\mathrm{T} >> \hbar\Omega$.

6.2.2 Fourth-order decay rate

Following the same steps as for the 2nd order term evaluation, the 4th order cumulant k_4 can be expressed in terms of the operators in equation 6.5, and the coefficients $a_{m,4}$ can be found. The decay rate attributed to the 4th order cumulant can be expressed as

$$\chi_4(T) = \int_0^T dt_1\int_0^{t_1} dt_2\int_0^{t_2} dt_3\int_0^{t_3} dt_4 \left\langle\prod_{i=1}^4 f(t_i)\right\rangle \prod_{j=1}^2 \cos\left(\Omega\left(t_{2j-1}-t_{2j}\right)\right) - \frac{1}{2}\left(\chi_2(T)\right)^2. \tag{6.20}$$

Using the Isserlis Gaussian moment theorem again, the 4th order correlation function is written as the product of 2nd order correlation functions: $\langle f(t_1)f(t_2)f(t_3)f(t_4)\rangle = \langle f(t_1)f(t_2)\rangle\langle f(t_3)f(t_4)\rangle + \langle f(t_1)f(t_3)\rangle\langle f(t_2)f(t_4)\rangle + \langle f(t_1)f(t_4)\rangle\langle f(t_2)f(t_3)\rangle$. The product of the 2nd order correlation function can be expressed in terms of the spectral density, $S(\omega)$ as before. Then, the 4th order decay rate can be rewritten compactly as

$$\chi_4(T) = \left(\frac{1}{2\pi}\right)^2\int_{-\infty}^\infty d\omega_1\int_{-\infty}^\infty d\omega_2 S(\omega_1)S(\omega_2)\mathcal{F}_4(\omega_1,\omega_2,\Omega,T), \tag{6.21}$$

where

$$\begin{aligned}\mathcal{F}_4(\omega_1,\omega_2,\Omega,T) &= \int_0^T dt_1\int_0^{t_1} dt_2\int_0^{t_2} dt_3\int_0^{t_3} dt_4 \prod_{j=2}^1 \cos\left(\Omega\left(t_{2j-1}-t_{2j}\right)\right)\\ &\times\left(e^{i\omega_1(t_1-t_2)}e^{i\omega_2(t_3-t_4)} + e^{i\omega_1(t_1-t_3)}e^{i\omega_2(t_2-t_4)} + e^{i\omega_1(t_1-t_4)}e^{i\omega_2(t_2-t_3)}\right)\\ &-\frac{1}{2}\mathrm{Re}\left(\mathcal{F}_2\left(\omega_1,\Omega,T\right)\right)\mathrm{Re}\left(\mathcal{F}_2\left(\omega_2,\Omega,T\right)\right).\end{aligned} \tag{6.22}$$

The time integration for $\mathcal{F}_4$ can be carried out analytically. Symmetries in the filter function $\mathcal{F}_4$ result in the imaginary component of the integral going to zero as was the case for 2nd order decay rate. Using the symmetry of $\mathrm{Re}(\mathcal{F}_4)$ the expression for the 4th order decay rate can be simplified to

$$\chi_4(T) = \frac{1}{2\pi^2}\int_0^\infty d\omega_1 \int_0^\infty d\omega_2 S(\omega_1)S(\omega_2)\tilde{\mathcal{F}}_4(\omega_1,\omega_2,\Omega,T), \tag{6.23}$$

where

$$\tilde{\mathcal{F}}_4(\omega_1,\omega_2,\Omega,T) = \mathrm{Re}\left(\mathcal{F}_4(\omega_1,\omega_2,\Omega,T) + \mathcal{F}_4(\omega_1,-\omega_2,\Omega,T)\right).$$

6.3 Accuracy of coherence decay

To evaluate the accuracy of the cumulant expansion decays, we simulated a set of experiments with known input noise spectra, $S_{input}(\omega)$. The simulated signal decays are generated by time-discretized unitary evolution of an initial state density matrix, using $N = 10,000$ randomly generated noise realizations. A cosine series representation, as described in reference [113], is used to generate the noise realizations, $f(t)$ in equation 6.2. This simulation method accurately represents stationary, Gaussian noise matching the input noise spectrum, and converges to the correct spectrum at a rate of 1/N, where N is number of noise samples used. For all noise spectra in this paper, $S_{input}(\omega)$ plateaus below $\omega = 1\,\mathrm{rad/s}$, i.e. $S_{input}(\omega') = S_{input}(1\,\mathrm{rad/s})$ for $\omega' < 1\,\mathrm{rad/s}$. These simulated signal decays are used in the following sections to represent experimental data. Since the number of noise realizations N is finite, $S_{in}(\omega)$ is recalculated using the N generated noise realizations, and this is treated as the true input spectrum.

Using the simple exponential expression from equation 6.19, $S(\omega)$ can be accurately determined when the assumptions listed in the introduction are valid, i.e. when the relaxation timescale is long compared to the drive field period ($\Omega/2\pi \gg S(\Omega)$). When this condition is not met, the signal decay can be non-exponential and the standard analysis can give inaccurate values for $S(\omega)$. Figure 6.2a shows the result of applying a least-squares exponential fit and using equation 6.19 to determine $S(\omega)$ for a $1/f$ input noise spectrum. In this example, $S_{input}(\omega) = 30\,\mathrm{Hz}^2/\omega$ and $S_0(\omega)$ was obtained by fitting simulated CW noise spectroscopy experiments at $\omega = 1, 2, 4, 8, 12, 16, 20, 24, 32, 40, 64, 100, 125\,\mathrm{rad/s}$. The insets show examples of the normalized signal decay $\langle\sigma_x(t)\rangle$, which becomes non-exponential at low Ω, leading to inaccurate $S(\Omega)$ values. Figures 6.2b and c show this same procedure applied to (b) a $1/f^2$ noise spectrum (c) and a $1/f$ noise spectrum with

100 times higher noise power than that shown in (a). Simulated CW experiments at $\omega = 1, 2, 4, 6, 8, 10, 12, 15, 20, 25, 30, 35, 40, 50, 120$ rad/s were used for figure 6.2b, and experiments at $\omega = 1, 10, 20, 40, 80, 120, 160, 320, 640, 1000, 1250$ rad/s were used for figure 6.2c.

The non-exponential signal decay displayed in the inset of figure 6.2a can be understood based on the shape of the overlap filter function with respect to $S(\omega)$ when the δ-function approximation no longer holds. Figure 6.2d shows a non-exponential signal decay, with χ_2 displayed in insets at certain time points in the decay, along with the noise spectrum $S(\omega)$. The finite width of the main filter function peak, as well as its satellite peaks, overlaps with large values of $S(\omega)$ at low frequencies, producing oscillations in the signal decay.

Figure 6.3 shows the error, as a function of decay time and drive field amplitude, between the simulated "experimental" signal decays and theoretical decays calculated using one of three different methods. Each calculation method uses the correct "guess" of $S(\omega) = S_{in}(\omega)$. Figure 6.3a shows the result of applying the simple exponential from equation 6.19. Figures 6.3b and c show the decays calculated via the cumulant expansion from equation 6.11, with (b) using only χ_2, and (c) using both χ_2 and χ_4.

The cumulant expansion method provides much better matching to signal decays at short times (t $<$ 0.5 s in the example in figure 6.3) compared to the standard exponential decay of equation 6.19. However, using only χ_2 introduce errors in the intermediate (20-35 rad/s) Ω region. Using the cumulant expansion up to fourth order ($\chi_2 + \chi_4$), the mismatch is reduced at all times over a large portion of the drive amplitudes ($\Omega \gtrsim 20$ rad/s for the parameters chosen in this example).

6.4 Noise spectroscopy based on the cumulant expansion

The $\chi_2 + \chi_4$ cumulant expansion method can be used to improve CW noise spectroscopy when the experimental signal decays become non-exponential. The accuracy of a given noise spectrum estimate $S'(\omega)$ can be tested by comparing the cumulant expansion signal decay, calculated using $S'(\omega)$, and the experimental decay. Furthermore, the non-exponential, oscillatory behaviour observed at short timescales is the result of a wide frequency filter that overlaps with $S(\omega)$ across a range of frequencies, sometimes extending to $\omega = 0$. This short-time behaviour thus contains broad spectral information and can be used to extend the range over which $S(\omega)$ can be determined. In particular, one can choose a drive frequency for which the signal decay is well-matched by the $\chi_2 + \chi_4$ calculation

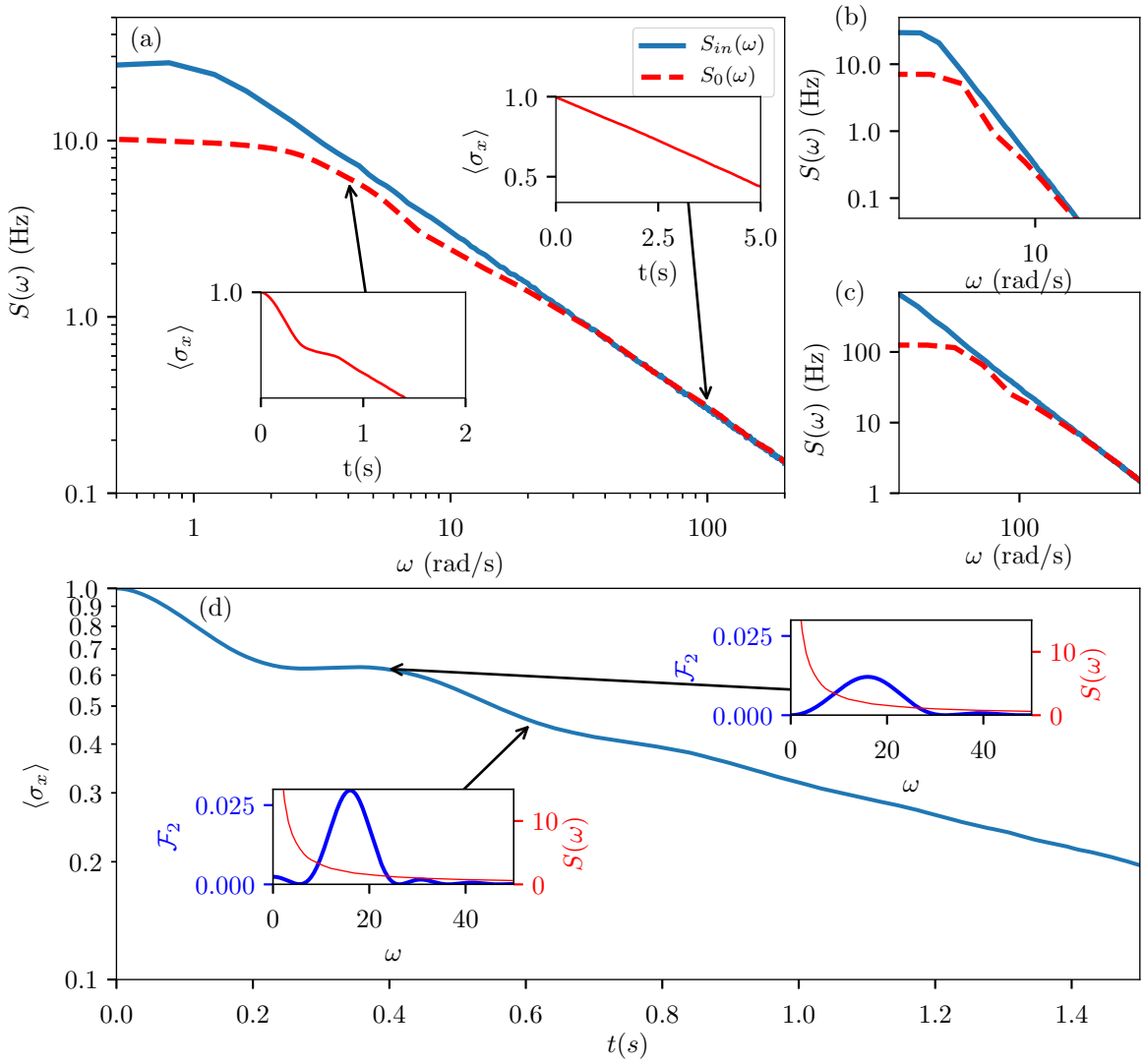

Figure 6.2: **a** Determination of $S(\omega)$ using simple exponential fitting in simulated CW noise spectroscopy experiments. The signal decay is simulated using an input $S_{in}(\omega) \approx 30\ \mathrm{Hz}^2/\omega$, and least-squares fitting is used to calculate the noise spectrum $S_0(\omega)$. At small pulse amplitudes (low Rabi frequencies), the exponential fitting returns inaccurate spectral information. The insets show the signal decays at the indicated pulse amplitudes, illustrating the non-exponential signal decay behaviour at low Ω. **b,c** Examples of the same procedure applied to different noise spectra, with b) $S_{in}(\omega) \approx 30\ \mathrm{Hz}^3/\omega^2$, and c) $S_{in}(\omega) \approx 3000\ \mathrm{Hz}^2/\omega$. **d** A signal decay taken at $\Omega = 16$ rad/s from the simulated experiment used in (a), illustrating non-exponential decay. The insets show $\mathcal{F}_2(\omega, \Omega, T)$ and $S(\omega)$ at two different time points.

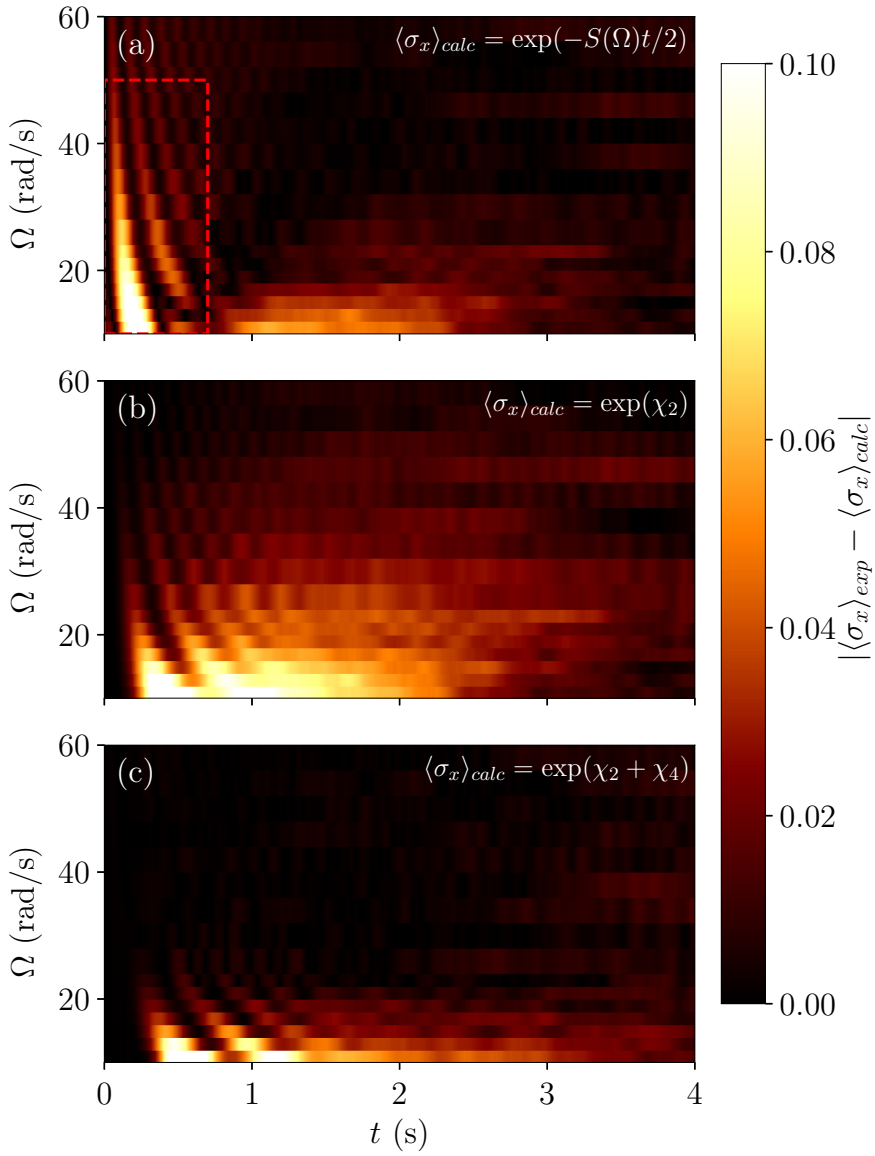

Figure 6.3: The error between the simulated "experimental" signal decays and theoretical decays calculated by standard (i.e. equation 6.19) and cumulant expansion methods. **a** Using the exponential form $\exp(-S(\Omega)t/2)$ results in large errors at short time scales ($t < 0.5$ s), i.e. the region indicated by the dashed box. **b** and **c**, using the cumulant expansion method reduces the error at short times. By using $\chi_2 + \chi_4$, the experimental decays are better matched at all times, down to low drive amplitudes ($\Omega \approx 20$ rad/s for the parameters chosen here).

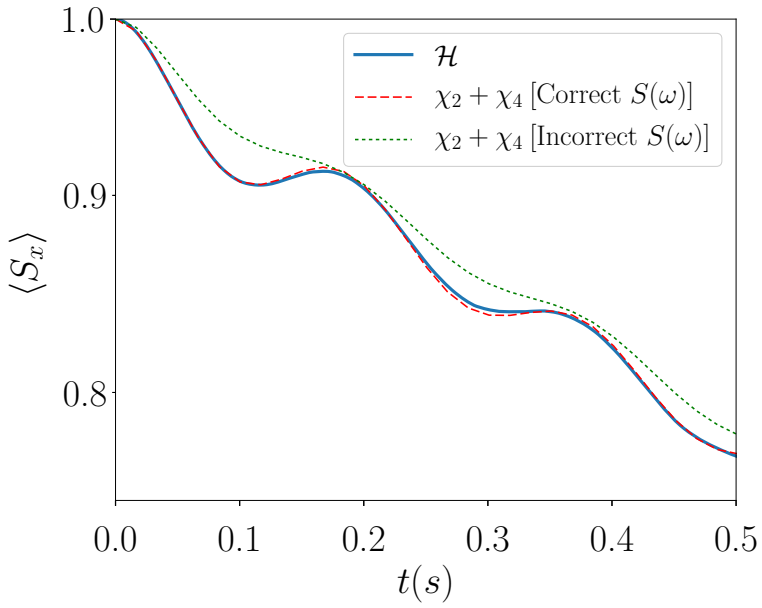

Figure 6.4: Comparison of the true signal decay, calculated by unitary time-evolution ($\mathcal{H}$), and decays calculated by the cumulant expansion up to χ_4, when $S(\omega)$ is varied in a region away from the driving amplitude. The correct $S(\omega) = 30\,\mathrm{Hz}^2/\omega$ (with a plateau as $\omega \to 0$) is used to calculate the red curve. For the green curve, all values of $S(\omega)$ for $\omega < 10\,\mathrm{rad/s}$ are reduced by half. The probe frequency is $\Omega = 32\,\mathrm{rad/s}$.

(e.g. $\Omega > 20\,\mathrm{rad/s}$ in figure 6.3) and extract information about $S(\omega)$ for $\omega < 20\,\mathrm{rad/s}$ from detailed fitting of the short-time behaviour.

To illustrate this broad spectral sensitivity, figure 6.4 shows the short-time behaviour of a $\chi_2 + \chi_4$ calculated signal decay for two different noise spectra. One spectrum is labelled 'correct', while the other represents an error in which $S(\omega)$ at low frequencies has been changed. Here, the error is introduced for $\omega < 10\,\mathrm{rad/s}$, while the drive amplitude $\Omega = 32\,\mathrm{rad/s}$. This shows that the decay is sensitive to variation in $S(\omega)$ at frequencies far below the probing frequency Ω.

6.4.1 Noise spectroscopy protocol

To take advantage of the accuracy of the $\chi_2 + \chi_4$ cumulant expansion for improving noise spectroscopy, a gradient ascent protocol was developed based on matching to the experi-

mental signal decay using a single chosen pulse amplitude, Ω_P. An initial estimate of the noise spectrum, $S_0(\omega)$, is obtained from the standard approach of fitting to exponential decays for a group of probe frequencies. Then, by accurately fitting a detailed signal decay at Ω_P using the cumulant expansion method, particularly in the short-time regime, the full noise spectrum can be determined.

The signal decay given by the cumulant expansion method is

$$\begin{aligned} s(t) &= \exp\left(\chi_2 + \chi_4\right) \\ &= \exp\left(-\frac{1}{\pi}\int_0^\infty d\omega S(\omega)\mathrm{Re}(\mathcal{F}_2(\omega,\Omega,t))\right. \\ &\left. + \frac{1}{2\pi^2}\int_0^\infty d\omega_1 \int_0^\infty d\omega_2 S(\omega_1)S(\omega_2)\tilde{\mathcal{F}}_4(\omega_1,\omega_2,\Omega,t)\right) \end{aligned}$$

Discretizing the above expression, and defining a fitness function as the root-mean square error between the experimentally measured decay, $\langle\sigma_x(t_j)\rangle$, and the calculated decay $s'(t_j)$ for a given $S'(\omega)$:

$$\Phi = 1 - \sqrt{\frac{1}{n}\sum_{j=1}^{n}\left(\langle\sigma_x(t_j)\rangle - s'(t_j)\right)^2} \tag{6.24}$$

Then calculate the gradient of the fitness function, $\frac{\partial\Phi}{\partial S'(\omega_i)}$, for any target frequency ω_i. The gradient is used to update the estimate of $S'(\omega)$ towards a closer matching of the experimental and calculated decays. The full protocol is:

1. To obtain an initial estimate, $S'_0(\omega)$, use exponential fits of decays over a range of Ω, and matching to $\langle\sigma_x(t)\rangle = \exp(-S'_0(\omega)t/2)$.

2. Select a drive amplitude, Ω_P, for detailed matching of the decay curve. Ω_P should be low enough to display non-exponential features at short times, but not so low that the $\chi_2+\chi_4$ calculation is inaccurate. Otherwise, the following steps will not converge to a high fitness function Φ.

3. Calculate the fitness function, Φ_0, for the decay at Ω_P using the initial estimate $S'_0(\omega)$.

4. While $\Phi_k < 1-\delta$ for some target threshold δ,

(a) Calculate $\frac{\partial \Phi}{\partial S(\omega_i)}$ for the current estimate $S'_k(\omega)$

(b) Update the estimate: for all ω_i, $S'_{k+1}(\omega_i) = S'_k(\omega_i) + \epsilon \frac{\partial \Phi}{\partial S(\omega_i)}$ for some fixed ϵ

(c) Calculate the updated fitness Φ_{k+1} and increment k.

To improve the speed of calculation/convergence, make use the knowledge that the simple exponential decay fitting is accurate when the signal decays are smooth exponentials, and only update $S'(\omega_i)$ for ω_i where that condition is not satisfied.

6.4.2 Demonstration of protocol

The cumulant expansion noise spectroscopy protocol described above was applied to the simulated experiments presented in section 6.3 corresponding to three different noise spectra. Figure 6.5 shows the result obtained using the simulation with the input noise $S_{input}(\omega) = 30\ \text{Hz}^2/\omega$ (with a plateau as $\omega \to 0$). The initial estimate, $S_0(\omega)$, uses the standard exponential fitting method at 11 pulse amplitudes in the range of 20-125 rad/s. The final estimate was obtained by detailed fitting to a single decay curve as described above. For comparison, this final step was done with three different choices for the parameters (Ω_P, T), where T is the total pulse duration. The final noise spectrum estimate $S_{final}(\omega)$ is a much better fit in the low frequency regime to the correct (input) spectrum.

Some artifacts are introduced in the form of oscillations in the intermediate frequency range ($\omega = 8 - 30$ rad/s). These artifacts have characteristic periods of order $\sim 2\pi/T$ and are a consequence of remaining error between the $\chi_2 + \chi_4$ decay and the true decay, such as contributions from χ_6 and higher terms. These oscillations are not a consequence of the gradient optimization and there is not a straightforward way to remove them. However, given that $S_0(\omega)$ is typically a smooth function, and that these oscillations are confined to a certain band of frequencies, smoothing or sliding window averaging can be used to suppress the oscillations in the final estimate. Alternately, they can be fully removed if the noise spectrum can be fit to a certain functional form, such as $1/f^k$.

Figure 6.6 shows the results of applying the cumulant expansion noise spectroscopy protocol to the same three simulated experiments shown in figure 6.2. Each plot shows the input, initial, and final $S(\omega)$ determined by fitting the signal decay at pulse amplitude Ω_P and total time T. To obtain the initial estimate, $S_0(\omega)$, figure 6.6a uses the same experiment set as figure 6.5, figure 6.6b uses experiments at 15 pulse amplitudes in the range 1-120 rad/s, and figure 6.6c uses 9 pulse amplitudes in the range 10-1250 rad/s.

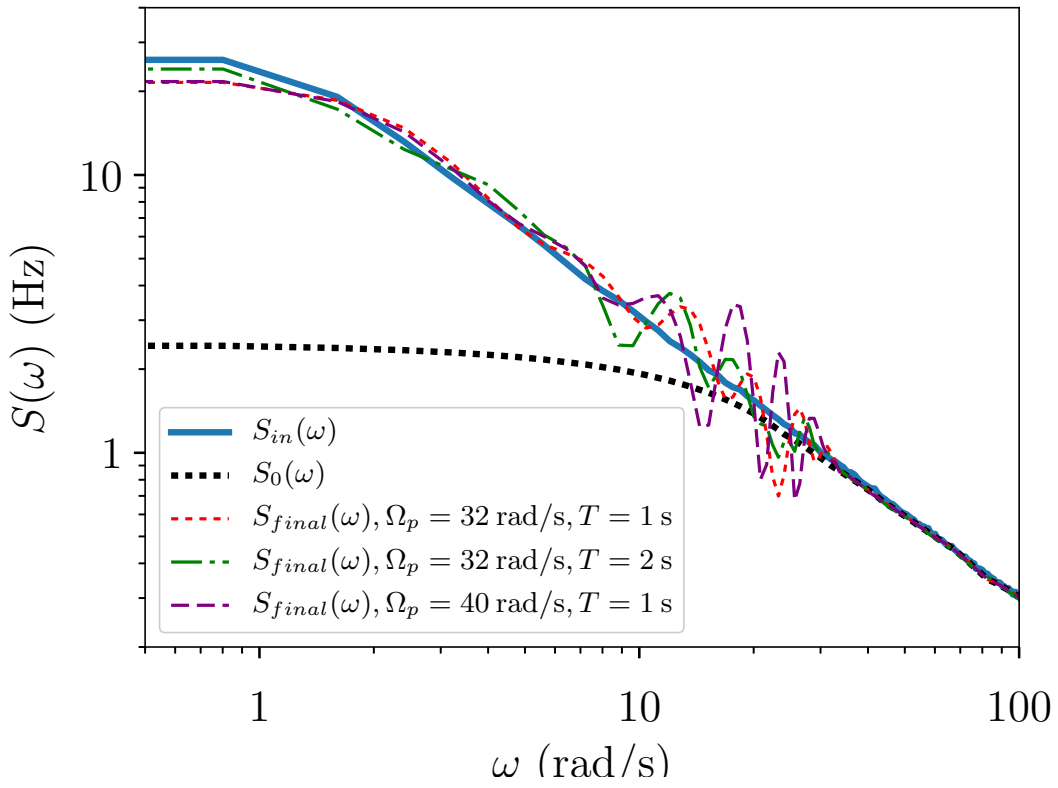

Figure 6.5: $S(\omega)$ estimates obtained from the cumulant expansion based noise spectroscopy protocol described in the main text. Results shown are for a simulated experiment with $S_{in} = 30\,\mathrm{Hz}^2/\omega$. The final spectrum estimates, $S_{final}(\omega)$, are shown for three different (Ω_P, T) conditions, where T is the total pulse duration. The initial estimate $S_0(\omega)$ is determined using the standard method of exponential fits to equation 6.19. The oscillations that appear in the range of 8-30 rad/s are artifacts (discussed in the text) and can be removed by fitting $S_{final}(\omega)$ to a functional form such as $1/f^k$.

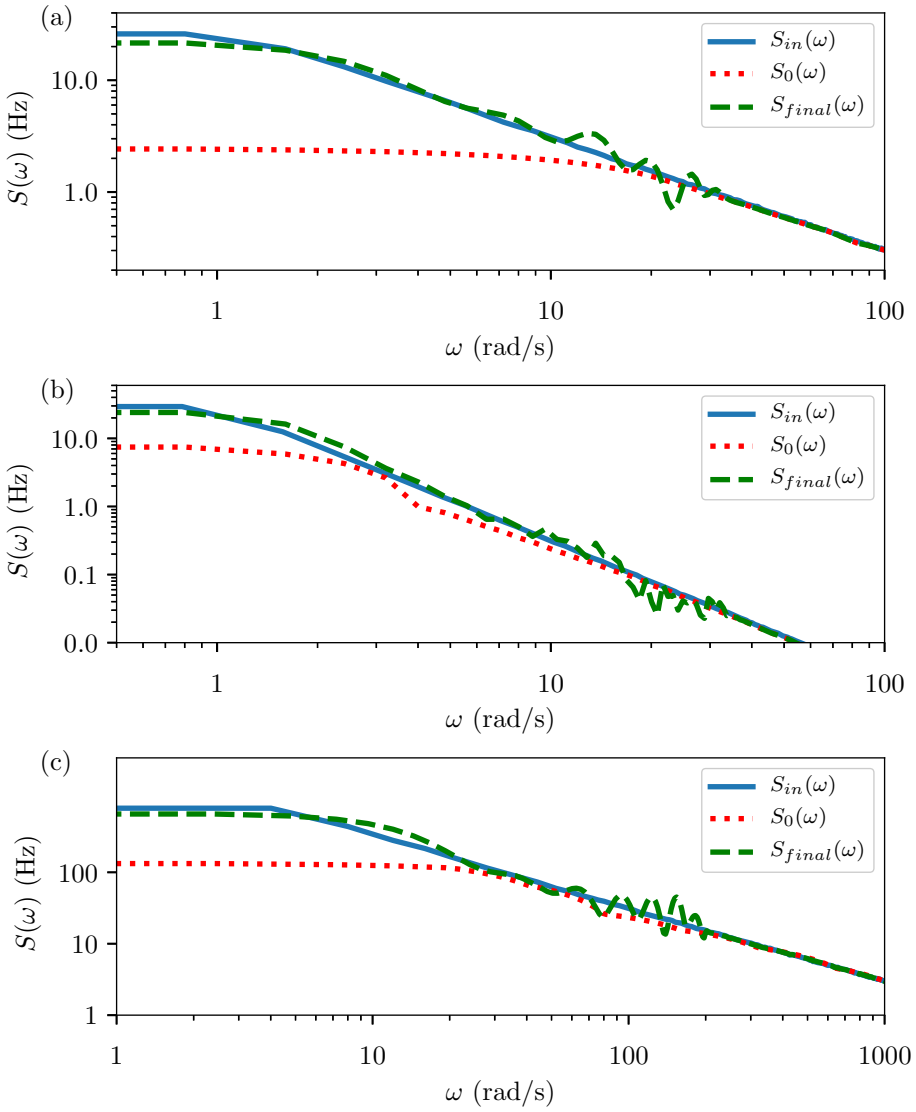

Figure 6.6: The result of applying the cumulant expansion noise spectroscopy protocol to three different noise spectra. The noise spectrum used to simulate each experiment is shown in blue ($S_{in}(\omega)$). The spectrum obtained from the standard exponential fitting ($S_0(\omega)$) is shown in red, and the result of the cumulant expansion protocol ($S_{final}(\omega)$) is shown in green. The input noise spectrum, pulse amplitude Ω_P, and total pulse duration are: (a) $S(\omega) = 30\ \mathrm{Hz}^2/\omega$, $\Omega_P = 35\ \mathrm{rad/s}$, $T = 1\ \mathrm{s}$, (b) $S(\omega) = 30\ \mathrm{Hz}^3/\omega^2$, $\Omega_P = 35\ \mathrm{rad/s}$, $T = 5\ \mathrm{s}$, (c) $S(\omega) = 3000\ \mathrm{Hz}^2/\omega$, $\Omega_P = 640\ \mathrm{rad/s}$, $T = 0.2\ \mathrm{s}$

6.5 Discussion

To summarize, this chapter examined the problem of spin evolution in the presence of single-axis phase noise during an experiment with CW excitation, with a goal towards improving the determination of an arbitrary noise spectral density. By retaining terms up to fourth order in the system-bath coupling, a cumulant expansion calculation can more accurately match coherence decay dynamics that exhibit non-exponential and oscillatory behaviour, and thereby extract more accurate spectral information, especially at low frequencies. A two-step protocol is proposed: (1) estimate $S(\omega)$ using the standard exponential fitting approach by probing over a set of frequencies (low-resolution signal decay experiments); (2) refine $S(\omega)$ based on fitting a single, high-resolution signal decay experiment using the fourth order cumulant expansion calculation. Since this second step consists of probing at a single frequency, it is efficient in terms of experimental resources. For the cases of $1/f$ and $1/f^2$ noise (with low frequency cutoff plateau), this protocol allows for accurate determination of $S(\omega)$ to zero frequency, i.e. the low frequency regime where standard CW and pulsed noise spectroscopy fail. While the examples given were noise spectra of the form $1/f^\alpha$, the theoretical analysis and protocol are applicable to arbitrary spectra, and future work should test this applicability in simulations and real experiments. In addition, inhomogeneous broadening is typical in physical spin systems, and should also be included. This can be expressed as an additional Hamiltonian component $H(t) = \beta\sigma_z$, where β is a static random variable. Thus, inhomogeneous broadening yields a peak in $S(\omega)$ at $\omega = 0$, which should enhance the oscillations in signal decay at short timescales for low probing frequencies. The protocol developed in this chapter should therefore reveal such broadening. Additional work could also extend the cumulant expansion noise spectroscopy protocol to include multi-axis noise and/or higher order cumulants (χ_6) for more general applications.

Chapter 7

Conclusion and Outlook

The primary focus of this thesis was the suspended carbon nanotube as a nanoelectromechanical system, with an eye towards employing such devices for magnetic force detection of molecular nanomagnets [1]. While the experimental integration of such nanomagnets has not been realized, the fabrication of long, high quality single wall CNT devices with integrated ferromagnets was achieved. The future operation of these integrated devices will require fast CNT mechanical readout, at low temperatures ($< 2\,\mathrm{K}$ for many nanomagnets)

The fabrication processes developed in chapter 3 provides reproducible clean CNT devices. Through tuning of the CVD growth conditions, single suspended small-diameter low-defect CNTs were realized with comparatively high yields. These CNTs can be either measured as grown, or transferred to separate substrates. By separating the CVD growth and contact fabrication, the integration of CVD-incompatible ferromagnetic materials was realized.

In chapter 4, fast electrical readout of the mechanical motion of a suspended CNT resonator was demonstrated using a proximate HBT circuit operated as a linear AC current amplifier. A Coulomb rectification measurement made it possible to explore the transition from the linear to the strongly non-linear regimes. The transient mechanical response was measured under pulsed driving, where we observed a fast turn-on response in the non-linear regime. The resonator behaviour is well described by a harmonic oscillator by including Duffing and non-linear damping terms. For the circuit and CNT device measured in chapter 4, a response time $\sim 10\ \mu$s to an instantaneously applied force could be obtained using non-linear response under strong driving, making it a suitable readout mechanism for nanomagnet sensing. Future work could investigate the use of direct HBT amplification with no resistor network, which could allow for sub-microsecond readout times at μW heat

dissipation. This heat load is compatible with direct integration onto the mixing chamber stage of a dilution refrigerator, making HBT amplification a promising path for not only fast, low-temperature sensing of CNTs, but also other electrical detection such as charge sensing in quantum dots and quantum point contacts.

In low-temperature operation of CNT NEMS, both in this thesis and literature, it is common to operate devices in Coulomb blockade conduction regimes, due to large readout signals created by sharp non-linear conduction peaks. In chapter 5, I reported on self-driven oscillations observed in this regime, and presented a model to understand the conditions which create these states. In summary, high quality factor CNT oscillators at low temperatures can support self-driven oscillations in the presence of strongly energy-dependent tunneling to the contacts. This could, for example, become increasingly prevalent in devices in which suspended CNT sections are coupled to readout quantum dots, a device geometry previously discussed in literature [114, 115]. These in-diamond self-driven oscillations are large amplitude self-sustained oscillations, which would limit the use of these devices for nominal operation as CNT mechanical sensors. However these oscillations may exhibit narrower linewidths than the intrinsic resonator linewidths [87], and the electromechanical coupling can potentially result in active cooling of the mechanical state.[73], creating some potential for harnessing the self-driven states.

Chapter 6 examined noise spectroscopy of spin qubits in the presence of dominant single-axis phase noise, under CW excitation. Using a cumulant expansion analysis of the system, the spin decay evolution could be accurately calculated for arbitrary noise power spectral densities. Based on this analysis, an experimental protocol was proposed that first uses low resolution experiments and standard exponential fitting to get an estimate of $S(\omega)$, then refines this estimate using optimization over a single high resolution signal decay experiment. This protocol and the associated analysis allow accurate CW noise spectroscopy over a wider set of noisy systems than prior CW noise analysis permitted. This may, for example, be useful in understanding the evolution of continually driven nanomagnets in the CNT-nanomagnet systems proposed in this thesis. One of the intriguing aspects of nanomagnet sensing with the carbon nanotubes is the ability to see the nanomagnet evolution at the individual scale, away from bulk physics. Measuring the remaining noise affecting the nanomagnet in this scenario, and comparing it to noisy evolution in bulk experiments would further the understanding of molecular nanomagnet systems.

The devices described in section 3.4 and measured in chapter 5 are suitable for the magnetic force sensing experiments proposed in reference [1]. Using the measurement technique in chapter 4 would permit single-shot readout of the magnetic states of many molecular nanomagnets on timescales comparable to their spin relaxation and/or dephasing times [65, 66]. After identifying a suitable molecular nanomagnet, deposition by either

sublimation or solution-based dispersion can be performed. I tested in-situ sublimation of nanomagnets in the 1.4 K pumped He_4 cryostat (see Appendix F for details), however the nanomagnets for which this was attempted ($Dy(hfac)_3(bipy)$ and $Tb(hfac)_3(4\text{-benzylpyridine})_2$) did not survive the sublimation-to-CNT process, with the only material deposited on the CNT having no magnetic signature. Solution based dispersion using critical point drying has been previously used to deposit nanomagnets on CNTs [53], however the in-solvent processing of the CNTs can damage the suspended devices, particularly for the stamped fabrication devices which have smaller mechanical contact regions. Development of a robust molecular nanomagnet with ligand structures suitable for both sublimation and CNT-adhesion would allow for the current generation of CNT devices to realize the molecular nanomagnet force sensing experiments.

References

[1] K. Willick, C. Haapamaki, and J. Baugh, "Sensitive magnetic force detection with a carbon nanotube resonator," *Journal of Applied Physics*, vol. 115, p. 114501, mar 2014.

[2] S. Kotru, J. Zhong, A. Highsmith, and J. E. Jackson, "Design and fabrication of a meso-scale gyroscope," in *2008 IEEE Workshop on Microelectronics and Electron Devices*, pp. 5–8, IEEE, 2008.

[3] A. Górecka-Drzazga, "Miniature and mems-type vacuum sensors and pumps," *Vacuum*, vol. 83, no. 12, pp. 1419–1426, 2009.

[4] N. J. Conway, Z. J. Traina, and S.-G. Kim, "A strain amplifying piezoelectric mems actuator," *Journal of Micromechanics and Microengineering*, vol. 17, no. 4, p. 781, 2007.

[5] M. B. Gerdroodbary, A. Anazadehsayed, A. Hassanvand, and R. Moradi, "Calibration of low-pressure mems gas sensor for detection of hydrogen gas," *International Journal of Hydrogen Energy*, vol. 43, no. 11, pp. 5770–5782, 2018.

[6] D. Dudley, W. M. Duncan, and J. Slaughter, "Emerging digital micromirror device (dmd) applications," in *MOEMS display and imaging systems*, vol. 4985, pp. 14–25, International Society for Optics and Photonics, 2003.

[7] T. George, "Overview of mems/nems technology development for space applications at nasa/jpl," in *Smart Sensors, Actuators, and MEMS*, vol. 5116, pp. 136–148, International Society for Optics and Photonics, 2003.

[8] A. N. Cleland and M. L. Roukes, "A nanometre-scale mechanical electrometer," *Nature*, vol. 392, no. 6672, pp. 160–162, 1998.

[9] D. Rugar, R. Budakian, H. J. Mamin, and B. W. Chui, "Single spin detection by magnetic resonance force microscopy.," *Nature*, vol. 430, pp. 329–332, July 2004.

[10] A. D. O'Connell, M. Hofheinz, M. Ansmann, R. C. Bialczak, M. Lenander, E. Lucero, M. Neeley, D. Sank, H. Wang, M. Weides, *et al.*, "Quantum ground state and single-phonon control of a mechanical resonator," *Nature*, vol. 464, no. 7289, pp. 697–703, 2010.

[11] M. Mohammad, S. Dew, S. Evoy, and M. Stepanova, "Fabrication of sub-10 nm silicon carbon nitride resonators using a hydrogen silsesquioxane mask patterned by electron beam lithography," *Microelectronic engineering*, vol. 88, no. 8, pp. 2338–2341, 2011.

[12] V. Sazonova, Y. Yaish, H. Ustünel, D. Roundy, T. a. Arias, and P. L. McEuen, "A tunable carbon nanotube electromechanical oscillator.," *Nature*, vol. 431, pp. 284–7, Sept. 2004.

[13] A. K. Huttel, G. A. Steele, B. Witkamp, M. Poot, L. P. Kouwenhoven, and H. S. J. van der Zant, "Carbon nanotubes as ultrahigh quality factor mechanical resonators," *Nano Lett.*, vol. 9, no. 7, pp. 2547–2552, 2009.

[14] G. A. Steele, A. K. Hüttel, B. Witkamp, M. Poot, H. B. Meerwaldt, L. P. Kouwenhoven, and H. S. J. van der Zant, "Strong coupling between single-electron tunneling and nanomechanical motion," *Science*, vol. 325, no. 5944, pp. 1103–1107, 2009.

[15] A. Eichler, M. del Álamo Ruiz, J. A. Plaza, and A. Bachtold, "Strong coupling between mechanical modes in a nanotube resonator," *Phys. Rev. Lett.*, vol. 109, p. 025503, Jul 2012.

[16] A. Eichler, J. Chaste, J. Moser, and A. Bachtold, "Parametric amplification and self-oscillation in a nanotube mechanical resonator," *Nano letters*, vol. 11, no. 7, pp. 2699–2703, 2011.

[17] B. Lassagne, Y. Tarakanov, J. Kinaret, D. Garcia-Sanchez, D. Garcia-Sanchez, and A. Bachtold, "Coupling mechanics to charge transport in carbon nanotube mechanical resonators.," *Science*, vol. 325, pp. 1107–10, Aug. 2009.

[18] A. K. Huttel, H. B. Meerwaldt, G. A. Steele, M. Poot, B. Witkamp, L. P. Kouwenhoven, and H. S. J. van der Zant, "Single electron tunnelling through high-q single-wall carbon nanotube nems resonators," *Phys. Status Solidi B*, vol. 247, no. 11-12, pp. 2974–2979, 2010.

[19] H. B. Meerwaldt, G. Labadze, B. H. Schneider, A. Taspinar, Y. M. Blanter, H. S. J. van der Zant, and G. A. Steele, "Probing the charge of a quantum dot with a nanomechanical resonator," *Phys. Rev. B*, vol. 86, p. 115454, Sept. 2012.

[20] J. Chaste, A. Eichler, J. Moser, G. Ceballos, R. Rurali, and a. Bachtold, "A nanomechanical mass sensor with yoctogram resolution.," *Nat. Nanotechnol.*, vol. 7, pp. 301–4, May 2012.

[21] J. Moser, J. Güttinger, A. Eichler, M. J. Esplandiu, D. E. Liu, M. I. Dykman, and A. Bachtold, "Ultrasensitive force detection with a nanotube mechanical resonator," *Nat. Nanotechnol.*, vol. 8, pp. 493–496, July 2013.

[22] E. A. Laird, F. Pei, W. Tang, G. A. Steele, and L. P. Kouwenhoven, "A high quality factor carbon nanotube mechanical resonator at 39 ghz," *Nano letters*, vol. 12, no. 1, pp. 193–197, 2012.

[23] J. O. Island, V. Tayari, A. C. McRae, and A. R. Champagne, "Few-Hundred GHz Carbon Nanotube Nanoelectromechanical Systems (NEMS)," *Nano Lett.*, vol. 12, pp. 4564–4569, Sept. 2012.

[24] J. Moser, A. Eichler, J. Güttinger, M. I. Dykman, and A. Bachtold, "Nanotube mechanical resonators with quality factors of up to 5 million," *Nature nanotechnology*, vol. 9, no. 12, p. 1007, 2014.

[25] J. Schwender, I. Tsioutsios, A. Tavernarakis, Q. Dong, Y. Jin, U. Staufer, and A. Bachtold, "Improving the read-out of the resonance frequency of nanotube mechanical resonators," *Applied Physics Letters*, vol. 113, no. 6, p. 063104, 2018.

[26] A. W. Barnard, M. Zhang, G. S. Wiederhecker, M. Lipson, and P. L. McEuen, "Real-time vibrations of a carbon nanotube," *Nature*, vol. 566, no. 7742, p. 89, 2019.

[27] W. Wernsdorfer, "Molecular nanomagnets: towards molecular spintronics," *Int. J. Nanotechnol.*, vol. 7, no. 4/5/6/7/8, pp. 497–522, 2010.

[28] B. Lassagne, D. Garcia-Sanchez, A. Aguasca, and A. Bachtold, "Ultrasensitive mass sensing with a nanotube electromechanical resonator," *Nano Lett.*, vol. 8, no. 11, pp. 3735–3738, 2008.

[29] M. Ganzhorn, S. Klyatskaya, M. Ruben, and W. Wernsdorfer, "Carbon nanotube nanoelectromechanical systems as magnetometers for single-molecule magnets.," *ACS nano*, vol. 7, pp. 6225–36, July 2013.

[30] H.-S. P. Wong and D. Akinwande, *Carbon Nanotube and Graphene Device Physics*. Cambridge University Press, 2011.

[31] W. Izumida, K. Sato, and R. Saito, "Spin–Orbit Interaction in Single Wall Carbon Nanotubes: Symmetry Adapted Tight-Binding Calculation and Effective Model Analysis," *J. Phys. Soc. Japan*, vol. 78, p. 074707, July 2009.

[32] E. A. Laird, F. Kuemmeth, G. A. Steele, K. Grove-Rasmussen, J. Nygård, K. Flensberg, and L. P. Kouwenhoven, "Quantum transport in carbon nanotubes," *Reviews of Modern Physics*, vol. 87, no. 3, p. 703, 2015.

[33] M. Huang, Y. Wu, B. Chandra, H. Yan, Y. Shan, T. Heinz, and J. Hone, "Direct Measurement of Strain-Induced Changes in the Band Structure of Carbon Nanotubes," *Phys. Rev. Lett.*, vol. 100, p. 136803, Apr. 2008.

[34] M. J. Biercuk, S. Ilani, C. M. Marcus, and P. L. Mceuen, "Electrical Transport in Single-Wall Carbon Nanotubes," in *Carbon Nanotub. Adv. Top. Synth. Struct. Prop. Appl.*, vol. 493, pp. 455–493, Springer Berlin Heidelberg, 2008.

[35] L. P. Kouwenhoven, C. M. Marcus, P. L. Mceuen, S. Tarucha, and M. Robert, "Electron transport in quantum dots.," in *Proc. NATO Adv. Study Inst. Mesoscopic Electron Transp.*, pp. 105–214, Kluwer Series E345, 1997.

[36] R. Hanson, J. R. Petta, S. Tarucha, and L. M. K. Vandersypen, "Spins in few-electron quantum dots," *Rev. Mod. Phys.*, vol. 79, pp. 1217–1265, Oct. 2007.

[37] D. H. Cobden and J. Nygård, "Shell filling in closed single-wall carbon nanotube quantum dots," *Physical Review Letters*, vol. 89, no. 4, p. 046803, 2002.

[38] D. J. Griffiths, "Introduction to electrodynamics," 2005.

[39] H. B. Meerwaldt, S. R. Johnston, H. S. J. van der Zant, and G. A. Steele, "Submicrosecond-timescale readout of carbon nanotube mechanical motion," *Applied Physics Letters*, vol. 103, no. 5, p. 053121, 2013.

[40] B. H. Schneider, V. Singh, W. J. Venstra, H. B. Meerwaldt, and G. A. Steele, "Observation of decoherence in a carbon nanotube mechanical resonator," *Nature Communications*, vol. 5, p. 5819, December 2014.

[41] Y. Wen, N. Ares, T. Pei, G. Briggs, and E. A. Laird, "Measuring carbon nanotube vibrations using a single-electron transistor as a fast linear amplifier," *Applied Physics Letters*, vol. 113, no. 15, p. 153101, 2018.

[42] V. Sazonova, *A tunable carbon nanotube resonator*. Phd, Cornell University, 2006.

[43] V. Gouttenoire, T. Barois, S. Perisanu, J.-L. Leclercq, S. T. Purcell, P. Vincent, and A. Ayari, "Digital and FM Demodulation of a Doubly Clamped Single-Walled Carbon-Nanotube Oscillator: Towards a Nanotube Cell Phone," *Small*, vol. 6, no. 9, pp. 1060–1065, 2010.

[44] A. Eichler, J. Moser, J. Chaste, M. Zdrojek, I. Wilson-Rae, and A. Bachtold, "Nonlinear damping in mechanical resonators made from carbon nanotubes and graphene," *Nat. Nanotechnol.*, vol. 6, pp. 339–342, June 2011.

[45] M. Poot, *Mechanical systems at the nanoscale*. Phd, Technische Universiteit Delft, 2009.

[46] J.-P. Salvetat, J.-M. Bonard, N. H. Thomson, A. J. Kulik, L. Forro, W. Benoit, and L. Zuppiroli, "Mechanical Properties of Carbon Nanotubes," *Appl. Phys. A Mater. Sci. Process.*, vol. 69, pp. 255–260, 1999.

[47] A. Krishnan, E. Dujardin, T. Ebbesen, P. Yianilos, and M. Treacy, "Young's modulus of single-walled nanotubes," *Phys. Rev. B*, vol. 58, pp. 14013–14019, Nov. 1998.

[48] S. V. Rotkin and S. Subramoney, *Applied physics of carbon nanotubes: fundamentals of theory, optics and transport devices*. Springer Science & Business Media, 2006.

[49] H. B. Meerwaldt, *Carbon nanotubes as electromechanical resonators: Single-electron tunneling, non-linearity, and high-bandwidth readout*. Phd, TU Delft, 2013.

[50] R. Kubo, "The fluctuation-dissipation theorem," *Reports on progress in physics*, vol. 29, no. 1, p. 255, 1966.

[51] B. Witkamp, M. Poot, and H. S. J. van der Zant, "Bending-mode vibration of a suspended nanotube resonator.," *Nano Lett.*, vol. 6, pp. 2904–8, Dec. 2006.

[52] M. Poot and H. S. van der Zant, "Mechanical systems in the quantum regime," *Physics Reports*, vol. 511, no. 5, pp. 273–335, 2012.

[53] M. Ganzhorn, *Coupling Magnetism and Mechanics at a molecular scale*. Phd, Universite de Gernoble, 2012.

[54] S. Diez, "The next generation of maskless lithography," in *Emerging Digital Micromirror Device Based Systems and Applications VIII*, vol. 9761, p. 976102, International Society for Optics and Photonics, 2016.

[55] S. Franssila, *Introduction to Micro Fabrication*. Wiley, 2004.

[56] S. Mahieu, K. Van Aeken, and D. Depla, "Transport of sputtered particles through the gas phase," in *Reactive Sputter Deposition*, pp. 199–227, Springer, 2008.

[57] J. Sengupta, "Carbon nanotube fabrication at industrial scale: Opportunities and challenges," in *Handbook of Nanomaterials for Industrial Applications*, pp. 172–194, Elsevier, 2018.

[58] V. Ngoc-Nguyen, *Synthesis and electronic transport of ultraclean single wall carbon nanotubes*. Phd, Institut Neel, 2012.

[59] C. P. Deck and K. Vecchio, "Prediction of carbon nanotube growth success by the analysis of carbon–catalyst binary phase diagrams," *Carbon N. Y.*, vol. 44, pp. 267–275, Feb. 2006.

[60] M. Kumar and Y. Ando, "Chemical Vapor Deposition of Carbon Nanotubes: A Review on Growth Mechanism and Mass Production," *J. Nanosci. Nanotechnol.*, vol. 10, pp. 3739–3758, June 2010.

[61] M. S. Dresselhaus, G. Dresselhaus, R. Saito, and A. Jorio, "Raman spectroscopy of carbon nanotubes," *Physics reports*, vol. 409, no. 2, pp. 47–99, 2005.

[62] C. Hierold, *Carbon Nanotube Devices*. Wiley-VCH Verlag GMBH Co., 2008.

[63] M. Dresselhaus, G. Dresselhaus, A. Jorio, A. Souza Filho, and R. Saito, "Raman spectroscopy on isolated single wall carbon nanotubes," *Carbon*, vol. 40, no. 12, pp. 2043–2061, 2002.

[64] J. Waissman, M. Honig, S. Pecker, A. Benyamini, A. Hamo, and S. Ilani, "Realization of pristine and locally tunable one-dimensional electron systems in carbon nanotubes," *Nature nanotechnology*, vol. 8, no. 8, p. 569, 2013.

[65] A. Ardavan, O. Rival, J. J. L. Morton, S. J. Blundell, A. M. Tyryshkin, G. A. Timco, and R. E. P. Winpenny, "Will Spin-Relaxation Times in Molecular Magnets Permit Quantum Information Processing?," *Phys. Rev. Lett.*, vol. 98, p. 057201, Jan. 2007.

[66] J. M. Zadrozny, J. Niklas, O. G. Poluektov, and D. E. Freedman, "Millisecond Coherence Time in a Tunable Molecular Electronic Spin Qubit," *ACS Central Science*, vol. 1, no. 9, pp. 488–492, 2015.

[67] J. C. Bardin, *Silicon-germanium heterojunction bipolar transistors for extremely low-noise applications*. PhD thesis, California Institute of Technology, 2009.

[68] M. J. Curry, T. D. England, N. C. Bishop, G. Ten-Eyck, J. R. Wendt, T. Pluym, M. P. Lilly, S. M. Carr, and M. S. Carroll, "Cryogenic preamplification of a single-electron-transistor using a silicon-germanium heterojunction-bipolar-transistor," *Applied Physics Letters*, vol. 106, no. 20, p. 203505, 2015.

[69] D. Davidović, H. Ying, J. Dark, B. Wier, L. Ge, N. Lourenco, A. Omprakash, M. Mourigal, and J. Cressler, "Tunneling, current gain, and transconductance in silicon-germanium heterojunction bipolar transistors operating at millikelvin temperatures," *Physical Review Applied*, vol. 8, no. 2, p. 024015, 2017.

[70] R. J. Monroe and S. W. Shaw, "On the transient response of forced nonlinear oscillators," *Nonlinear Dynamics*, vol. 67, no. 4, pp. 2609–2619, 2012.

[71] D. R. Schmid, P. L. Stiller, C. Strunk, and A. K. Hüttel, "Magnetic damping of a carbon nanotube nano-electromechanical resonator," *New Journal of Physics*, vol. 14, no. 8, p. 083024, 2012.

[72] D. R. Schmid, P. L. Stiller, C. Strunk, and A. K. Hüttel, "Liquid-induced damping of mechanical feedback effects in single electron tunneling through a suspended carbon nanotube," *Applied Physics Letters*, vol. 107, no. 12, p. 123110, 2015.

[73] C. Urgell, W. Yang, S. De Bonis, C. Samanta, M. Esplandiu, Q. Dong, Y. Jin, and A. Bachtold, "Cooling and self-oscillation in a nanotube electromechanical resonator," *Nature Physics*, pp. 1–6, 2019.

[74] Y. Wen, N. Ares, F. Schupp, T. Pei, G. Briggs, and E. Laird, "A coherent nanomechanical oscillator driven by single-electron tunnelling," *Nature physics*, vol. 16, no. 1, pp. 75–82, 2020.

[75] P. Stokes and S. I. Khondaker, "Evaluating defects in solution-processed carbon nanotube devices via low-temperature transport spectroscopy," *ACS nano*, vol. 4, no. 5, pp. 2659–2666, 2010.

[76] P. Jarillo-Herrero, J. Kong, H. Van der Zant, C. Dekker, L. Kouwenhoven, and S. De Franceschi, "Electronic transport spectroscopy of carbon nanotubes in a magnetic field," *Physical review letters*, vol. 94, no. 15, p. 156802, 2005.

[77] H. Ajiki and T. Ando, "Electronic states of carbon nanotubes," *Journal of the Physical Society of Japan*, vol. 62, no. 4, pp. 1255–1266, 1993.

[78] O. Usmani, Y. M. Blanter, and Y. V. Nazarov, "Strong feedback and current noise in nanoelectromechanical systems," *Physical Review B*, vol. 75, no. 19, p. 195312, 2007.

[79] M. Brink, *Imaging Single-Electron Charging in Nanostructures by Low-Temperature Scanning Force Microscopy*. PhD thesis, Cornell University, 2006.

[80] A. Armour, M. Blencowe, and Y. Zhang, "Classical dynamics of a nanomechanical resonator coupled to a single-electron transistor," *Physical Review B*, vol. 69, no. 12, p. 125313, 2004.

[81] Y. M. Blanter, O. Usmani, and Y. V. Nazarov, "Single-electron tunneling with strong mechanical feedback," *Physical review letters*, vol. 93, no. 13, p. 136802, 2004.

[82] A. Korotkov and Y. V. Nazarov, "Single-electron tunneling coexisting with the barrier suppression," *Physica B: Condensed Matter*, vol. 173, no. 3, pp. 217–222, 1991.

[83] D. Wang, B. Perkins, A. Yin, A. Zaslavsky, J. Xu, R. Beresford, and G. Snider, "Carbon nanotube gated lateral resonant tunneling field-effect transistors," *Applied Physics Letters*, vol. 87, no. 15, p. 152102, 2005.

[84] D. J. Perello, S. ChuLim, S. J. Chae, I. Lee, M. J. Kim, Y. H. Lee, and M. Yun, "Anomalous schottky barriers and contact band-to-band tunneling in carbon nanotube transistors," *ACS nano*, vol. 4, no. 6, pp. 3103–3108, 2010.

[85] J. Knoch and J. Appenzeller, "Tunneling phenomena in carbon nanotube field-effect transistors," *physica status solidi (a)*, vol. 205, no. 4, pp. 679–694, 2008.

[86] P. Gehring, J. K. Sowa, J. Cremers, Q. Wu, H. Sadeghi, Y. Sheng, J. H. Warner, C. J. Lambert, G. A. D. Briggs, and J. A. Mol, "Distinguishing lead and molecule states in graphene-based single-electron transistors," *ACS nano*, vol. 11, no. 6, pp. 5325–5331, 2017.

[87] S. D. Bennett and A. A. Clerk, "Laser-like instabilities in quantum nanoelectromechanical systems," *Phys. Rev. B*, vol. 74, p. 201301, Nov 2006.

[88] X. Feng, C. White, A. Hajimiri, and M. L. Roukes, "A self-sustaining ultrahigh-frequency nanoelectromechanical oscillator," *Nature nanotechnology*, vol. 3, no. 6, pp. 342–346, 2008.

[89] K. Khodjasteh and L. Viola, "Dynamically error-corrected gates for universal quantum computation," *Phys. Rev. Lett.*, vol. 102, p. 080501, Feb 2009.

[90] T. Yuge, S. Sasaki, and Y. Hirayama, "Measurement of the noise spectrum using a multiple-pulse sequence," *Phys. Rev. Lett.*, vol. 107, p. 170504, 2011.

[91] G. A. Álvarez and D. Suter, "Measuring the spectrum of colored noise by dynamical decoupling," *Phys. Rev. Lett.*, vol. 107, p. 230501, 2011.

[92] I. Almog, Y. Sagi, G. Gordon, G. Bensky, G. Kurizki, and N. Davidson, "Direct measurement of the system environment coupling as a tool for understanding decoherence and dynamical decoupling," *J. Phys. B: At. Mol. Opt. Phys.*, vol. 44, no. 15, p. 154006, 2011.

[93] N. Bar-Gill, L. Pham, C. Belthangady, D. L. Sage, P. Cappellaro, J. Maze, M. Lukin, A. Yacoby, and R. Walsworth, "Suppression of spin-bath dynamics for improved coherence of multi-spin-qubit systems," *Nat. Commun.*, vol. 3:858, 2012.

[94] G. Ithier, E. Collin, P. Joyez, P. J. Meeson, D. Vion, D. Esteve, F. Chiarello, A. Shnirman, Y. Makhlin, J. Schriefl, and G. Schön, "Decoherence in a superconducting quantum bit circuit," *Phys. Rev. B*, vol. 72, p. 134519, Oct 2005.

[95] J. Bylander, S. Gustavsson, F. Yan, F. Yoshihara, K. Harrabi, G. Fitch, D. G. Cory, Y. Nakamura, J.-S. Tsai, and W. D. Oliver, "Noise spectroscopy through dynamical decoupling with a superconducting flux qubit," *Nat Phys*, vol. 7, no. 7, pp. 565–70, 2011.

[96] F. Yan, S. Gustavsson, J. Bylander, X. Jin, F. Yoshihara, D. G. Cory, Y. Nakamura, T. P. Orlando, and W. D. Oliver, "Rotating-frame relaxation as a noise spectrum analyser of a superconducting qubit undergoing driven evolution," *Nat. Commun.*, vol. 4:2337, 2013.

[97] D. H. Slichter, R. Vijay, S. J. Weber, S. Boutin, M. Boissonneault, J. M. Gambetta, A. Blais, and I. Siddiqi, "Measurement-induced qubit state mixing in circuit qed from up-converted dephasing noise," *Phys. Rev. Lett.*, vol. 109, p. 153601, Oct 2012.

[98] P. Szańkowski, G. Ramon, J. Krzywda, D. Kwiatkowski, and . Cywiński, "Environmental noise spectroscopy with qubits subjected to dynamical decoupling," *Journal of Physics: Condensed Matter*, vol. 29, no. 33, p. 333001, 2017.

[99] T. Green, H. Uys, and M. J. Biercuk, "High-order noise filtering in nontrivial quantum logic gates," *Phys. Rev. Lett.*, vol. 109, p. 020501, Jul 2012.

[100] T. J. Green, J. Sastrawan, H. Uys, and M. J. Biercuk, "Arbitrary quantum control of qubits in the presence of universal noise," *New J. Phys.*, vol. 15, p. 095004, 2013.

[101] A. G. Kofman and G. Kurizki, "Unified theory of dynamically suppressed qubit decoherence in thermal baths," *Phys. Rev. Lett.*, vol. 93, p. 130406, Sep 2004.

[102] A. Ajoy, G. A. Álvarez, and D. Suter, "Optimal pulse spacing for dynamical decoupling in the presence of a purely dephasing spin bath," *Phys. Rev. A*, vol. 83, p. 032303, Mar 2011.

[103] M. J. Biercuk, A. C. Doherty, and H. Uys, "Dynamical decoupling sequence construction as a filter-design problem," *J. Phys. B: At. Mol. Opt. Phys*, vol. 44, no. 15, p. 154002, 2011.

[104] C. P. Slichter and D. Ailion, "Low-field relaxation and the study of ultraslow atomic motions by magnetic resonance," *Phys. Rev.*, vol. 135, p. A1099, Aug 1964.

[105] D. C. Ailion and C. P. Slichter, "Observation of ultra-slow translational diffusion in metallic lithium by magnetic resonance," *Phys. Rev.*, vol. 137, p. A235, Jan 1965.

[106] D. C. Ailion, "Nmr and ultraslow motions," *Adv. Mag. Res.*, vol. 5, pp. 177–227, 1971.

[107] D. C. Look and I. J. Lowe, "Nuclear magnetic dipole—dipole relaxation along the static and rotating magnetic fields: Application to gypsum," *The Journal of Chemical Physics*, vol. 44, no. 8, p. 2995, 1966.

[108] E. Geva, R. Kosloff, and J. L. Skinner, "On the relaxation of a two-level system driven by a strong electromagnetic field," *J. Chem. Phys*, vol. 102, p. 8541, Jun 1995.

[109] K. Blum, *Density Matrix Theory and Application*. Physics of Atoms and Molecules, Springer US, 1996.

[110] R. Kubo, "Generalized cumulant expansion method," *J. Phys. Soc. Jap.*, vol. 17, no. 7, pp. 1100–1120, 1962.

[111] R. Kubo, "Stochastic liouville equations," *J. Math. Physics*, vol. 4, no. 2, p. 174, 1963.

[112] L. Isserlis, "On a formula for the product-moment coefficient of any order of a normal frequency distribution in any number of variables," *Biometrika*, vol. 12, no. 1/2, pp. 134–139, 1918.

[113] M. Shinozuka and G. Deodatis, "Simulation of stochastic processes by spectral representation," *Applied Mechanics Reviews*, vol. 44, no. 4, pp. 191–204, 1991.

[114] C. Ohm, C. Stampfer, J. Splettstoesser, and M. R. Wegewijs, "Readout of carbon nanotube vibrations based on spin-phonon coupling," *Applied Physics Letters*, vol. 100, no. 14, p. 143103, 2012.

[115] S. Zippilli, G. Morigi, and A. Bachtold, "Cooling carbon nanotubes to the phononic ground state with a constant electron current," *Physical review letters*, vol. 102, no. 9, p. 096804, 2009.

APPENDICES

Appendix A

Suspended CNT Device Fabrication Processes

This appendix describes the details of the processes used in CNT device fabrication. These were all carried out in the QNFCF facilities, with the exception of the catalyst solution deposition and CVD growth. The sub-process details are given following the overall device recipes.

A.1 As-grown Suspended CNT

The devices are fabricated on a 3" Si wafer with 300 nm SiO_2 thermal oxide. The wafer is undoped Si with resistivity $\rho > 5000$ Ω/cm, and $\langle 100 \rangle$ orientation.

1. Clean wafer as required by wafer condition

2. Deposit 10 nm tungsten and 20 nm platinum using AJA sputter deposition
3. Source/Drain definition:
   (a) Photolithography using Man-1410 recipe and Source-Drain Pattern (Mask #1)
   (b) Ion mill using the AJA ATC ion mill under manual control and 400 V, 190 mA ion source operation. Total exposed etch time of 75 s, operated at 4% duty cycle
   (c) SiO_2 etching using Oxford III-V etcher. Use OPT-SiO2 for 39s to etch $\sim$ 240 nm
   (d) 10 minute, 200 W descum in YES CV200-RF plasma asher
   (e) Liftoff in PG remover
4. Gate bond pads
   (a) Photolithography using PMGI-S1805 Bilayer recipe and Gate Pad Pattern (Mask #3)
   (b) Deposit 10nm Ti, followed by 30nm Pt, using the IntlVac e-Beam evaporation system
   (c) Liftoff in PG remover
5. Cleave wafer into smaller sections for further processing
6. Fine gate deposition
   (a) Electron beam lithography using PMMA 950 A4 recipe, 100 $\mu C/cm^2$ does at 10 kV exposure
   (b) Deposit 10nm Ti, followed by 30nm Pt, using the IntlVac e-Beam evaporation system
   (c) Liftoff in PG remover
7. CNT Catalyst Deposition:
   (a) Photolithography using PMGI-S1805 bilayer recipe and CNT Mask #4 (Islands)
   (b) 6 minutes of 50W descum in YES-CV200RFS PR Stripper
   (c) Spin coat catalyst solution (see appendix B) using the following spin settings:
      i. 7s wait after drop casting
      ii. 500 RPM for 15s
      iii. 2000 RPM for 40s

iv. 0 RPM

(d) Bake sample at 100 °C for 5 minutes.

(e) Liftoff in PG remover. Use 30s PG remover soak, followed by separate 15 minute PG remove soak to minimize catalyst re-adhesion.

(f) 6 minutes of 50W descum in YES-CV200RFS PR Stripper, to remove any final resist residues.

8. CVD growth of CNTs

A.2 Stamped CNT - Device Wafer

These samples were fabricated on 4" undoped Si wafers with 300 nm SiO_2 dry thermal oxide. This version of the fabrication uses full wafer processing until final chips are separated for CNT transfer, and all photolithography.

1. Clean wafer as required by wafer condition
2. Gate definition:
   (a) Photolithography using single layer S1805 recipe and fine gate pattern on Heidelberg MLA150 maskless aligner. Nominal exposure of 80 μmJ/cm^2 may require fine adjustment depending on resist source condition and environment.
   (b) Deposit 60 nm nickel using the IntlVac e-Beam evaporation system
   (c) Liftoff in PG remover
3. Source-drain definition:
   (a) Photolithography using PMGI-S1805 Bilayer recipe and source-drain pattern in Heidelberg MLA150. Due to the beyond specification alignment required, patterns are optically inspected after development, and full lithography process is repeated until sufficient alignment is achieve.
   (b) Deposit 40 nm Ti, followed by 360 nm Au, using the IntlVac e-Beam evaporation system
   (c) Liftoff in PG remover
4. Dice wafer into individual 1 cm by 1 cm chips for CNT transfer

A.3 Stamped CNT - Quartz Wafer

These chips start from 4" z-cut quartz wafers. All processing is done on full wafer until dicing for catalyst deposition and CNT growth

1. Clean wafer as required
2. Etch mask definition:
   (a) Photolithography using PMGI-S1805 Bilayer recipe and Heidelberg MLA150 maskless aligner with "etch mask" pattern
   (b) Deposit 200 nm aluminum using IntlVac e-Beam evaporation system
   (c) Liftoff in PG remover
3. Etch $\sim 1.4\,\mu$m using Oxford III-V etcher, recipe OPT-SiO2 for 400 s
4. Alignment pattern definition:
   (a) Photolithography using PMGI-S1805 Bilayer recipe and Heidelberg MLA150 maskless aligner with "alignment marker" pattern
   (b) Deposit 10 nm Ti and 30 nm PT using IntlVac e-Beam evaporation system
   (c) Liftoff in PG remover
5. Remove aluminum etch mask in a 10 minute soak in MF-319, followed by DI water rinse
6. Spin PMMA 950 A6 onto wafer to act as mechanical mask for catalyst. Spin recipe:
   (a) 500 RPM at 500 RPM/s ramp for 10s
   (b) 4000 RPM at 2000 RPM/s ramp for 60s
   (c) 0 RPM at 500 RPM/s ramp for 0s
   (d) Bake wafer at 180 °C for 15 minutes
7. Dice wafer into 1.4 cm by 1.4 cm pieces
8. Partially etch PMMA using 50 W O_2 plasma ash in the YES asher for 6 minutes, nominally exposing pillar tops while retaining PMMA cover on etched regions.
9. Spin coat catalyst solution (see appendix B) using the following spin settings:

(a) 30s wait after drop casting

(b) 500 RPM for 5s

(c) 2000 RPM for 30s

(d) 0 RPM

10. Bake sample at 100 °C for 3 minutes.

11. Liftoff in PG remover. Use 30s PG remover soak, followed by separate 15 minute PG remove soak to minimize catalyst re-adhesion.

12. 6 minutes of 50W descum in YES-CV200RFS PR Stripper, to remove any final resist residues.

13. CVD growth of CNTs at 950 °C

A.4 Man-1410 Negative Photolithography Recipe

The basic recipe for the Man-1410 photolithography is:

1. Clean sample as required

2. Spin Man-1410 S1811 photoresist onto the sample, , with the following spin settings

   (a) 500 RPM at 100 RPM/s ramp for 5s

   (b) 3000 RPM at 500 RPM/s ramp for 60s

   (c) 0 RPM at 500 RPM/s ramp for 0s

3. Bake sample at 120 °C for 90s

4. Expose sample using MA6 Mask Aligner and desired photomask. The nominal exposure time is 35.0s.

5. Develop sample for 60s in Ma-D 533 developer, followed by 60s DI water to stop development. Rinse in DI water and blow dry with N_2.

A.5 S1811 Image Reversal Photolithography Recipe

The basic recipe for the image-reverse S1811 photolithography is:

1. Clean sample as required
2. Spin Shipley S1811 photoresist onto the sample, using the same spinning recipe as the PMGI layer in A.6
3. Bake sample at 120 °C for 90s
4. Expose sample using MA6 Mask Aligner, with a nominal exposure time of 4.0s. Fine adjustments to exposure based on current condition of resist/lamp/environment are needed to achieve $\sim 1\,\mu$m resolution.
5. 45 minute image reversal exposure using HMDS oven
6. 12.0 s flood exposure using MA6 mask aligner
7. Develop in MF-319 developer for 60 s, followed by 60 s DI water to stop development. Rinse in DI water and blow dry with N_2.

The nominal resist thickness is 1 μm.

A.6 PMGI-S1805 Bilayer Photolithography Recipe

The basic recipe for our bilayer photolithography is:

1. Clean sample as required
2. Apply a hexamethyl disilazane (HMDS) coat using the YES-310-TA HMDS Oven recipe #1.
3. Spin PMGI onto sample using the Wafer spinner, with the following spin settings
   (a) 500 RPM at 100 RPM/s ramp for 5s
   (b) 5000 RPM at 500 RPM/s ramp for 60s
   (c) 0 RPM at 500 RPM/s ramp for 0s

4. Bake sample at 150 °C for 5 minutes. If slightly less undercut is desired after development, this temperature can be increased to 190 °C.

5. Spin Shipley S1805 photoresist onto the sample, using the same spinning recipe as the PMGI layer.

6. Bake sample at 120 °C for 90s

7. Expose sample using MA6 Mask Aligner and desired photomask. The nominal exposure time is 4.0s, however the best resolution exposure settings will depend on feature size, substrate, and lamp lifecycle.

8. Develop sample for 60s in MF-319 developer, followed by 60s DI water to stop development. Rinse in DI water and blow dry with N_2.

9. Clean sample with 20 second, 50W descum recipe in YES-CV200RFS PR Stripper to remove the HMDS layer in the developed regions.

A.7 PMMA 950 A4 Electron Beam Lithography Recipe

The basic recipe for single layer EBL is:

1. Clean sample as required

2. Spin PMMA 950k A4 resist onto the sample, using:

   (a) 500 RPM at 500 RPM/s ramp for 10s

   (b) 2000 RPM at 2000 RPM/s ramp for 40s

   (c) 0 RPM at 500 RPM/s ramp for 0s

3. Bake sample at 180 °C for 15 minutes.

4. Expose sample using RAITH 150TWO electron-beam direct-write lithography system. Exposure settings will depend on sample. The nominal settings used in this work are 10 kV accelerating voltage, 30 μm aperture, 100 C/μm^2 area dose.

5. Develop sample for 30s in IPA:DI (7:3), followed by 30 in DI water, then N_2 blow dry.

Appendix B

CVD Procedures

This appendix details the CNT catalyst solution preparation and CVD cleaning and conditioning protocol.

B.1 Catalyst Recipe

All CVD growths used a Fe-Co-Mo catalyst with alumina supporting beads. The preparation process for catalyst solution is:

1. In a small glass vial, combine:
   (a) 1.4 mg of Molybdenum (II) acetate dimer ($Mo_2(OCOCH_3)_4$)
   (b) 9.2 mg of Cobalt (II) acetate ($(CH_3CO_2)_2Co$)
   (c) 6.0 mg of Iron (III) acetylacetonate ($Fe(C_5H_7O_2)_3$)
   (d) 3.0 mL of IPA
2. In a separate glass vial, combine:
   (a) 15.0 mg of fumed alumina 50 nm nanopowder (Sigma-Aldrich 544833)
   (b) 3.0 mL of IPA
3. Sonicate both vials for $\sim$ 2 hour
4. Combine 2mL of each solution into a separate glass vial
5. Sonicate the combined solution for $\sim$ 2 hours

B.2 CVD Cleaning and Conditioning

Each CVD growth was preceded by a cleaning and conditioning process:

1. Open quartz tube to ambient air
2. Ramp to 850 °C (20 minutes)
3. Wait 30minutes
4. Cool to 150 °C (∼40 minutes)
5. Reseal quartz tube
6. Ramp to 850 °C under 200 sccm H_2 flow (20 minutes)
7. At 850 °C, flow 1000 sccm CH_4 and 200 sccm H_2 (30 minutes)
8. Cool to 80 °C under 200 sccm H_2 flow (∼ 40 minutes)
9. Run an empty growth using the desired growth recipe (∼2 hours)

Appendix C

1.4 K Measurement Probe

This appendix details the design of the custom probe used for some of the 1.4K measurements conducted in this thesis. The probe was designed for general transport experiments in a commercial pumped He-4 cryostat from Janis. An optical fiber input and focusing lens was also included for sample illumination from external sources (not used in this thesis).

This probe is designed to hold a sample in vacuum at the bottom of the pumped Helium space in the Janis 1.4K cryostat. Figure C.1 shows an image of the full probe. The sample chamber at the bottom of the probe is brazed to a 12 mm stainless steel tube. Along this tube are 6 aluminum baffles. The top of this stainless steel tube is welded to a KF63 flange which seals the top of the Janis helium space. Above this flange, two breakout boxes provide electrical and optical access to the sample, and a vacuum port and valve are used for vacuum pumping of the probe before cool-down.

The sample to be tested is mounted on a custom G-10 fiber glass chip carrier and wire-bonded to the top surfaces of 0.5 mm Mill-Max Manufacturing pin terminal connectors in a 16 mm circular pattern. The chip carrier is shown in figure C.2. The Mill-max pins plug into matching sockets permanently mounted in the sample probe, allowing quick sample changes.

The Mill-max sockets are directly soldered to the probe wiring. Six high frequency inputs are connected directly from the pins to room temperature connectors at the top of the probe via semi-rigid coaxial cable (SC-119/50-SB-B from Coax Co. Ltd.). Low frequency signals pass through a low-temperature filter PCB near the sample, and then are run through constantan ribbon cable to room temperature connectors in the breakout boxes. All lines pass through a custom vacuum feed-through at the room temperature end of the probe. At the breakout box, the DC wiring is connectorized by a 24-pin Fischer

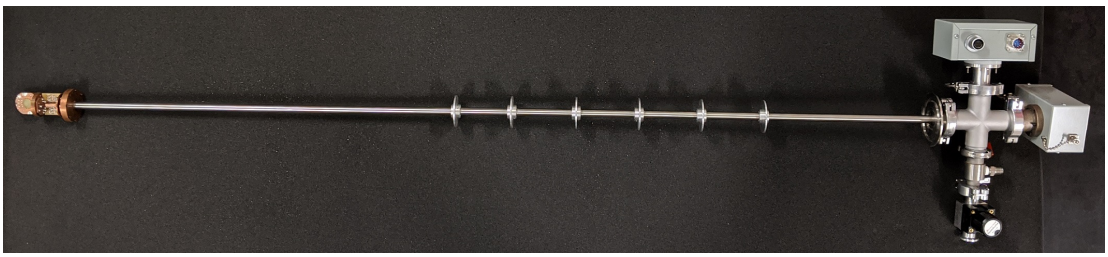

Figure C.1: The 1.4 K measurement probe. The sample is mounted in the assembly at the bottom (left of this photo), and then sealed using a copper can assembly. Wires run from the sample end, through the inner space of the stainless steel tube, and out through vacuum feed-throughs to the breakout boxes at the top (right side of photo).

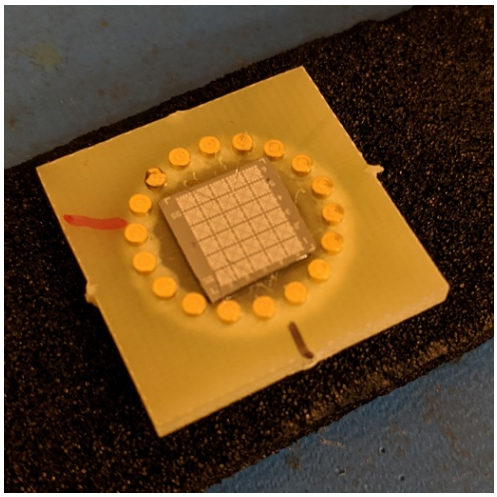

Figure C.2: The chip carrier used with the 1.4 K measurement probe. The sample is varnished onto the supporting G10 material as shown, then bonding pads on the sample are connected to the surrounding pin by wire bonding. The pins protrude through the back face of the chip carrier to interface with a matching pattern of sockets in the measurement probe.

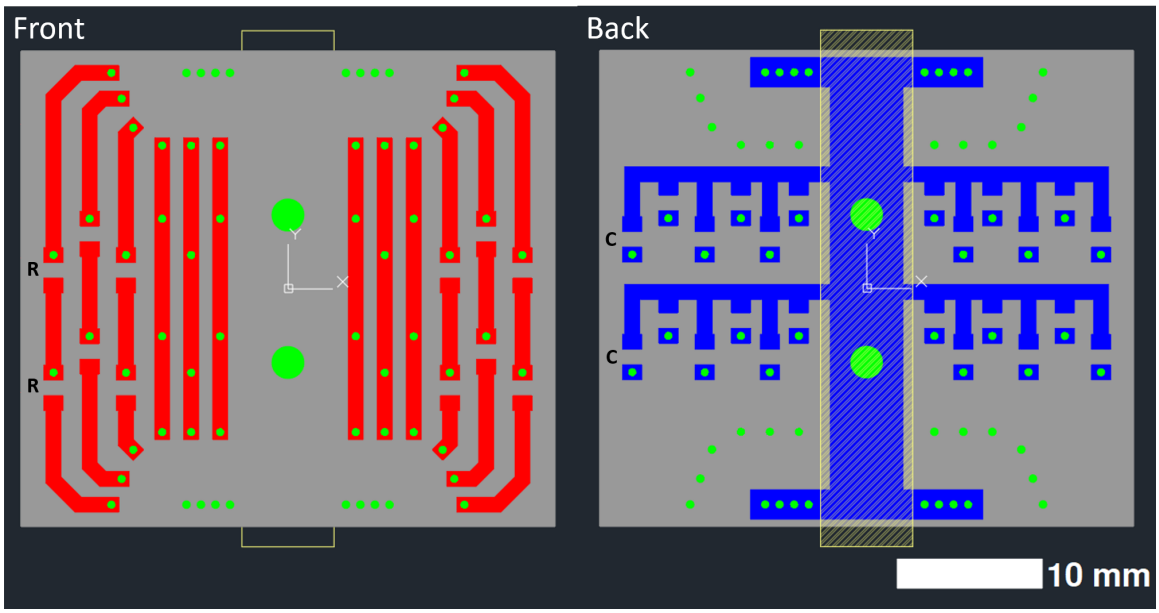

Figure C.3: Design of the PCB for low temperature filtering in the 1.4 K probe. The left panel shows the front face , and the right panel shows a mirror of the rear face. Each of the 6 outer traces include 2-pole RC filters, with the placement of R and C labeled on the left-most trace. The inner paths do not include filtering, for higher bandwidth connections.

connector (DBEE 105 A093-80) with a matching connector leading to a separate BNC connectorized breakout box. High frequency lines are terminated at the breakout box by panel mount SMA connectors.

Low temperature filtering on 6 of the 12 DC connections is performed by 2-pole RC filters . Figure C.3 shows the PCB of the low-temperature filter. The values for the R(C) components are 26 kΩ (10 nF), providing ≈ 4 kHz low pass filtering.

Finally, the optical access to the sample is done using a custom 3-fiber assembly and focusing lens adjacent to the sample. The fiber assembly is comprised of three single mode fiber optics ending in a custom ceramic ferrule. The fibers are specified for wavelength ranges: 400-680 nm, 780-970 nm, 980-1550 nm. The ceramic ferrule is locked into a custom alignment assembly which also includes an adjustable focusing lens. At the room temperature side of the probe, the fibers pass through a vacuum feedthrough and are terminated at the breakout boxes with standard panel mount FC connectors.

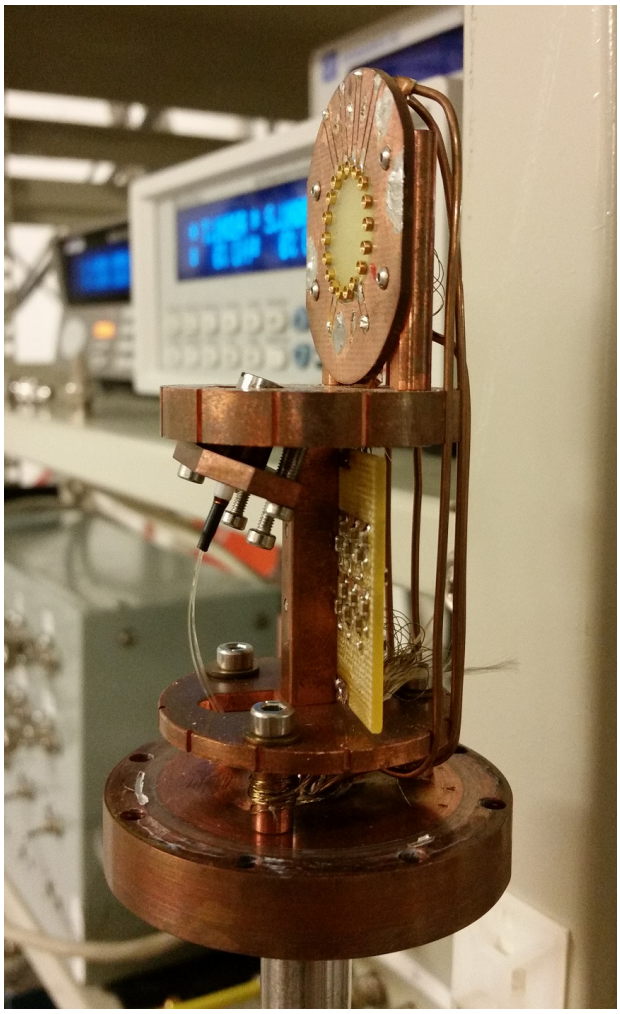

Figure C.4: Photograph of the low-temperature/sample end of the 1.4 K measurement probe. All wiring is input through a hole at the bottom of the photo, and routed to the sample mounting board (HF) or filter board (DC). The filter board and optical assembly are shown in the middle of photo, and the PCB and sockets for sample chip carrier mounting are in the top of the photo.

Appendix D

Methods for transient response measurement

This appendix describes the envelope calculation and fitting procedures referenced in chapter 4.

D.1 Calculating current envelope

The time-domain measurements reported in figure **4.4**c,d and figure **4.5**b were measured with an oscilloscope after amplification of I_{out}. The current recorded at the oscilloscope is a product of the conductance of the CNT and the 100 kHz bias voltage. To extract the conductance of the CNT, we apply a MATLAB RMS envelope extraction function with 10μs window, analogous to the output signal of a lock-in amplifier with similar time constant.

An example of the oscilloscope signal is shown in figure D.1(a). In addition to the 100 kHz bias frequency, there is a 16 kHz oscillation in the average current that was observed in all measurements and is likely an artifact of the voltage source used for $V_{g,dc}$. This noise is removed during post-processing by applying a narrow band-stop filter at 16 kHz. Figure D.1b shows the data from (a) after this filtering. Finally, the RMS envelope is extracted from the filtered data. Figure D.1c shows the envelope extracted from (b).

D.2 Fitting time-domain data

To model the time-domain current measurements presented in figures 4.4 and 4.5 of the chapter 4, we use equation 4.2 to determine the oscillator motion as a function of time, then calculate current using equation 4.1. The parameters used in these equations are determined as follows:

- C_g, $\partial C_g/\partial x$, and m are estimated from the device geometry. Based on Raman spectroscopy of similar CNT samples, a CNT diameter of 1.5 nm is assumed.
- From off-resonant current data, e.g. at $f = 87$ MHz in figure 2a of main text, $\partial^2 I'/\partial V_g^2$ is calculated.
- The resonant frequency, ω_0, is determined using low drive power and is used to calculate k.
- Values for α, γ, and η are estimated from similar devices in literature, then fine tuned to fit the time domain data in the following sequence:
    1. The transient decay time when F_{drive} is turned off is fit by adjusting damping parameters γ and η.
    2. The fit to turn on behaviour is improved by adjusting α.
    3. γ and η are adjusted to fit the steady state amplitude while maintaining a good match to the turn-off decay.

Figure D.2 shows the fitting steps for the data from main text figure **4.4**d.

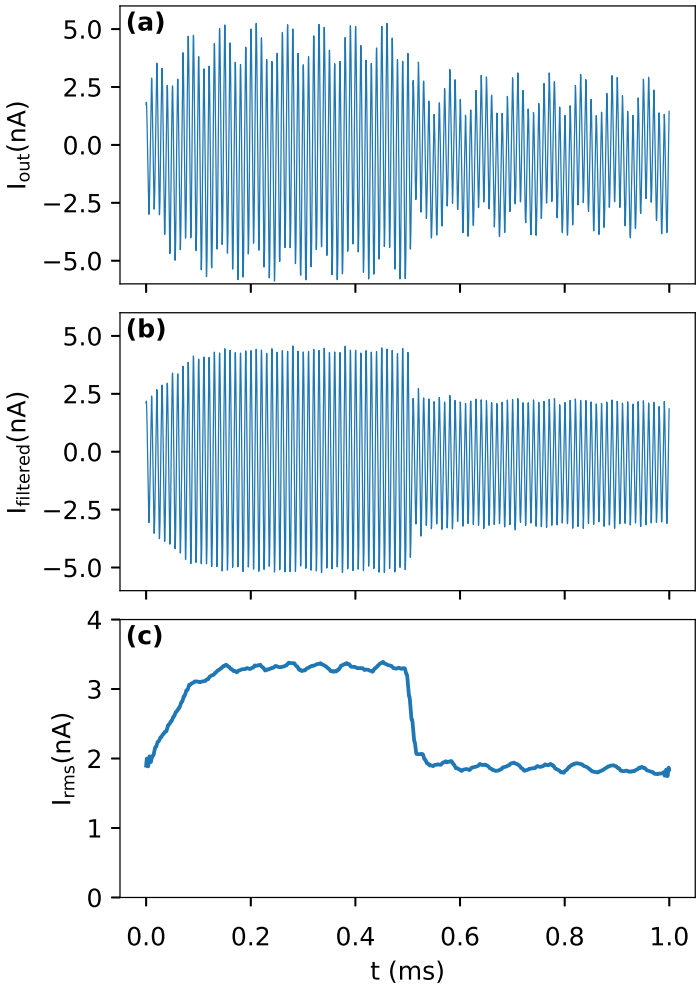

Figure D.1: **a** I_{out} as recorded on an oscilloscope and averaged over 2048 shots. **b** The same data as (a) after applying a band-stop filter at 16 kHz. **c** The RMS envelope of (b) calculated using MATLAB RMS envelope function with 10μs sliding window.

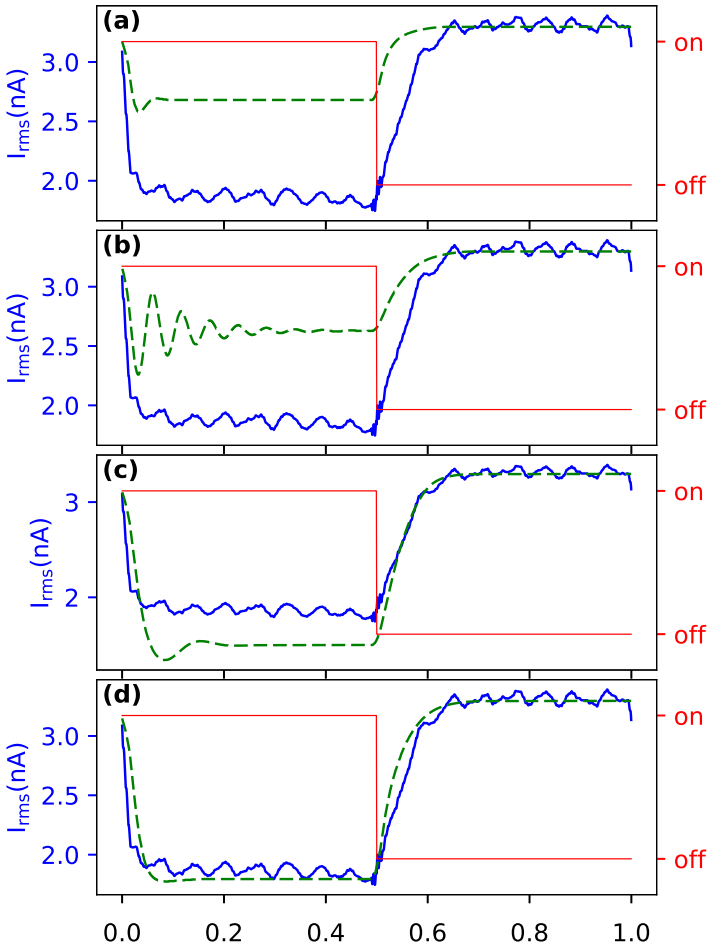

Figure D.2: Fitting of time-domain current signals. **a** Using rough initial estimates of $\alpha = 5\times10^{10}, \gamma = 1\times10^{-16}, \eta = 100$. **b** After fitting the turn-off decay time, $\gamma = 1\times10^{-16}, \eta = 4$. **c** After fitting the turn-on transient shape, $\alpha = 5\times10^{9}$. **d** Finally, adjusting how damping terms affects steady state, while maintaining the turn-off decay fit, $\gamma = 1\times10^{-17}, \eta = 22$

Appendix E

Dilution Refrigerator Electronics

This appendix details the wiring that was installed into an Oxford Instruments DR200 dilution refrigerator, which was used for measurements in chapter 5. This wiring was designed for general transport experiments, with a specific target of operation of several gate-defined 2DEG quantum dots. The current configuration provides 19 filtered low frequency and 4 high frequency lines to a device region, including 1 line designed for 40 GHz signals. Each high frequency line is connected through a custom low temperature bias tee to additional filtered DC inputs. The current configuration can expand up to 21 low frequency and 15 high frequency connections with updates to the bias-tee and device PCBs.

E.1 Room temperature to mixing chamber

Figure E.1 shows a schematic of the current configuration of the fridge wiring.

The low frequency lines are run in constantan twisted pair ribbon cable (Oxford Instruments A8-312), with each pair carrying one signal wire and one grounded wire. At each thermal stage in the fridge, the wires pass between gold plated oxygen-free copper clamps to thermally anchor the lines. At the 100 mK plate, the lines pass into a 3-pole RC filter. For low frequency connections which will lead to the low temperature bias tees, the RC filter has a design cutoff frequency of 24 Hz, and include a series resistance of 4 MΩ. For low frequency connections to the device board, the RC filter has a designed cutoff of 30 kHz, and a series resistance of 2 kΩ. The schematics of the RC filters are shown in figure E.2.

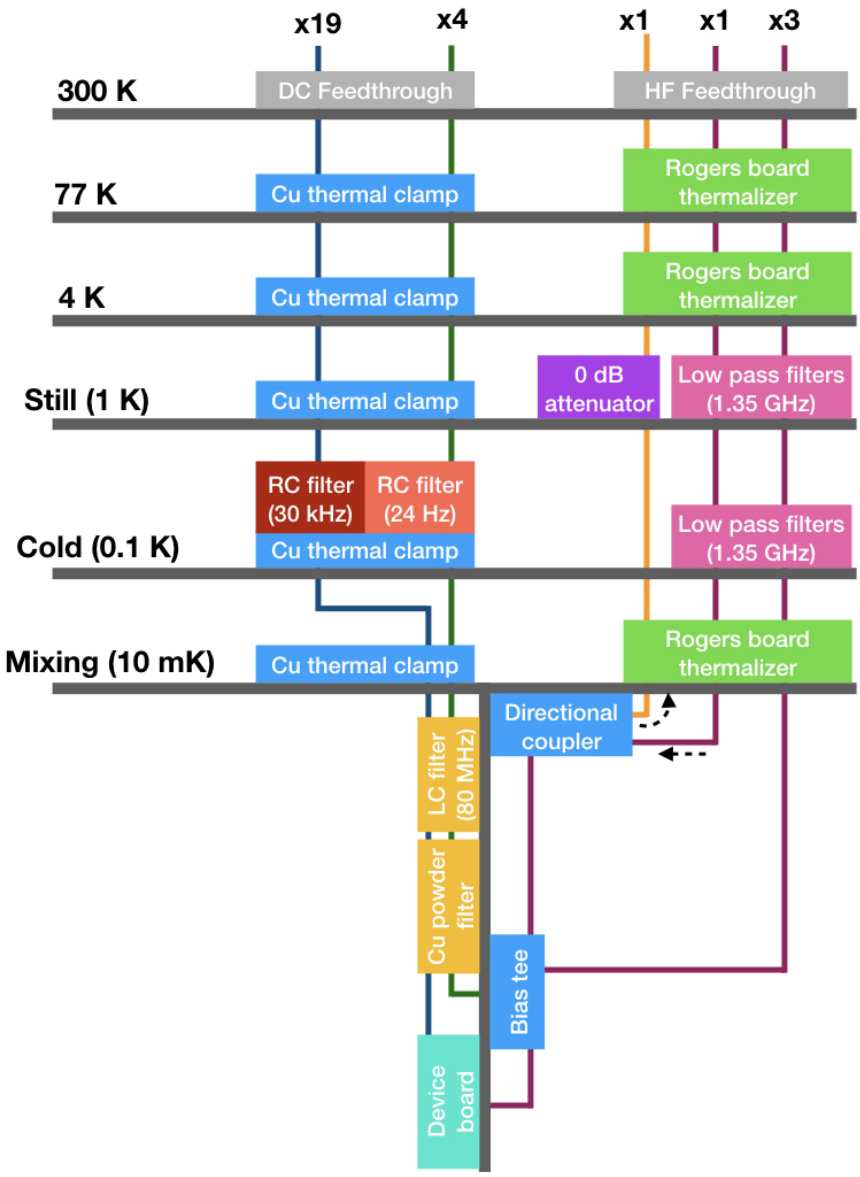

Figure E.1: Schematic of electronics filtering and thermalization for DR200 dilution refrigerator wiring. The blue line indicates low frequency connections to the device, the green lines are the low frequency components to the bias tee, the orange line is the 40 GHz high frequency line, and the purple lines are the other high frequency lines.

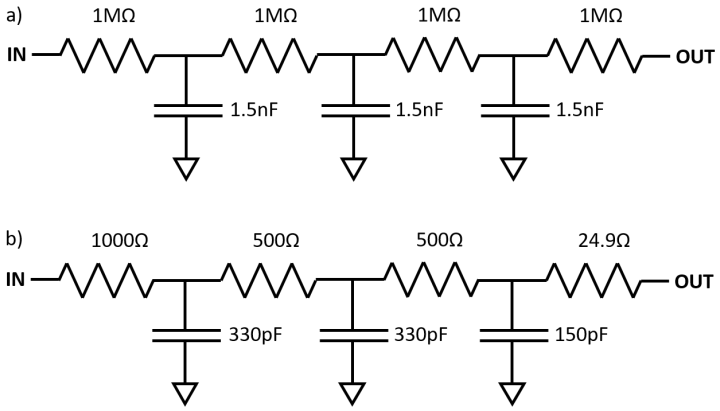

Figure E.2: The 3-pole RC filters for low-frequency signals. These filters are mounted to the 100 mK stage of the dilution refrigerator. **a** This high-impedance, 24 Hz low pass filter is used for DC inputs to the low temperature bias tees. **b**. This 30 kHz low pass filter is used for low frequency signals to the device board.

The main high frequency lines are designed to carry 1 MHz − 1.35 GHz signals to the sample. Between thermal stages of the fridge, the signals are carried by 0.047" inner diameter semi-rigid coaxial cables. All cables have a stainless steel outer shield to reduce thermal load on lower temperature stages. Above the still plate, the inner conductor is also stainless steel to reduce thermal load, at the cost of greater losses in HF signal. Below the still plate the inner core is beryllium copper. As the inner conductor of the cables is thermally isolated from the shield by a PTFE dielectric layer, thermal anchoring/cooling of the HF lines is done by custom microstrip anchoring boards. The microstrip boards are comprised of gold plated copper traces on 0.02" thick Rogers 4350B board, a high thermal conductivity PCB material. The PCBs are thermally connected to the fridge stages by Pb/Sn solder to gold-plated oxygen-free casings, which are bolted to the thermal stages. Figure E.3 shows an example one such copper box, which includes three microstrip boards and the coplanar waveguide board used for the 40 Ghz connection. At the 1 K and 100 mK stages, the high frequency lines pass through commercial low-pass pi filters (VLFX-1350 from mini-circuits) with cutoff frequency of 1.35 GHz.

The high frequency line designed for 40 GHz operation is connected through beryllium copper inner-outer semi-rigid coaxial cables to reduce losses at high frequencies that would be created by stainless steel components. At the 77 K, 4 K, and mixing chamber stages, this cable is thermalized in a similar manner to the other high frequency signals, except with a grounded coplanar waveguide fabricated on 0.008" thick R4003C Rogers board in

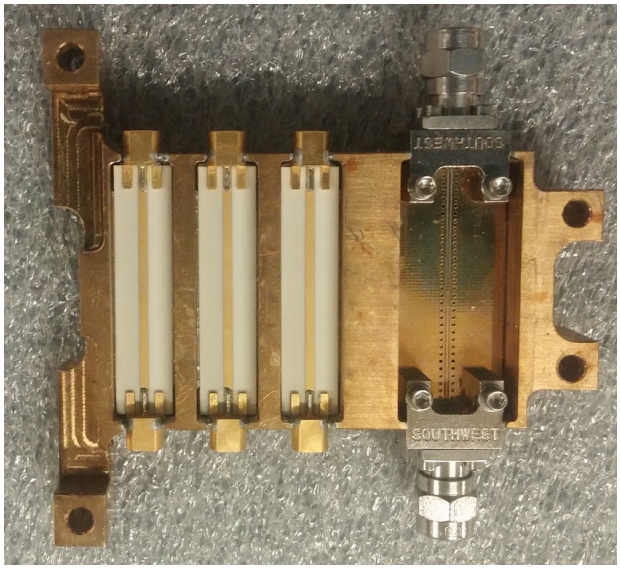

Figure E.3: A gold-plated copper box assembly including three microstrip thermalizers for high frequency signals, and the waveguide thermalizer (right side) for the 40 GHz line.

place of the microstrip. This waveguide can be seen on the right side of the box shown in figure E.3. The 40 GHz line is further anchored at the 1 K plate using a commercial 0 dB cryoattenuator (Bluefors part #: TA-4882-5008-00U-CRYO). In the current configuration this line is connected to the output of a directional coupler, however it can bypass this and connect directly to the device PCB using a 2.4 mm connector.

E.2 Copper powder PCB filter

At the mixing chamber, all low-frequency signals pass through a combined LC and copper powder filter PCB.

Figure E.4a shows a circuit description of a single line through the filter board. An overall R-C filter and three stage L-C filter (using off the shelf LFCN components from Mini-circuits) is used to reduce high frequency noise. After the LC output, the lines form a meandering 30 cm trace which is coated in copper powder infused epoxy that acts as a lossy dielectric to further thermalize the signals. Figure E.4b shows a render of one side of the filter board PCB without components or copper powder shown.

The copper-powder epoxy is a combination of non-conducting epoxy (MG chemicals

832C translucent 2-part epoxy) and copper powder (Alfa Aesar part #: 13990). The copper powder:epoxy is blended 1:3 by weight. After mixing the epoxy is left to rest for 30 minutes to reduce air pockets in final pour. The epoxy is applied to the PCB in ~ 1 mm thick layers then left to cure. Three total layers were applied to each side of the PCB. Figure E.4c shows a photograph of the finished PCB with copper powder epoxy.

E.3 Bias-tee PCB

The high frequency inputs to the device board are combined with a DC input using a custom bias tee PCB mounted to the mixing chamber of the dilution refrigerator. The high frequency signals are input through mini-SMP connectors (Pasternack PE44489) on the front face of the PCB, combined with the DC voltages, then output through identical mini-SMP connectors on the back side of the PCB. The rear-side mini-SMP connectors connect directly to the device board. The DC voltages are input through a nano-D connector (GlenAir 890-012).

The HF and DC signals are combined using a standard inductor-capacitor bias tee design, with an additional capacitance on the DC input to reduce HF feedback onto the upstream DC components. The circuit is shown in figure E.5a. Figure E.5b and c show renders of the PCB design.

E.4 Device PCB

The device under test is attached to a custom PCB with pads for wire bonding between the PCB and the device chip. The DC inputs are provided by a 21-pin nano-D connector and the HF signals pass through mini-SMP connectors which mate with the corresponding connectors on the bias tee PCB. The DC signal paths include an additional LC filter (LFCN-80+) adjacent to each bond pad to reduce any high frequency pick-ups that may occur between the copper powder filter and the device board. Figure E.6 shows an image of the device PCB. All DC and HF lines are connected to a grounding PCB during wire-bonding, transport, and initial connection to reduce the risk of electrostatic discharge damaging the device.

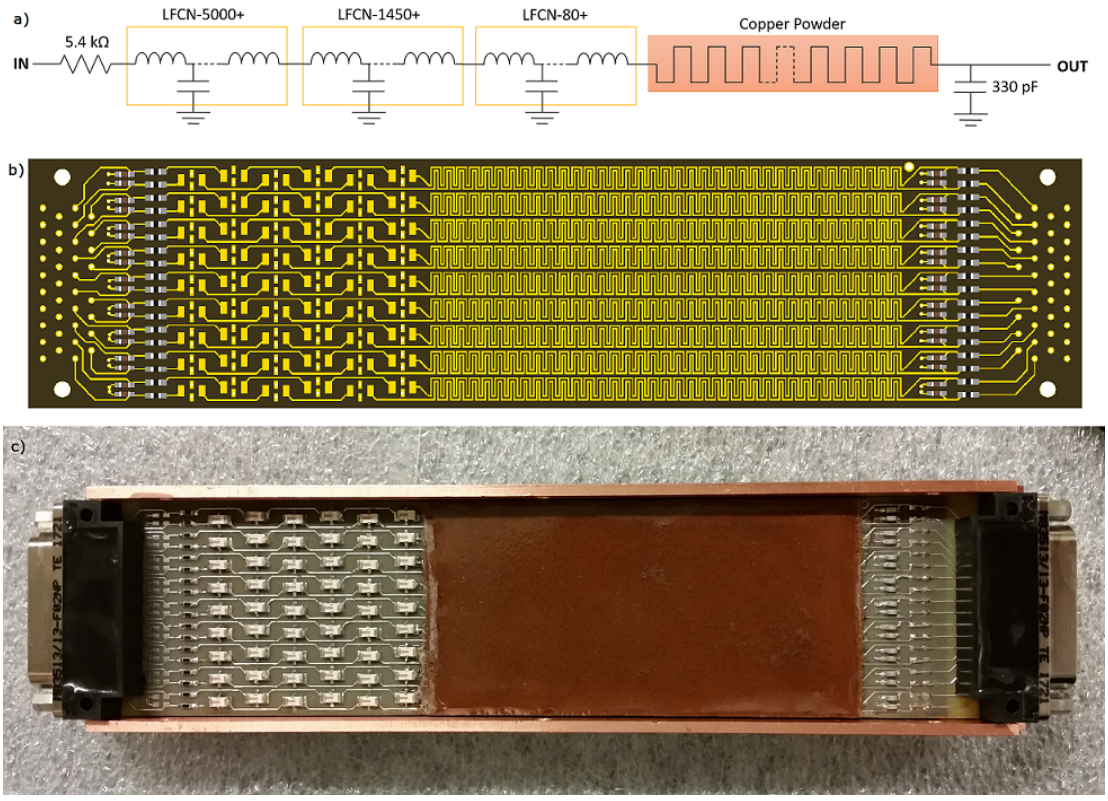

Figure E.4: **a**. The circuit of the copper powder filter board. The circuit includes an overall RC filter, 3 commercial LC filter components, and a 30 cm meandering line under a custom copper powder epoxy. **b**. One side of the PCB design of the copper powder filter board. The reverse side has an equivalent circuit, but connected to the outer pins of the end launch connectors. **c**. A photograph of the completed copper powder filter, including the cured copper powder epoxy over the meandering traces.

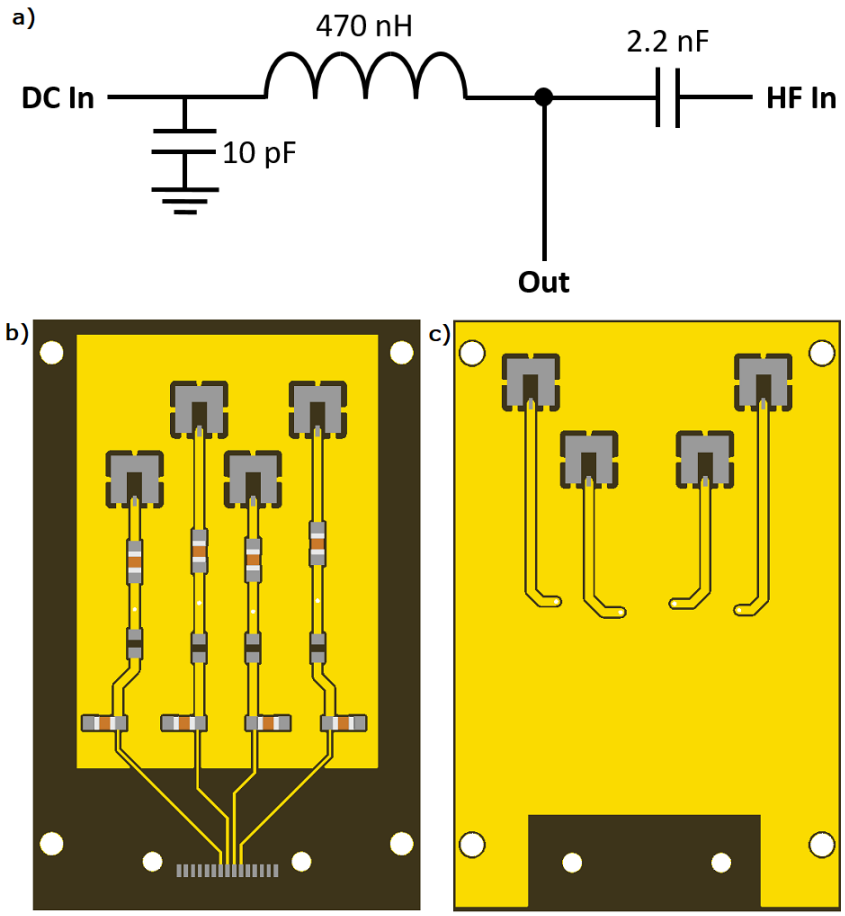

Figure E.5: **a**. The L-C circuit used as a bias tee to combined DC and HF inputs to a single output line. **b** The front face of the bias tee PCB, including the HF inputs at the top and DC inputs at the bottom. The combined signals are passed through vias to the reverse side (**c**).

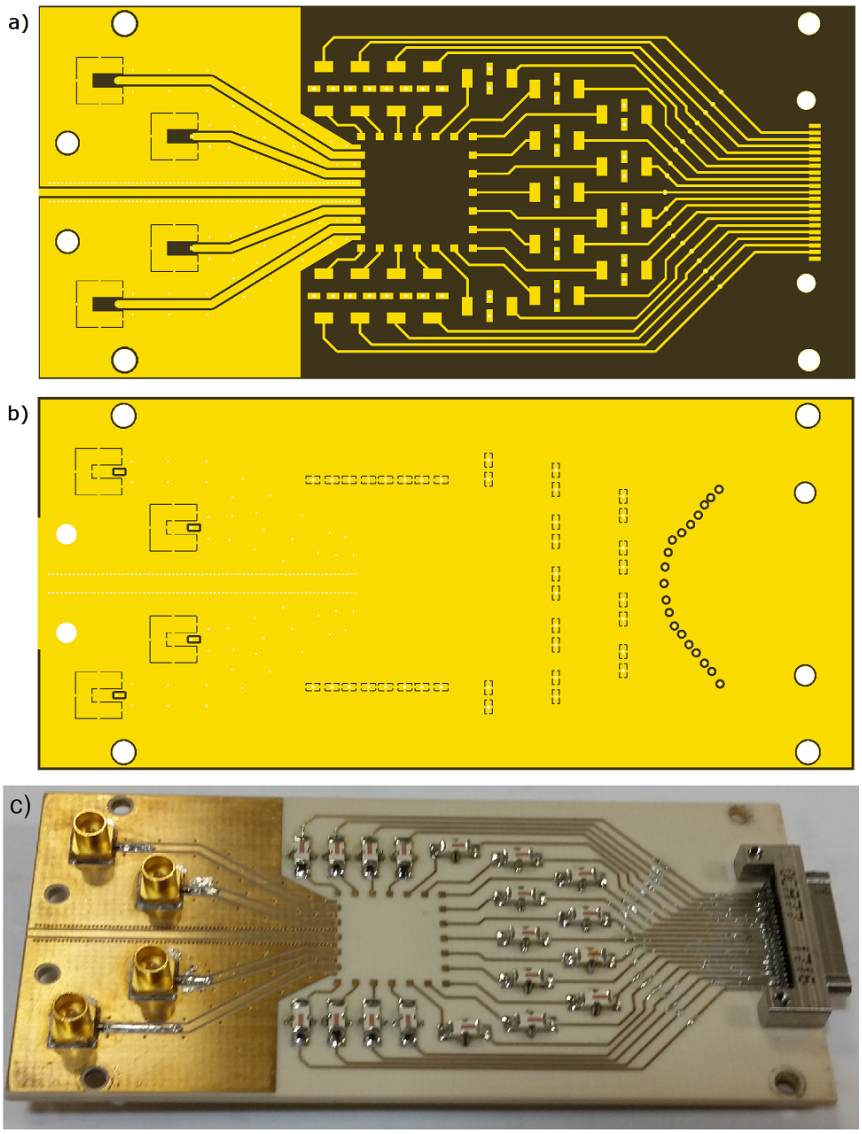

Figure E.6: The front (**a**) and reverse (**b**) side of the PCB designed for sample mounting for the dilution refrigerator electronics. The DC signals are input by a nano-D connector on the right side, and pass through LFCN-80+ filters before terminating at wirebond pads adjacent to the sample area. High-frequency signals are input on the left side and carried by coplanar waveguides to similar wirebond pads. **c** A photograph of a populated device PCB.

E.5 Electron thermometry experiment

To test the efficacy of the filtering components, a GaAs quantum dot was measured in the dilution refrigerator using the DC signal lines. The dot was formed in an $Al_{0.33}Ga_{(0.67)}As/GaAs$ heterostructure, with the 2-dimensional electron gas (2DEG) located 110 nm below the surface. The heterostructure has a 10 nm silicon cap and a δ-doping layer 70 nm under the surface (n-type doping with $\rho = 5 \cdot 10^{11} cm^{-2}$). The quantum dot is realized by applying negative gate voltages on a set of Ti/Au (20/20nm) metals gates which deplete the 2DEG to form a ~ 100 nm dot region.

The conduction through the quantum dot at low temperatures is given by the equation

$$G(\mu, T) \approx \frac{e^2}{h} \frac{A}{k_B T} \text{sech}^2 \left[\frac{\alpha(V_g - V_o)}{2k_B T} \right] \tag{E.1}$$

where G is the conductance of the dot, A is an amplitude fitting parameter, T_e is the electron temperature, α is the gate lever arm (determined from Coulomb diamond measurements), V_g is the plunger gate voltage, and V_o is the applied gate voltage at which the peak is maximum. In fitting experimental conduction peaks, V_o and A depend only on the peak height and position. The electron temperature, T_e, is determined by fitting to the conduction peak shape.

Figure E.7a shows a conductance peak measured in the GaAs quantum dot in the dilution refrigerator when operating at base temperature ($T_{mc} \approx 30$ mK). In fitting equation E.1 to the data, we find an estimated electron temperature of $T_e = 35.5$ mK. Using the mixing chamber plate resistive heater, the stage was heated to four additional temperatures, and the conductance peak measurement and fitting was repeated. Figure E.7b shows the extracted T_e as a function of the mixing chamber temperature T_{mc}. The electron temperature shows near perfect matching of the mixing chamber down to base temperature.

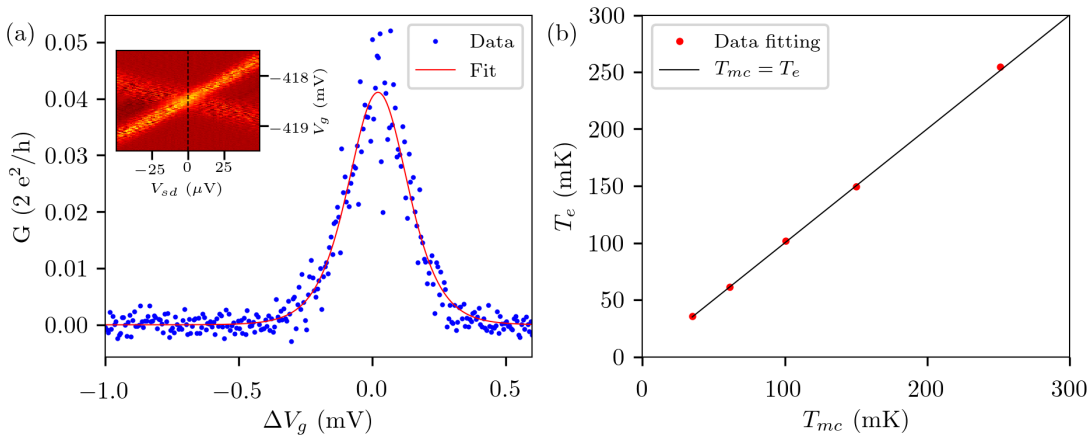

Figure E.7: **a**. Conductance peak of the gate-defined GaAs quantum dot measured at the base temperature in the dilution refrigerator. The red line shows a fit to the data using equation E.1 and $T_e = 35.5\,\text{mK}$. The inset shows the Coulomb diamond vertex at which the conductance was measured. **b**. The electron temperature (T_e) determined from conductance peak fitting, as a function of the mixing chamber temperature (T_{mc}).

Appendix F

In-situ sublimation for molecular nanomagnet deposition

This appendix describes a process for in-situ sublimation in the 1.4K Janis probe, intended for the deposition of molecular nanomagnets onto suspended carbon nanotube devices. The procedure was tested with $Dy(hfac)_3(bipy)$ and $Tb(hfac)_3(4\text{-benzylpyridine})_2$ nanomagnets. While no magnetic signatures were seen from these experiments, the sublimation process was able to deposit material onto the CNTs.

The in-situ sublimation is realized using a low-thermal mass resistive heating element to rapidly raise the temperature of small quantities of the molecules of interest. A platinum resistance temperature detector (RTD) was used as the resistive heater, which allowed for real-time temperature readout while driving current to heat the RTD. Specifically, the TE Connectivity PTFC102BC1G0 was selected. This has a 0°C resistance of 1 kΩ, and is calibrated down to 77 K, where $R = 200\,\Omega$. The resistance measured at 1.4 K was approximately 10 Ω.

The platinum RTD leads are connected to the cryostat probe via stainless steel wires to reduce thermal load on the probe/sample during heating of the RTD. The stainless steel wires are soldered directly to low resistance lines of the cryostat probe, in this case using the coaxial high frequency lines. Aluminum film is used to create a small pocket around the RTD that holds the molecule to sublimate. Figure F.1a shows a photo of the RTD assembly connected into a cryostat probe.

The sublimation heating process is powered using a Keithley Sourcemeter 2401. The sourcemeter is configured to measure resistance while applying fixed current driving. During initial heating an 8 mA current is applied through the RTD. Upon reaching the target

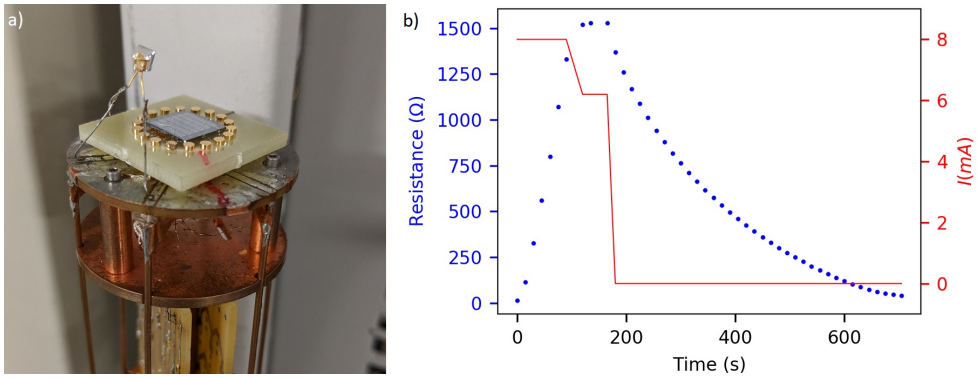

Figure F.1: **a** Photo of platinum RTD assembly soldered into 1.4 K cryostat probe. The RTD is connected through stainless steel wires to low resistance cryostat lines. An aluminum film pocket attached to the RTD head holds the material for sublimation. **b** Applied driving current and measured RTD resistance when warming from 1.4 K to 135°C, holding for 30 s, then cooling.

resistance (temperature), the driving current is reduced to stabilize the temperature for the desired sublimation time. Then the driving current is switched off. Temperature measurement can continue using 10 μA current. Figure F.1b shows the applied current and measured resistance for an example sublimation run. The target resistance of 1520 Ω corresponds to a temperature of 135°C.

The sublimation process was tested with two varieties of molecular nanomagnet that had demonstrated sublimation near $80 - 100$°C in ex-situ testing, $Dy(hfac)_3(bipy)$ and $Tb(hfac)_3(4\text{-benzylpyridine})_2$. In all tests, approximately 1 mg of nanomagnet material was placed into the aluminum pocket. After inserting the material, the cryostat probe was quickly sealed and pumped to pressures below $5 \cdot 10^{-6}$ torr, then inserted into cryostat. A test run in which the RTD was only heated to 0°C while in cryostat verified that the molecular material remained in place through this loading and preheating process. Upon heating the RTD above 80°C, both of the tested molecule types sublimated out of the pocket.

Figure F.2 shows an overlay of the mechanical resonance frequency measurement of a suspended carbon nanotube test device before and after sublimating using the RTD heater. This test used the $Tb(hfac)_3(4\text{-benzylpyridine})_2$ molecule, and heating up to 70°C for 30 seconds. After sublimation, the resonance frequency decreases by approximately 5 MHz in the range shown. Using a simple harmonic oscillator approximation, the change in mass

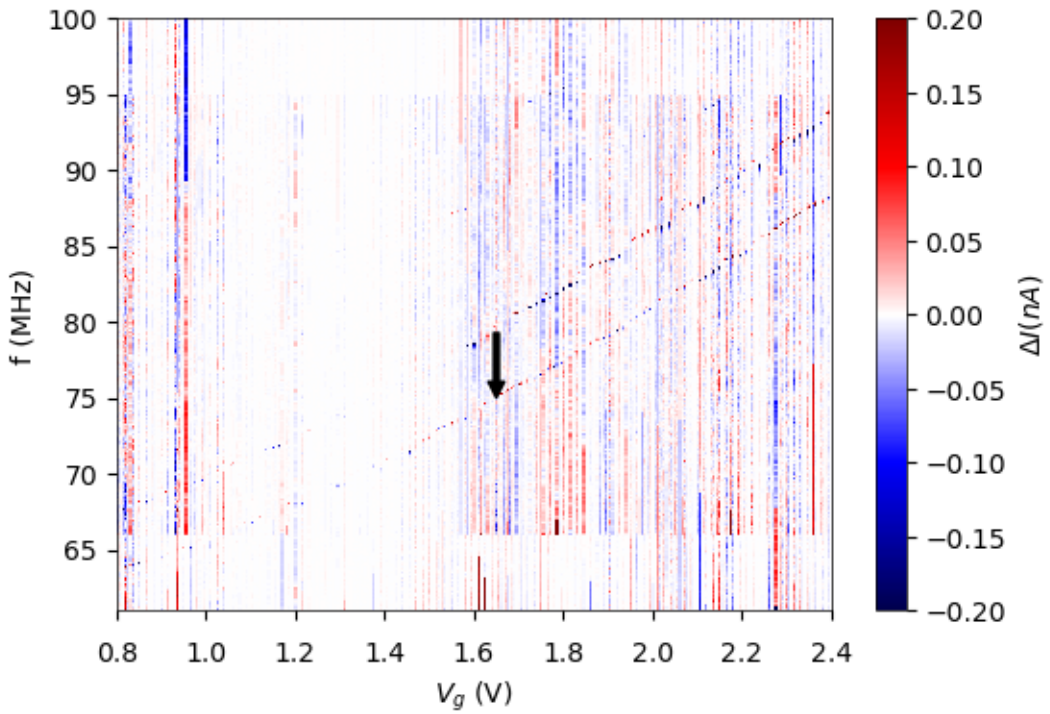

Figure F.2: Frequency-modulation readout of mechanical resonance, before and after in-situ sublimation. Colorscale shows difference from average current at each gate voltage as a function of drive frequency, overlaying data before and after the sublimation. The higher frequency mode was measured before sublimation. After sublimation the mechanical resonance frequency is decreased by approximately 5 MHz

can be estimated

$$\frac{m_2 - m_1}{m_1} = \frac{f_1^2}{f_2^2} - 1 \tag{F.1}$$

where $m_1(m_2)$ and $f_1(f_2)$ are the mass and resonance frequency before (after) deposition. The initial mass, m_1, can be estimated from average CNT parameters measured with devices similar to the one used in this test, $d \approx 2\text{nm}$ and $L \approx 2\mu\text{m}$, giving $m_1 \approx 5 \cdot 10^{-21}\,\text{kg}$. Then, the change in effective mass for this deposition is $\Delta m = m_2 - m_1 \approx 7 \cdot 10^{-22}$ kg, corresponding to approximately 300 intact $\text{Tb(hfac)}_3\text{(4-benzylpyridine)}_2$ molecules.